Development and Validation of a Numerical Model for an Inflatable Paper Dunnage Bag Using Finite Element Methods

by

Martin Philip Venter

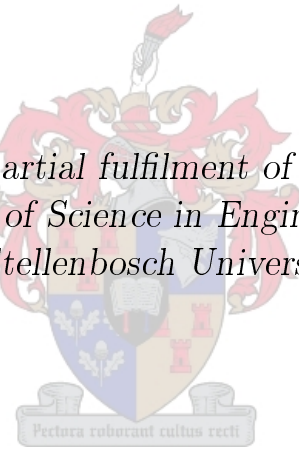

Thesis presented in partial fulfilment of the requirements for the degree of Master of Science in Engineering (Mechanical) at Stellenbosch University

Department of Mechanical & Mechatronic Engineering
University of Stellenbosch
Private Bag X1, 7602, Matieland, South Africa

Supervisor: Prof G. Venter

March 2011

Declaration

By submitting this thesis electronically, I declare that the entirety of the work contained therein is my own, original work, that I am the owner of the copyright thereof (unless to the extent explicitly otherwise stated) and that I have not previously in its entirety or in part submitted it for obtaining any qualification.

Date: .....

Abstract

Development and Validation of a Numerical Model for an Inflatable Paper Dunnage Bag Using Finite Element Methods

M.P. Venter

Department of Mechanical & Mechatronic Engineering
University of Stellenbosch
Private Bag X1, 7602, Matieland, South Africa

Thesis: MSc.Eng (Mech)

March 2011

This thesis relates to the development of a numerical model for an inflatable paper dunnage bag. Dunnage bags fill the voids between cargo, thus securing the cargo in place. The numerical model is developed as a design tool for investigating the trends associated with new or existing bags.

Modeling considerations are outlined with an emphasis on the material properties of paper. The effects of material, goemetry and boundary condition non-linearity are discussed.

The development of a stable generic model is described in detail. The effect of time scale factor, load application, analysis time, global damping, mesh refinement, Poisson's ratio and mass scaling are investigated. The development of a representative model follows, where the process of including the inflation valve, glued seam lines, void constraint size and material model are discussed.

Physical testing was performed, and the results were used to validate the numerical model developed. The the shape of the inflated model matched that of the physical samples, and the restraining force produced by the bag was found to be within 7% of the tested values.

Uittreksel

Ontwikkeling en Geldigheidsbepaling van ‘n Numeriese Model vir ‘n Opblaasbare Papier Stumateriaal-sak deur van Eindige Element Metodes gebruik te maak

(“Development and Validation of a Numerical Model for an Inflatable Paper Dunnage Bag Using Finite Element Methods”)

M.P. Venter

Departement Meganiese Ingenieurswese
Universiteit van Stellenbosch
Privaatsak X1, 7602, Matieland, Suid Afrika

Tesis: MSc.Ing (Meg)

Maart 2011

Hierdie tesis handel oor die ontwikkeling van ‘n numeriese model vir toepassing op papier stu sake. Hierdie sake word gebruik om spasies tussen vrag op te neem en sodoende die vrag te beskerm tydens vervoer. Die numeriese model is ontwikkel as ontwerp gereedskap om huidige en nuwe sake se gedrag te ondersoek.

Die modelerings proses word bespreek met ‘n beklemtoning van die materiaal eienskappe van papier en die effek daarvan op die model. Die invloed van geometrie, grens voorwaardes en nie lineariteite in die model word ook bespreek.

Die ontwikkeling van ‘n stabiele generiese model word ook in diepte bespreek. Die effek van tyd skaal factor, las geval, analiese durasie, stelsel demping, maas verfyning, Poissonâs verhouding en massa skalering word ondersoek. Dit het die ontwikkeling van ‘n verteenwoordigende model tot gevolg waar die proses om die inflasie klep, gegomde soom lyne, gaping grotes en materiaal model in te sluit bespreek word.

Fisiese toetse was gedoen en die toetsdata was gebruik om die numeriese model te valideer. The vorm van die model was verteenwoordigend van die werklikheid en die kragte in die sak was binne 7% van die gamete waardes.

Acknowledgments

Thanks to

Stopak for the opportunity to work on this project as well as financial backing and technical advice. Livermore Software Technology Corporation for LS-DYNA software licenses. Jennifer de Beyer for editing this thesis. My mother, father and stepfather for their support. Prof. Gerhard Venter for his experience and guidance. Niklas Kreutzman form Mondi Steti for information on kraft paper. Liesl Crous for translation of the abstract.

Contents

List of Figures

List of Tables

Chapter 1

Introduction and Project Description

1.1 Introduction to Dunnage

Dunnage is the term used to describe any material used to protect goods and their packaging. Cargo in transit might require protection from mechanical damage, contamination and moisture. This project focuses on dunnage used to protect cargo from mechanical damage, such as impact. This type of dunnage protects cargo by filling voids within a container, either securing the cargo itself or assisting in securing cargo through other means, such as strapping. Contamination by moisture and other agents is protected against by isolating goods from the environment with a covering, or lifting cargo off the floor.

Types of dunnage may include scrap packing materials, plastic films, assorted coverings, wood, rice matting, liner bags, inflatable bags and cushions. Dunnage is made from various materials including wood and organic fibers, plastic films, woven materials, laminates and paper.

Several points should be considered in dunnage selection. The cost of dunnage materials is not the only consideration when choosing a type of dunnage. Dunnage may be transported both to and from places of use. It also takes up volume and adds mass to a transported load. These considerations necessitate that the chosen dunnage should be as lightweight and low volume as possible, given the expected load conditions. Dunnage is also subject to approval by several bodies including the Association of American Railroads, the International Maritime Organization and the European Railway Regulations. The 'Rules Governing The Loading, Blocking And Bracing Of Freight In Closed Trailers And Containers For TOFC/COFC Service' [AAR (2001)], is an example of the rules governing rail transportation and 'Rules And Procedures For Testing Of New Loading And Bracing Methods Or Materials' [AAR (2007)], is an example of the rules governing the testing of bracing methods. Other legal considerations are duties to be paid on imported timber and the quarantine of some materials used for dunnage to avoid transporting pests across

borders. For details see the Agricultural Pests Act 36 of 1983 [ZAF (1983)], in conjunction with International Plant Protection Convention.

1.2 Inflatable Dunnage Bags

Inflatable dunnage bags or air cushions are an adaptive cargo securing mechanism. Dunnage bags are positioned between goods within a container and inflated to fill voids with a compressed volume of air. With these voids filled and the compressed volume securing the cargo, movement within a container is limited. Limiting the amount of relative movement between goods reduces the chance that goods impact either with each other or the walls of the container while in transit.

Dunnage bags work by filling the voids between goods with a contained air volume under low pressure. This pressure is distributed over the contact surface between the inflated dunnage bag and the goods or packaging they secure. This securing method produces a large securing force without rigid contact points that could damage the goods. Air volumes also act as springs, being free to compress more than traditional dunnage, further protecting cargo.

Dunnage bags can be used to provide both lateral securing force or fore/aft impact protection. A typical application for inflatable dunnage bags is to secure paper rolls in rail transportation. Paper printing machines are sensitive to flat spots in their feed rolls which could cause the paper strip to break and damage the machine. Dunnage bags can be inflated between paper rolls, securing them within the container and preventing the rolls from bumping into each other during activities such as shunting.

Dunnage bags are typically pillow shaped when inflated, though they are rectangular sheets when deflated and laid flat. Other shapes are also used for more specific purposes.

The two main components of a dunnage bag are the bladder and the covering. The bladder serves as an airtight inflatable bag, and is fitted with a non-return valve for inflation. Alone, the bladder is not suitable for securing cargo. The external covering is strong but is not necessarily airtight. When the bladder is reinforced with an external covering a complete securing mechanism is created. The material chosen for this cover determines the strength of the bag. A material with a higher tensile strength can contain a higher internal pressure. This higher internal pressure exerts a higher securing force per area. Alternatively the same securing force can be produced with less material.

The two common choices for dunnage bag coverings, paper and woven polypropylene, have different characteristics. Paper is light, strong and flexible. It can be coated to add protection from chemical attack. Polypropylene tapes are woven into large tubes and stitched into pillows that provide high strength water resistant coverings.

There are several advantages to using inflatable dunnage bags. They are flexible, so can be positioned in non-standard voids, or voids with dimensions

that are unknown before packing. They are low weight, which gives them an advantage over conventional dunnage. They are not subject to the quarantine and duty issues related to the importation of timber products. However, inflatable dunnage bags are not puncture resistant, so the void to be filled must be free of sharp edges.

1.3 Project Description

Stellenbosch University was approached by Stopak, a company specializing in securing cargo, to provide design tools for the development and testing of dunnage bag concepts. A project was undertaken to develop understanding of the physics behind dunnage bags in order to improve product quality.

Stopak has a two-pronged approach to product design, namely design incorporating evolutionary adaptation, such as changing valve position or materials, and new product design, such as new geometries and the incorporation of new technology. Both branches of product development require that new designs be tested. In many cases new designs will require new tooling or manufacturing processes, the implementation or manufacturing of which is expensive and precludes testing of many concepts.

Stopak requires an alternative to physical testing during the conceptual phases of design. This testing alternative should be suited to extracting general trends, which can be used to evaluate and compare concepts before investing in prototypes. This will increase the number of designs that can be considered while reducing the number of prototypes required for physical testing.

This project endeavors to satisfy these requirements through the development of a computer-based numerical model.

1.4 Project Objectives

The target outcome of this project is to produce a virtual simulation of a static burst test performed on sample paper dunnage bags. A typical burst test is done on a large, press-type, rig. The test rig has two horizontal plates of which one is fixed in space. The gap between these two plates can be varied and maintained during a test. For a particular test the gap size is fixed and a sample bag is inflated between the plates until the bag fails by bursting.

In order to meet the project requirements, the conditions of the simulation and the sample dunnage bag should be matched. The simulated test would have a dunnage bag inflated between two rigid plates. The bag must make contact with the plates and conform to their geometry as it is inflated, a method of representing the air inflation must be found and the sample should be matched in material properties, geometry and components.

The project objective is to create a virtual environment for preforming static burst tests on paper dunnage bags. This environment must,

- include a representative material used to manufacture the dunnage bag
- include a representative means of inflation
- reproduce the inflated shape of the dunnage bag within a given void
- show the stress trends associated with the inflated shape
- allow for various void sizes and shapes
- be compared to physical tests

1.5 Simulation Requirements

In order to meet the project objectives there are some general requirements that should be met. The simulation will require a representative geometry, a mechanism allowing full inflation, an accurate material model and external contact. Later requirements may include multiple layers, the inclusion of a bladder, contact friction and failure simulation.

Building this virtual model requires some early assumptions. The exterior paper covering of the dunnage bag, with its punched hole and plastic valve, are the important components for this simulation. The bladder was excluded from the model because it adds very little structural strength and requires a complex contact interaction between itself and the paper covering.

Large deflections are expected during inflation and the dunnage bag makes contact with another body at some point during inflation. These two model characteristics necessitate the use of a simulation code capable of nonlinear analysis. The physical bags are inflated with a volume of air. The inflation by volume was replaced with inflation by a surface load, representative of the internal pressure, which will reduce the computational complexity of the simulation considerably.

Numerical simulation were done using a commercial finite element package.

Chapter 2

Considerations for Numerical Modeling of Inflatable Dunnage Bags

Numerical modeling brings with it several complexities. Some physical parameters cannot be matched using the tools a particular software package can provide. To match the physical parameters with the chosen software package, assumptions must be made. Potential problems should be identified, before a model can be built. Complexities such as model nonlinearity and computational constraints are considered.

When nonlinear characteristics are required from a model the computational requirement of the simulation is greatly increased. Linear analysis requires only a single calculation to be done. In order to run a nonlinear analysis, the simulation is broken into a series of increments that are individually linear. A linear analysis is done for each increment. At the end of each linear analysis, the model geometry is updated. Using this new geometry, new load conditions are calculated and another linear analysis is done. This process is repeated to complete the analysis.

This chapter will discuss expected problems resulting from material, geometric and boundary nonlinearity as well as some software-related issues. Possible solutions to identified issues are then discussed.

2.1 Material Nonlinearity

The dunnage bags used in this project have a kraft paper covering. This exterior covering is the focus of the simulations, and a good understanding of the material is vital to the accuracy of the model.

Paper is a complex engineering material, with several nonlinear properties that can affect the results of a simulation. As the model is intended to simulate inflation to near failure, as complete a material model as possible is required.

Some general paper properties are listed here to put the additional com-

plexity introduced by this material into context. Chapter 3 is devoted to the discussion of paper and the modeling thereof.

- The stress-strain relationship is nonlinear
- Paper exhibits different material properties for tension and compression
- Notable plastic deformation is exhibited
- Creep and stress relaxation are evident
- Elastic properties are time rate dependent
- Plastic properties are time rate dependent
- Orthotropic yield values are codependent

To simplify the simulation it is assumed that loads are applied slowly, under controlled humidity and temperature. Temperature and humidity are complex to model but their effect is important for a complete model as the operating conditions for dunnage bags include high load rates, large variations in temperature and humidity. This project intends to lay the foundation for further modeling and intends to extract only general trend information.

2.2 Geometric Nonlinearity

The inflated shape of a dunnage bag is largely application dependent. The flat rectangular bag is positioned and inflated to conform to the shape of the cargo it is securing. To widen the application of the virtual model it was decided that it should also have this capability. This suggests that the inflated shape of the dunnage bag is unknown before the simulation starts. The virtual model is inflated and the paper covering undergoes a significant shape change. This change in shape has ramifications throughout the simulation.

2.2.1 Large Element Rotations

When the virtual model is inflated the shape of the bag changes, becoming more spherical. As the bag's shape changes so does the relative position of the elements in the discretized model. The elements of the model translate, rotate and deform as the structure is loaded. Rigid element rotation is a source of nonlinearity in numerical simulation. During the early stages of inflation many of the elements in this model undergo this type of rotation. This simulation will be solved using small iterations. As these iterations follow each other sequentially, without feedback, the errors compound and cause the model to become unstable. To combat instability smaller increments are taken, increasing the computation time for a simulation.

2.2.2 Model Geometric Instability

The initial geometry for the model is a thin, flat, rectangular sheet with a load perpendicular to the internal surface. Due to the difference in dimension between the geometry and the material thickness of the bag, the model has a very low bending stiffness. This property is necessary for the easy inflation of the bag, but reduces the stability of the numerical model.

The initial model configuration requires the applied pressure to be perpendicular to the flat paper sheet. In this direction the sheet has a very low stiffness, so a very small applied load causes a large displacement. With an incremental solver each increment is linear. If there is a large displacement in an individual increment, that solution is unlikely to be accurate and the sequential nature of the solver will cause the numerical solution to become more and more unstable with each increment. This instability leads to the solver not converging to a solution. In order to produce a more stable model, a smaller increment is required and the computational time will increase.

The initial instability of the model is overcome through two mechanisms as the bag inflates. Firstly, the shape of the model changes in such a way that more of the energy input through internal pressure is dissipated through in-plane stiffness than bending stiffness. Secondly, when the model inflates to the point where it comes into contact with the rigid plates, the stiffness of those plates becomes dominant in the contact region.

Though the model is stable in its final state it must still pass through an unstable period with the potential to inhibit convergence.

2.2.3 Wrinkling

Wrinkling is a phenomenon visible in thin materials under loading. Wrinkles involve large deformations of naturally thin flat sheets [Cerda and Mahadevan (2003)]. In dunnage bags, paper can be considered to be a membrane, which has an extremely low bending stiffness and can buckle easily despite a small compression force [Bletzinger *et al.* (2007)]. Local buckling of the membrane allows a compressive force to be faded out by out-of-plane displacements [Jarasjarungkiat (s.a.)]. Wrinkles form along the edges of a dunnage bag as it inflates. Wrinkling is more prominent in models with large gap sizes, where the gap size is the distance between two parallel plates defining the void size. Wrinkling produces complex stress patterns in models, combined with intricate deflection patterns influencing the distribution of internal pressure. Blandino *et al.* (2002) shows some stress patterns associated with wrinkling. These wrinkle patterns should be modeled as well as possible to limit the effect of these patterns on the overall stress pattern. Capturing these effects require a finer mesh. Higher mesh densities are computationally more demanding.

2.3 Boundary Nonlinearity

Once the material properties and the geometry of the model have been defined, the interaction of the model with its environment must be modeled. Two interactions will be modeled, the pressure used to inflate the bag and the contact made with the external rigid plates. Both of these necessitate a nonlinear iterative solution.

2.3.1 Displacement Dependent Loading

A surface pressure is used in this simulation to inflate the virtual dunnage bag. This pressure is used in place of the compressed air volume present in the physical bags. The assumption of an internal pressure is a good approximation at full inflation but is less stable during the initial stages of inflation. Pressure load vectors are dependent on element orientation. With the model undergoing large deformations, this load vector must be recalculated after each linear iteration. Increment sizes must be small enough for a linear assumption to be true throughout the increment step.

2.3.2 Contact

The dunnage bag makes contact in four places during the simulation. The first is the contact made with the external rigid plates. This contact has an influence on the shape the bag conforms to. Later models may have friction on this contact interface. With each increment the solver checks whether or not individual elements are in contact and applies a constraint on the nodes of the element concerned.

The second contact is made at the glue lines that bond the paper sheet into a pillow shape. This contact interface requires that the nodes on either side of the sheet be bonded together in some way. The interface should be able to show the different material property of the glue itself.

Contact is also made where the paper sheet overlaps at the glued seams. They may not contribute much to the stiffness of the structure but they may produce a point from which failure can propagate. To improve accuracy, these effects will be included in the model.

The fourth contact in the simulation is that of the inflation valve with the main body of the bag. The valve is kept in position and presses into the paper. Self contact is not considered in this model, it is complex to include when the contact areas are unknown as two contacting parts must be defined. Self contact is only seen in samples inflated into lager voids or where no constraint is applied. Since this is not the operating condition for the bags, the definition of self contact will provide no added accuracy.

When there is contact at a point in the simulation other than at the beginning an iterative solution will be required. The addition of this contact checking procedure adds to computation time.

2.4 Finite Element Analysis

A finite element code was used to build a virtual model of the inflating dunnage bag. An iterative solver capable of nonlinear solutions was required. There are two major types of nonlinear code available, implicit and explicit solvers. Each of these code types have their own advantages and disadvantages and Stellenbosch University has access to both types of code.

When a nonlinear problem is approached using finite element methods the solution is approached incrementally. At the end of each increment the geometry, loads and material properties are changed and the stiffness matrix is updated.

Explicit solvers apply a load increment and update the stiffness matrix based on the changes this load makes to the model conditions. The next load increment is applied to this updated stiffness matrix. For an accurate solution a small increment is required. This requires more increments and a longer solution time. If the increment size is too large the solution will drift from the actual solution. Explicit solvers do not enforce an equilibrium between the externally applied loads and the internal structural forces. Explicit solvers are not recommended for analysis including cyclic loading or where snap back, snap through characteristics are expected. Examples of analyses run in explicit codes include car crash analysis and airbag inflations.

Implicit solvers do enforce an equilibrium between the externally applied loads and the internal structural forces. Newton-Raphson iterations are done to balance these forces to within a user-defined tolerance. This closed loop analysis makes the incremental solutions more accurate and as such, larger increments can be used for the analysis. An additional benefit of implicit solvers is that different control methods can be used to reach the desired equilibrium, such as load, displacement or arc length control. A disadvantages of the implicit solver is that each iteration of the Newton-Raphson method requires the reconstruction of the stiffness matrix. Examples of analysis run in implicit codes are the simulation of punching and forging operations.

Initially the implicit code MSC.Marc [MSC (2000)] was used to simulate the bag inflation, but a stable model that included all the parameters could not be produced. It was decided to switch to an explicit solver, LS-DYNA [Hallquist (2006)].

Chapter 3

Material Properties of Paper

Paper is a commonly used engineering material. It is used in several different manufacturing areas, from printing to packaging and even has some structural applications. In this project machine manufactured kraft paper is used as the external stiffening material for the dunnage bag. Material properties are of critical importance to nonlinear finite element analysis. This chapter covers the material properties of paper in general as well as the material model used.

3.1 Introduction to Paper

Haslach (2000) describes paper as a network material comprised of cellulose fibers, (a natural polymer composite). The manufacturing process begins with a low concentration solution of discrete wood fibers in water, composed of between 0.5 and 1% pulp fiber. This fiber suspension is sprayed onto a moving wire mesh. A difference in speed between the sprayed solution and the wire mesh leads to the orientation of fibers along the direction of motion of the wire mesh, machine direction. Excess water drains through the mesh and the resulting sheet is then pressed and dried. The result is a fiber network held together by inter-fiber hydrogen bonds, which does not require any matrix material to maintain cohesion. As a standard practice the natural preferred fiber direction is used as a basis for describing the properties of the paper. The three principal material axes for paper are the machine direction (MD), the cross direction (CD) and the through plane direction (ZD), Fig. 3.1. The MD and CD are considered to be in-plane directions while the ZD is considered to be the out-of-plane direction.

3.2 Mechanical Properties of Paper

"Paper is one of the most complex of the engineering materials" [Haslach (2000)]. It is important that the mechanical properties of paper are understood before starting a simulation. Paper has several mechanical properties that should be considered, the most important of which are explained below.

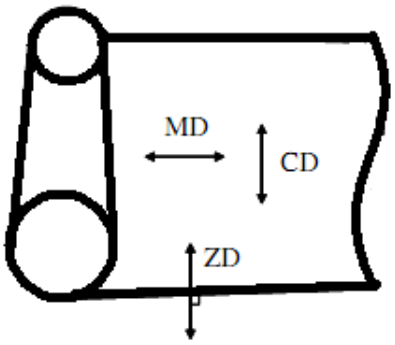

Figure 3.1: Principal material directions for machine manufactured paper. Machine direction (MD), cross direction (CD) and through-thickness direction (ZD). [Mäkelä and Östlund (2003)].

3.2.1 Material Property Orientation

Jones (1967) shows that although paper is a heterogeneous anisotropic material, it can be observed to have a preferred fiber orientation. When paper is loaded predominantly in-plane it can be considered to be an orthotropic material, with three mutually perpendicular planes of material symmetry. Each of these symmetric planes have different material properties. Results from material testing of paper show this to be a fair assumption on the macro scale [Baum *et al.* (1981*b*)]. This assumption can be used in most situations with the exception of small scale deformation, such as folding of a paper sheet.

To define a linear elastic orthotropic material requires nine material constants for a linear elastic model. This is significantly more than the two material properties required to define a linear elastic isotropic material. An orthotropic material can be defined either by its engineering constants E_1, E_2, E_3, (the Young's moduli in the three principal directions), ν_{12}, ν_{13}, ν_{23}, (the Poisson's ratios for the three principal directions), G_{23}, G_{13}, G_{12}, (the shear moduli for the three principal directions), or the C_{ij} values from the stiffness matrix. The stiffness matrix is a common way of defining linear elastic paper because it is easy to generate a complete set of constants by means of sound propagation techniques [Baum *et al.* (1981*b*), Baum (1981), Baum (1984) and Mann *et al.* (1979)].

3.2.2 Stress-Strain Relationship

Paper exhibits nonlinear mechanical behaviour, observed in its linear elastic response to moderate loads and non-linear plastic response to higher loads [Johnson and Urbanik (1984) and Suhling *et al.* (1989)]. Figure 3.2 shows a characteristic stress-strain relationship for machine-manufactured paper. This figure shows the non-linear nature of the stress-strain curve for paper and

the differences in properties between tensile and compressive loading. This difference between tensile and compressive properties may become a dominant factor in a complex load cycle.

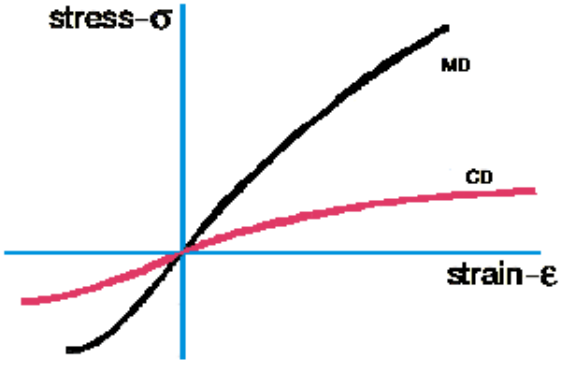

Figure 3.2: Machine direction (MD) and cross direction (CD) stress-strain curves of a paper sample [Jimenez-Caballero *et al.* (2009)].

3.2.3 Material Plasticity

Both Xia *et al.* (2002) and Mäkelä and Östlund (2003) put emphasis on paper experiencing visco-plasticity, and the importance of its inclusion for an accurate material model for paper. Visco-plasticity describes how the material undergoes partially unrecoverable material deformation when under applied stress. The rate at which this stress takes place affects what portion of the total deformation is permanent. It follows that the plasticity of paper is time-rate dependent. This is also observed when paper exhibits creep and stress relaxation [Haslach (2008) and Haslach (2000)], important in corrugated board. A typical load-unload curve for paper shows how paper loads elastically but unloads plasticly, Fig. 3.3. Plasticity allows paper to change its physical structure to accommodate high local stresses. Paper can experience significant plastic deformation and this will play a role in all but the simplest analysis of paper.

3.2.4 Material Elasticity

Many material models describe the low stress, low strain properties of paper as being linear elastic. The measurement of these elastic properties of paper are described in several papers, most notably Jones (1967), Mann *et al.* (1979), Baum and Habeger (1980), Baum (1981), Baum *et al.* (1981*b*) and Baum (1984). These elastic properties of paper are highly dependent on several factors, most importantly material orientation and time. Paper is as such considered to be visco-elastic. This means that the observed stiffness of paper can vary depending on the type of load being applied [Haslach (2008) and

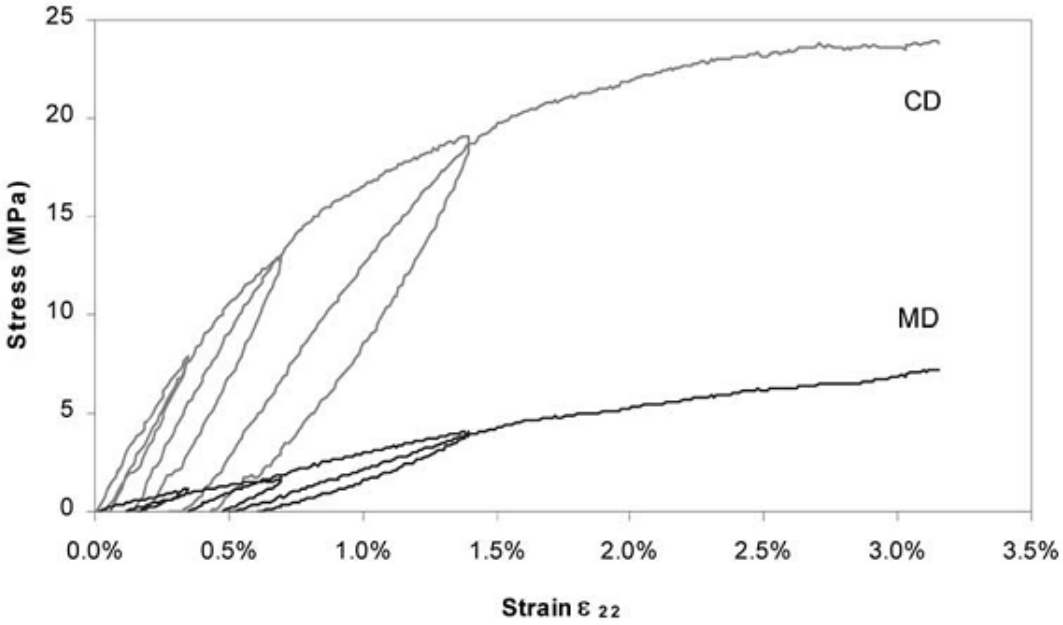

Figure 3.3: MD and CD stress-strain curve for biaxial cyclic loading and unloading [Castro and Ostoja-Starzewski (2003)].

Haslach (2000)]. Figure 3.4 shows a typical comparison of the fracture loads for paper with various load rates.

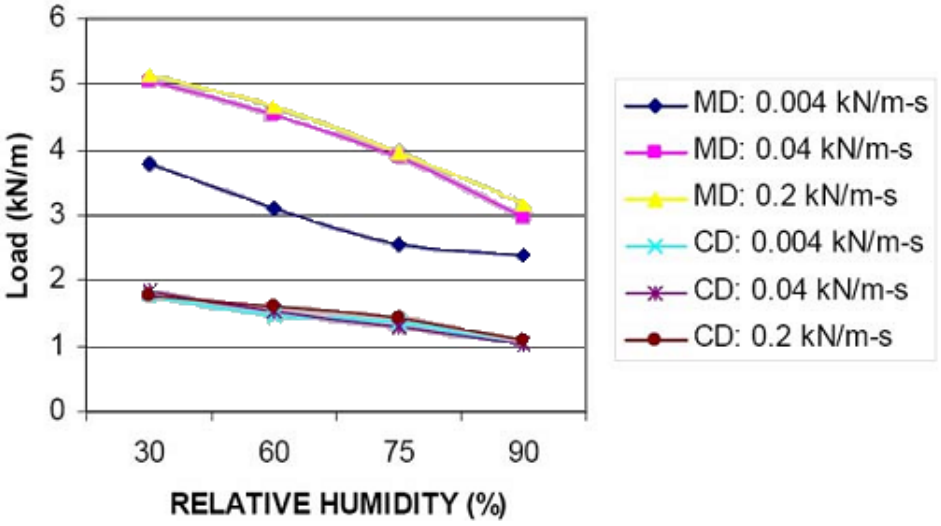

Figure 3.4: Paper fracture loads at various humidities and load rates [Haslach (2008)].

3.2.5 Moisture and Temperature Dependence

Haslach (2000) gives an in-depth review of the moisture and rate-dependent mechanical properties of paper. In a discussion of related results, the author shows that there is a significant change in the mechanical properties due to changes in humidity. Haslach (2008) shows that for a given paper at given load rate, the maximum failure load can change as much as 30% with varying humidity. Humidity has a similar effect on the maximum strain at failure. Unlike many engineering materials, humidity plays a more prominent role in the material properties of paper than temperature. Haslach (2000) also states that there is no conclusive evidence that the effects of temperature and humidity could be isolated from each other by holding one at a constant value. This means that these two factors should be considered simultaneously in an analysis.

3.2.6 Summary of Important Paper Properties

- Paper can be considered to be an orthotropic material
- Paper exhibits a nonlinear stress-strain relationship
- Paper exhibits significant plastic effects
- Paper exhibits creep and stress relaxation
- Paper's elastic properties are time-rate dependent, showing visco-elastic and visco-plastic effects
- The mechanical properties of paper are sensitive to temperature and humidity variations
- Yield values for paper are codependent

For testing of paper products one should consider the relevance of each of these nonlinear properties. The relevance of these properties must be reevaluated regularly during an analysis. Ideally as many of these properties as possible should be included from the earliest stages [Jimenez-Caballero *et al.* (2009)]. Appendix A discusses the material models considered for this simulation.

3.3 Modeling of Kraft Paper

The primary material used in this model is kraft paper. The paper is supplied by Mondi Steti, and, on request, a sample material test data was sent. Figure 3.5 shows sample data for a tensile test performed on a 100×15 mm sample. The sample shown is for multiple tests performed in the machine direction.

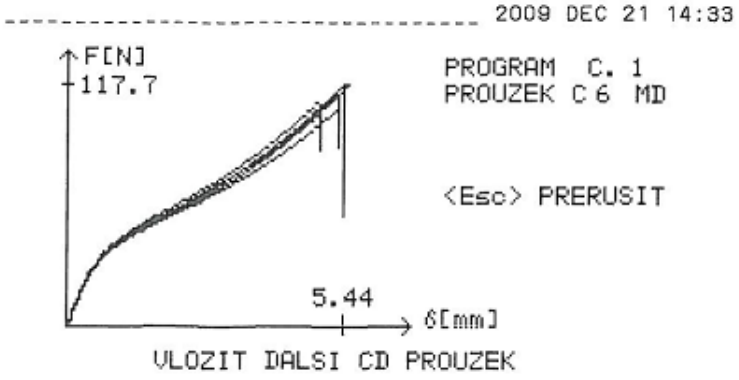

Figure 3.5: Kraft paper material tensile test sample data, applied load vs. elongation, provided by Mondi Steti.

The data presented shows the nonlinear nature of paper. It was decided that for this model a bilinear material model, described in Appendix A.7, will be used. Saliklis *et al.* (2003) proposed an orthotropic bilinear material model. This material model prescribes that the three mutually perpendicular material directions each have their own bilinear stress-strain curve, with a secondary requirement that they be codependent. Results for a biaxial tensile test are required to define these curves. In the absence of this data it was decided that an isotropic bilinear material model be used.

LS-DYNA has many material models, of which the most appropriate, for this model, is an isotropic elastic-plastic material with kinematic hardening. Young's moduli for the elastic and plastic regions were derived from the data provided by Mondi Steti. The slope of the force-displacement curves in the elastic and plastic regions were recorded. Using these slope values and the dimensions of the samples, elastic moduli for the elastic and plastic regions were found. These values were found to be in line with those found in some literature. The material was defined as having a elastic modulus of 3 GPa in the elastic region and 1.5 GPa in the plastic region.

Chapter 4

Building a Base Numerical Model

The building of a numerical dunnage bag model was approached systematically. Parameters were added one at a time and a stable method of simulation was determined before further parameters were added. Initially the solver, MSC.Marc was used for this model, but during the development of the model several problems arose.

The time taken to complete an analysis, the runtime, increased disproportionately to increasing model complexity. For instance a 20% increase in mesh size would result in runtimes increasing from a number of hours to several days. With the inclusion of a non-zero Poisson's ratio the model became unstable. Due to these problems, the model was rather developed for LS-DYNA.

LS-DYNA was originally excluded because explicit codes typically have longer runtimes than implicit codes for models with a longer analysis times. LS-DYNA is used to model short duration events such as impact. It also solves a dynamic problem, making it less suitable to quasi-static analysis than implicit codes such as MSC.Marc.

4.1 Base Model Requirements

A stable test model with a suitable capacity to be adapted to the geometry and materials of the physical model was first developed. This test model was also used to perform an initial study of the model parameters.

A series of sensitivity analyses were run on the test model to investigate the effect of each simulation parameter. These analyses included investigating the effects of analysis time, artificial damping, mesh density, Poisson's ratio and material density on the model characteristics.

4.2 Stabilizing the Base Model

A set of specifications for a similar problem were taken from Wu and Ting (2007). These authors focused on the development of a new element type. For the purpose of this project a model with a known solution was valuable.

The model from Wu and Ting (2007) is a flat plate undergoing large deformation due to a pressure load applied to one side. The plate is held in position by symmetry constraints along each edge. The model specifications are shown in Table 4.1.

Table 4.1: Test model specifications.

Model Type	$\frac{1}{2}$ Symmetry Model
Dimensions	1×1 m
Material Model	Linear Elastic Isotropic
Young's Modulus	6×10^9 Pa
Poisson's Ratio	0.267
Material Density	1×10^{10} $\frac{\text{Kg}}{\text{m}^3}$
Shell Thickness	1×10^{-3} m
Maximum Pressure	$1,5 \times 10^6$ Pa

Though the model specifications were supplied, the authors give little indication of how to approach the analysis. The density used in this simulation is much higher than is physically feasible. This high density was assumed to be a form of mass scaling, increasing the mass of the model to reduce unwanted dynamic effects. For a low velocity analysis, a higher density reduces dynamic effects by reducing the acceleration of nodes when subjected to a given load.

4.2.1 Time Scale Factor and Load Application

In the model described above, pressure was initially applied linearly over the total analysis time, the time in the simulation. The model became unstable and failed before the prescribed simulation termination time, citing nodal velocities exceeding allowable values. In this situation the LS-DYNA support site recommends reducing the time scale factor (TSSFAC, under the keyword *CONTROL-TIMESTEP). This parameter controls how much the time step can be increased or decreased between increments. Through a trial and error approach the TSSFAC value was set at 0.5. This means that from one increment to the next the time step cannot change more than half the previous time step. This TSSFAC value gives the best stability with the shortest runtime.

Once the model was capable of running to completion, the results where seen to be greatly affected by the application of early pressure. To correct this, the pressure was applied more realistically, by replacing the linear load application curve with an exponential curve.

A certain volume of air is pumped into the physical bag to inflate it. Initially the pressure remains low and the bag undergoes large deformation. As the bag approaches full inflation a small volume of air added produces a much more rapid increase in internal pressure. This exponential inflation is modeled

using,

$$P = K_1 e^{\frac{\text{ANALYSIS TIME}}{K_2}} - K_1 \tag{4.2.1}$$

where K_1 and K_2 are constants to calibrate the equation. K_2 scales the pressure curve over the analysis time. This allows the time at which maximum pressure is reached to be set, while maintaining the inflation curve shape. K_1 scales the maximum pressure to the desired value. Figure 4.1 shows a characteristic pressure load curve.

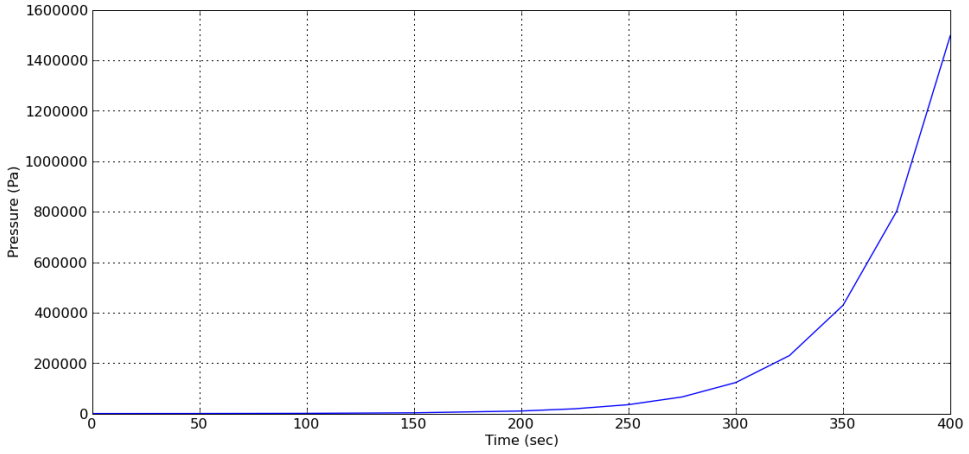

Figure 4.1: Pressure load vs. time for the simulated model.

A benefit of this pressure load curve is an increase in simulation stability. The model is allowed to inflate and take on a more stable geometry under low pressure, then the pressure is ramped to the desired value. With a linear pressure load curve, the magnitude of the force applied to the sheet exceeds the through-plane stiffness of the sheet, leading to numerical instability in the beginning phase of inflation.

Use of the exponential load curve improves, but does not eliminate, the unwanted dynamic effects present in the simulation. Figure 4.2 shows the displacement of the center node of the square plate over time when subjected to an exponential pressure load.

4.2.2 Analysis Time and Global Damping

The updated time scaling factor and load curve allow the model to complete a stable run, but there are still unwanted effects present. For a model to be quasi-static there should be no time dependent effects, Fig. 4.2. This may require that loads be applied slowly enough to avoid oscillatory effects. The analysis time was increased to reduce the unwanted dynamic effects. The load application occurs over a longer time and and inertial effects are removed.

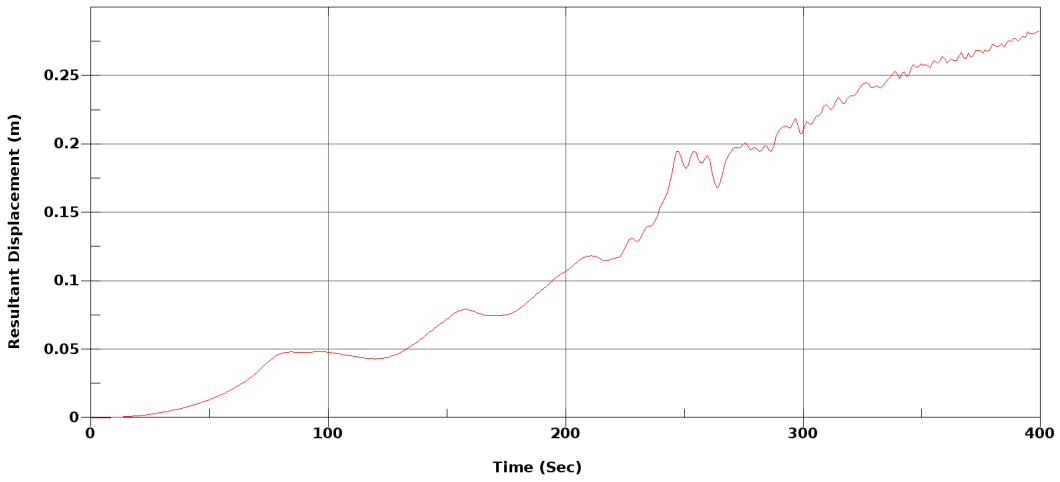

Figure 4.2: Center node displacement vs. time with initial oscillation over 400 seconds

Figure 4.3 shows the same simulation with the analysis time increased to 6400 seconds.

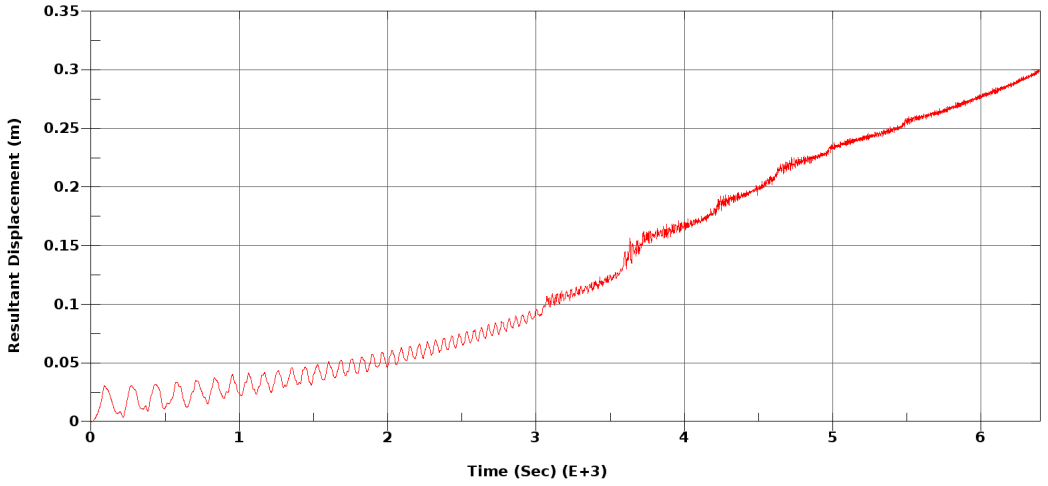

Figure 4.3: Center node displacement vs time with initial oscillation over 6400 seconds.

The same oscillation is present in both cases. The oscillation increases in frequency and reduces in amplitude as the pressure load increases. This is expected, as the increasing in-plane tension and change in geometry produce a structure that increases in stiffness over the inflation time. With an increase in stiffness, the natural frequency of the body increases. It is important to note that the frequencies are consistent between the two figures, not the number of oscillations. The frequency is found to be around 0.013 Hz for the first

half of the simulation. The frequency of the oscillation for each simulation was consistent without an applied oscillatory source. It is concluded that this frequency is then a property of the model. The model is put into this oscillatory state due to the load condition.

The simulation starts with the bag flat and unstressed. A pressure load is then applied in the direction that the plate has the least stiffness and oscillation begins. The magnitude of this effect can be reduced by applying a pretension to the model, either as a pretension setting or by adding a pre-tensioning phase. These options would reduce the effect of the oscillation by reducing its initial magnitude and increasing its frequency. The oscillatory nature would still be present, but it would have less of an influence on the results. It was decided to avoid these methods as they do not represent the condition of the physical bag.

Both figures show a change in the center node displacement over time trend around the mid time of the simulation. This stagnation point in center node displacement coincides with the formation of wrinkles. As the bag inflates, the displacement increases to this stagnation point where the displacement slows before increasing again. This effect should be maintained in the analysis, because it is present in the physical model. Several similar effects can be seen in the model, caused by wrinkle migration and wrinkle mode changes. These physical phenomena should be present in the final model.

In order to get rid of the unwanted early oscillation, an artificial global viscous damping was added to the model. A series of simulations were run with various analysis time values. These analysis were run first with a global damping value of 0.0. The same analyses were rerun, each time the global damping value was increased and the results evaluated until the oscillation was no longer prominent. Results for damping constants 0.01 and 0.25 can be seen in Fig. 4.4 and 4.5. These figures show that at a global damping value of 0.25 the unwanted oscillation is removed.

Based on the results of simulations where the analysis time and damping constant were varied, an analysis time of 400 seconds and a damping constant of 0.25 were chosen for the simulations. It was found that increasing the analysis time leads to excessive runtimes, while decreasing the damping constant leads to the inclusion of unwanted initial oscillation. The resulting model is stable, not greatly effected by a spurious oscillation and maintains the characteristics of the physical model. In addition, this model has a stress pattern which is does not have large differences between adjacent elements and is reproducible of slightly varied model parameters, requirements of the final model. The specifications for the stable model are listed in Table 4.2. This stable model was used to test the effects of several parameters on the model.

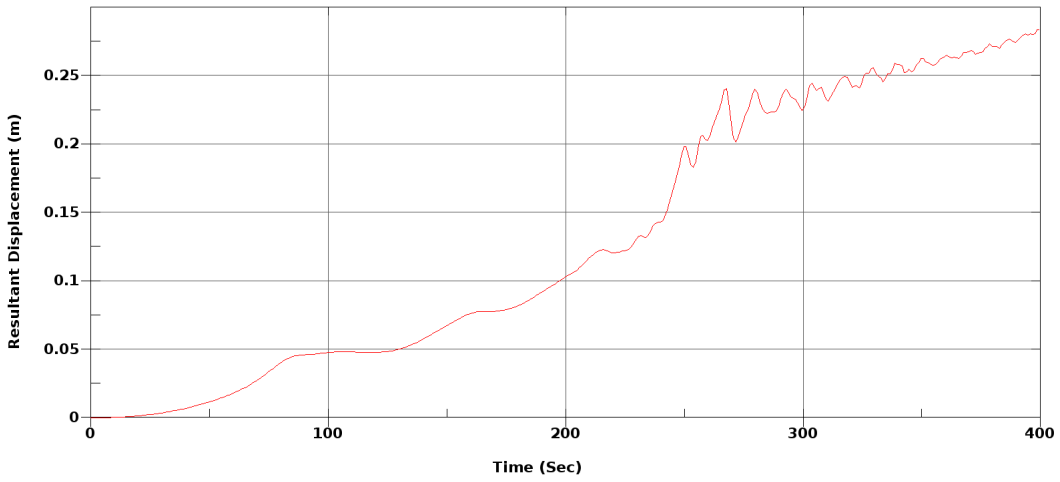

Figure 4.4: Center node displacement vs. time with damping constant 0.01.

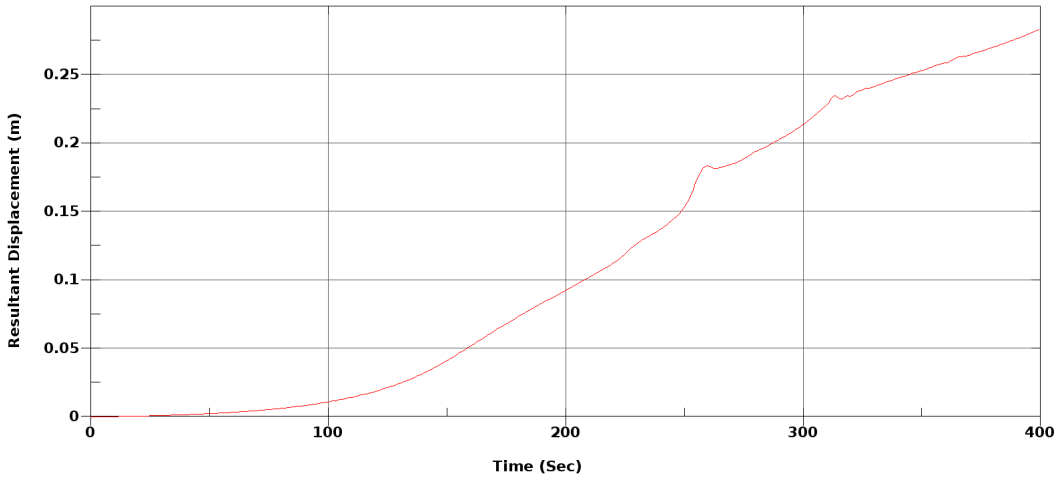

Figure 4.5: Center node displacement vs. time with damping constant 0.25.

4.3 Base Mesh Refinement

The shape of both wrinkles and folds can be mesh dependent. The mesh was refined to find the element edge length that removes mesh dependent effects. The mesh size was determined on convergence of the out-of-plane displacement of the center node and the quality of the visible stress pattern of the inflated bag. By this it is meant that the stress pattern is predictable near the end of the analysis. A stress convergence test was not done at this point. The nodal displacement values are less sensitive to small model variations than stress which made it easier to track between models. The second reason for using displacement convergence and not stress convergence is that the values of the stress at any point in the model are not a concern for this project. Stress

Table 4.2: Stable model specifications.

Model Type	$\frac{1}{2}$ Symmetry Model
Dimensions	1×1 m
Material Model	Linear Elastic Isotropic
Young's Modulus	6×10^9 Pa
Poisson's Ratio	0.267
Material Density	1×10^{10} $\frac{\text{Kg}}{\text{m}^3}$
Shell Thickness	1×10^{-3} m
Maximum Pressure	$1,5 \times 10^6$ Pa
Damping Constant	0.25
Analysis Time	400 sec
Load	Exponential Pressure
Time Scale Factor	0.5

values in this model have large variations between models based on where and how wrinkles and folds form.

A model similar to that described at the end of Section 4.2.2 is used as a basis for mesh refinement. The mesh density was then systematically increased and the effects of the changes evaluated. The simulation set was run with mesh densities between 400 and 28900 $\frac{\text{ELEMENTS}}{\text{m}^2}$.

Figure 4.6 shows the center and mid-side node displacements for a 900 element mesh, where 'B' is the center node.

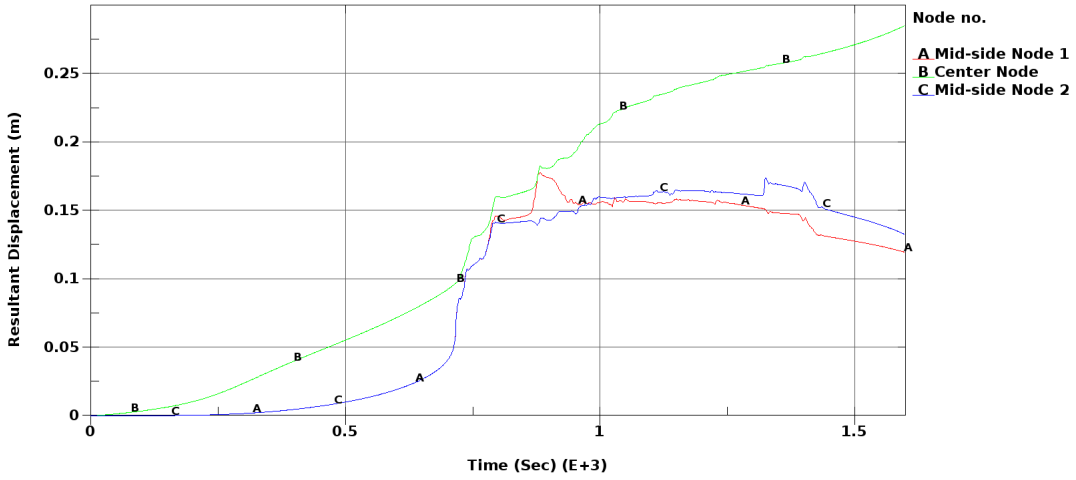

Figure 4.6: Center and mid-side node displacement vs. time for a 900 element mesh.

The model shows large wrinkles along the edges and a final stress pattern with high stress values along diagonal lines between the corners, Fig. 4.7.

The mesh was then increased to 1600 elements. This increase in element density allowed a further phenomenon to occur. A sudden rise in center node displacement occurs near the end of the simulation, Fig. 4.8. As the mesh density increases, the center node displacement is expected to converge to near 0.318 m, the radius of a semi-circle with a circumference of 1m. The rise occurs because the mesh becomes fine enough that the energy required to shift from one wrinkle state to the next, by changing the number of wrinkles along an edge, is reduced to within the potential of the model.

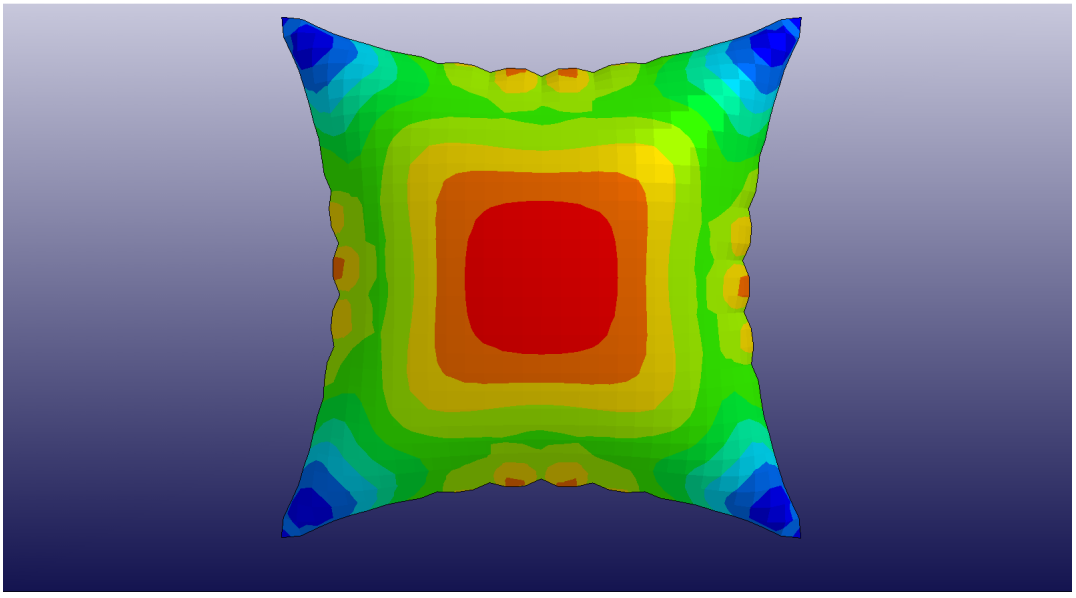

Figure 4.7: The Von Mises stress pattern for an inflated bag with a 900 element mesh, where red is a high and blue is a low stress area.

As the stress in the model increases so does its stiffness, and a higher stiffness produces a shorter wavelength wrinkle. The shorter the wavelength of the wrinkle the lower its amplitude and the less effect it has on the overall stress pattern.

The sudden displacement rise brings a kinetic energy component into the model at the end of the analysis. This may be a problem if the kinetic effects are allowed to dominate near the end of the simulation, as the simulation could no longer be considered quasi-static and the stress pattern would be in question. The magnitude of the kinetic energy is 100 times less than that of the internal energy of the model, and shows no effect on the displacement profile for the simulation. This kinetic energy can therefore be considered insignificant.

As stated earlier, it is expected that as the mesh is refined the maximum nodal displacement for the model should approach 0.318. A series of simulations were run to find the mesh density where displacement converges, Fig. 4.9. Convergence was assumed after the difference in displacement dropped to less

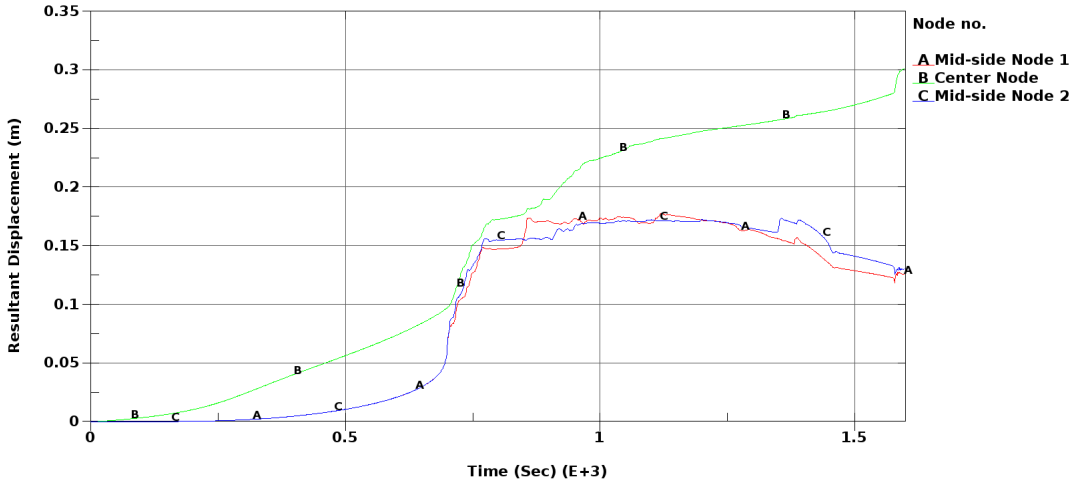

Figure 4.8: Center and mid-side node displacement vs. time for a 1600 element mesh.

than 3% over three sequential test densities. A mesh density of 4900 $\frac{\text{ELEMENTS}}{\text{m}^2}$ was the resulting converged mesh.

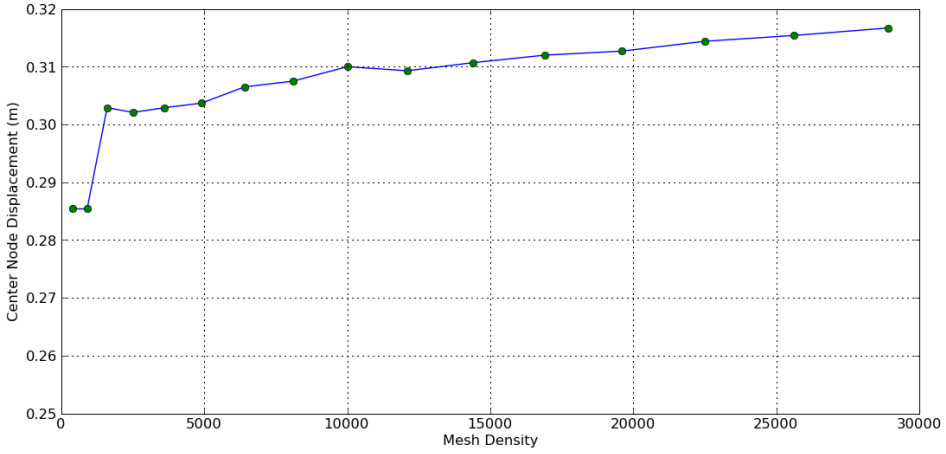

Figure 4.9: Center node displacement vs. mesh density for a 1×1m square bag.

This mesh has a consistent stress pattern. Figures 4.10 and 4.11 show the nodal displacement profile and final Von Mises stress pattern for the 4900 element mesh. A mesh density of 4900 $\frac{\text{ELEMENTS}}{\text{m}^2}$ was used as a base for further models.

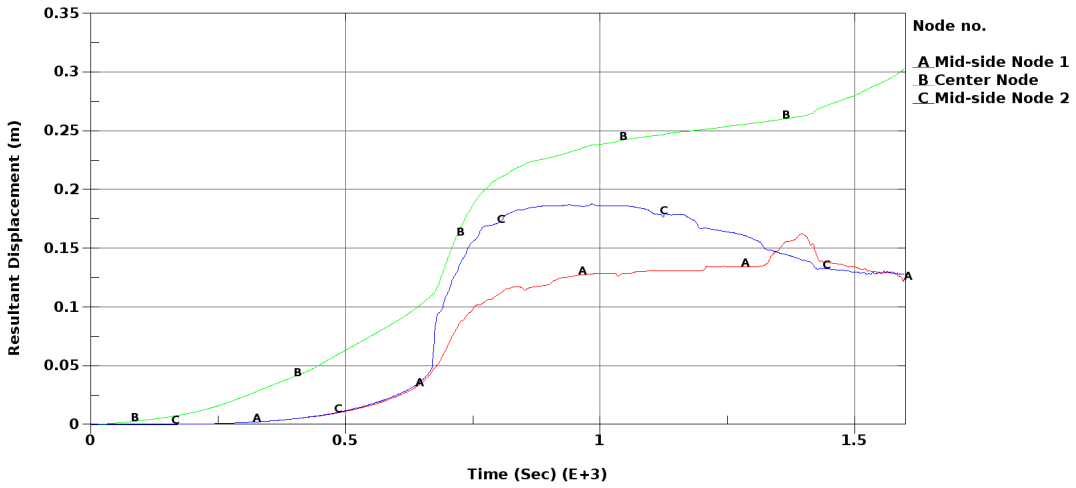

Figure 4.10: Center and mid-side node displacement vs. time for a 4900 element mesh.

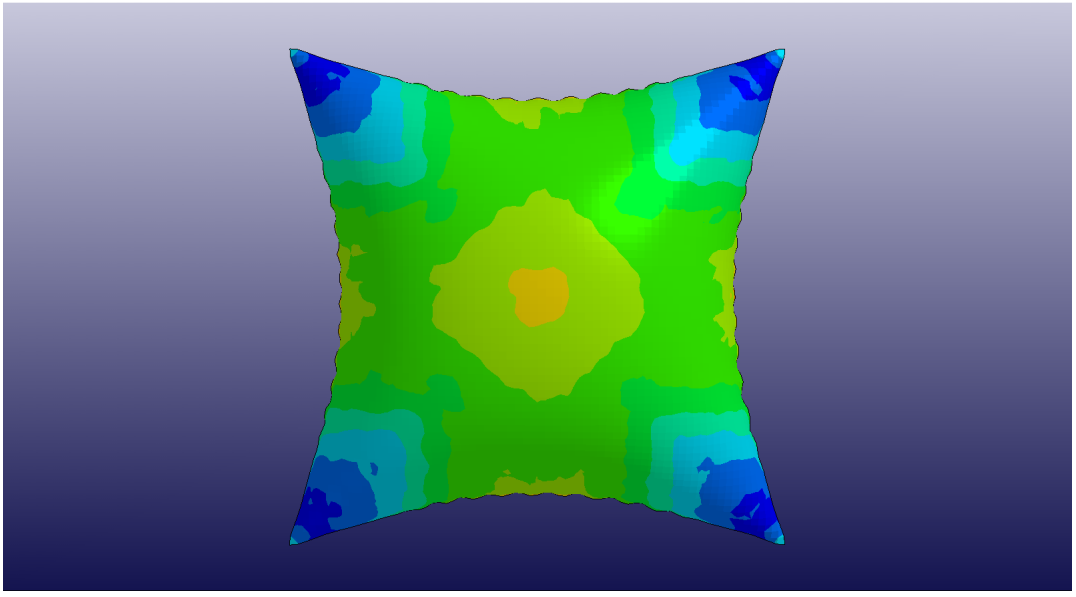

Figure 4.11: The Von Mises stress pattern for an inflated bag with a 4900 element mesh, where red is a high and blue is a low stress area.

4.4 Sensitivity to Poisson's Ratio

The test model was used to investigate how changing the Poisson's ratio of the material affects the simulation results. Poisson's ratio is expected to affect both final geometry and stress pattern. While a wide range of Poisson's ratios for paper were found in literature, no data was available for kraft paper.

The Poisson's ratio was varied between 0.0 and 0.49. Key simulations are presented in Fig. 4.12 through 4.14.

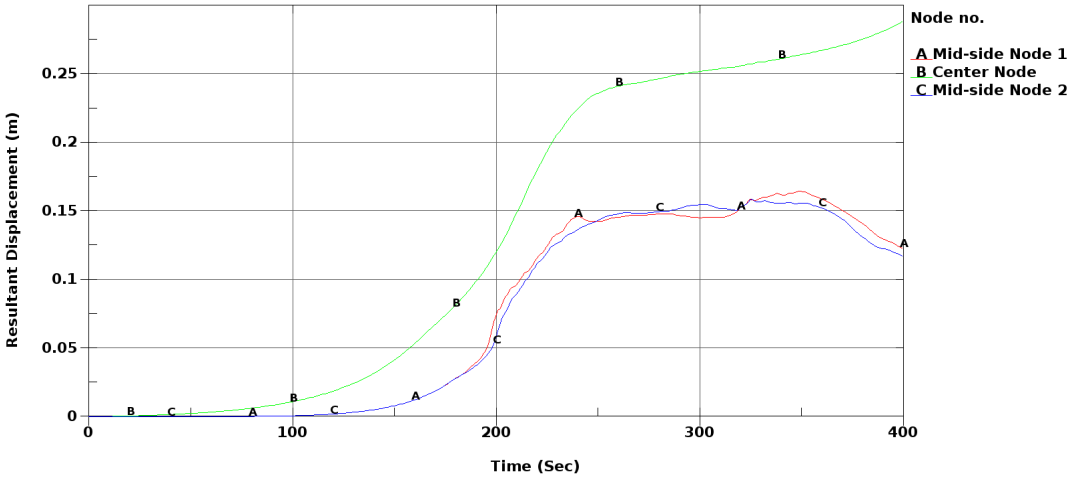

Figure 4.12: Center and mid-side node displacement vs. time with a 0.0 Poisson's ratio.

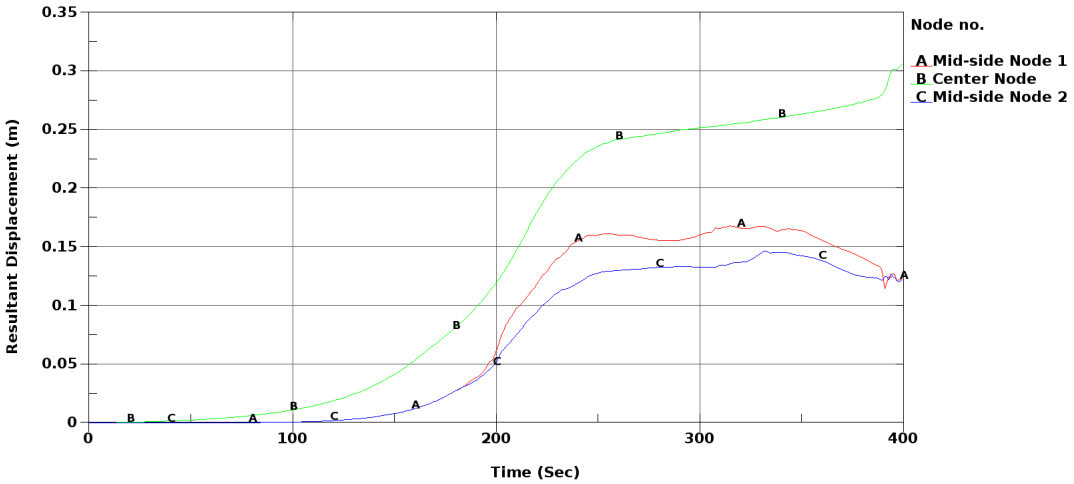

Figure 4.13: Center and mid-side node displacement vs. time with a 0.25 Poisson's ratio.

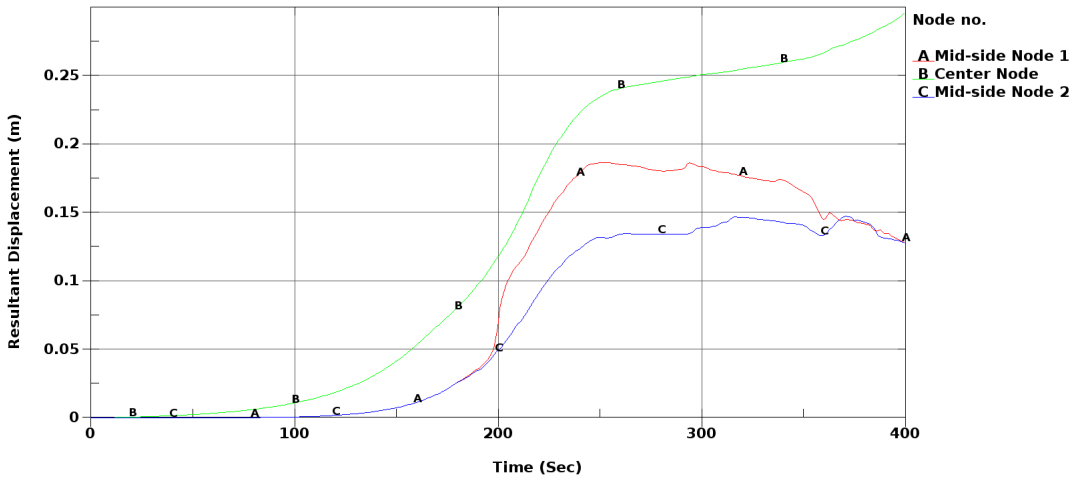

Figure 4.14: Center and mid-side node displacement vs. time with a 0.49 Poisson's ratio.

Observation of node 'B' for these cases reveals a Poisson's ratio dependence in the model. There is a rise in center node displacement, similar to that seen during mesh refinement. This corresponds to a change in the stress pattern as described previously. A check of the part kinetic energy in the models shows that even if the displacement profile does not show a geometric change there is a change, in the kinetic energy in each simulation. For example, the kinetic energy profile at Poisson's ratio of 0.0 shows a spike towards the end of the simulation, Fig. 4.15. Similar spikes can be seen at Poisson's ratios 0.1 and 0.49, Fig. 4.16 and 4.17.

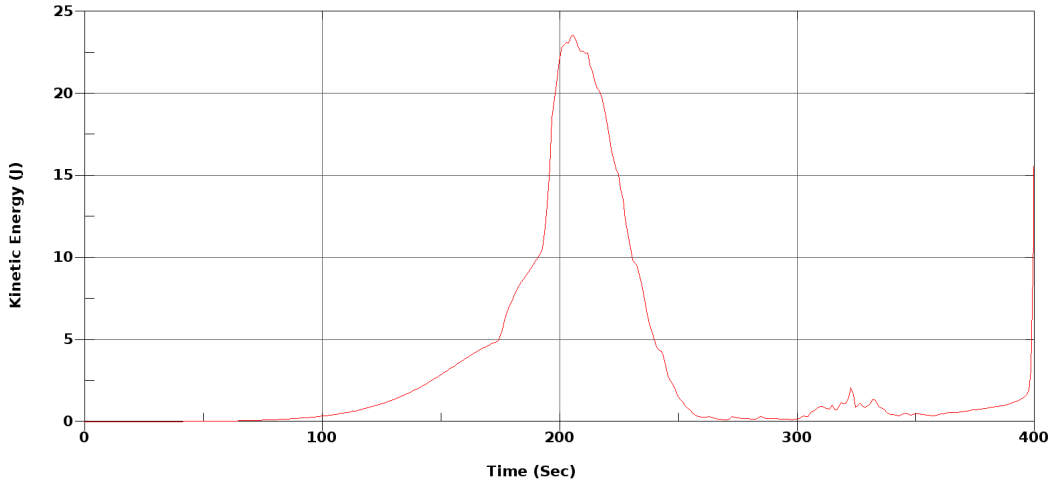

Figure 4.15: Bag kinetic energy vs. time with a 0.0 Poisson's ratio.

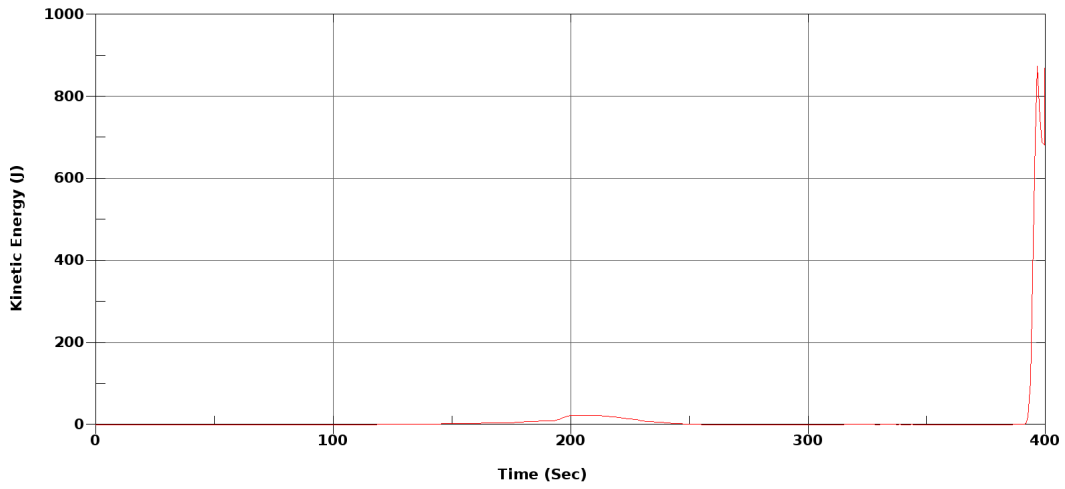

Figure 4.16: Bag kinetic energy vs. time with a 0.1 Poisson's ratio.

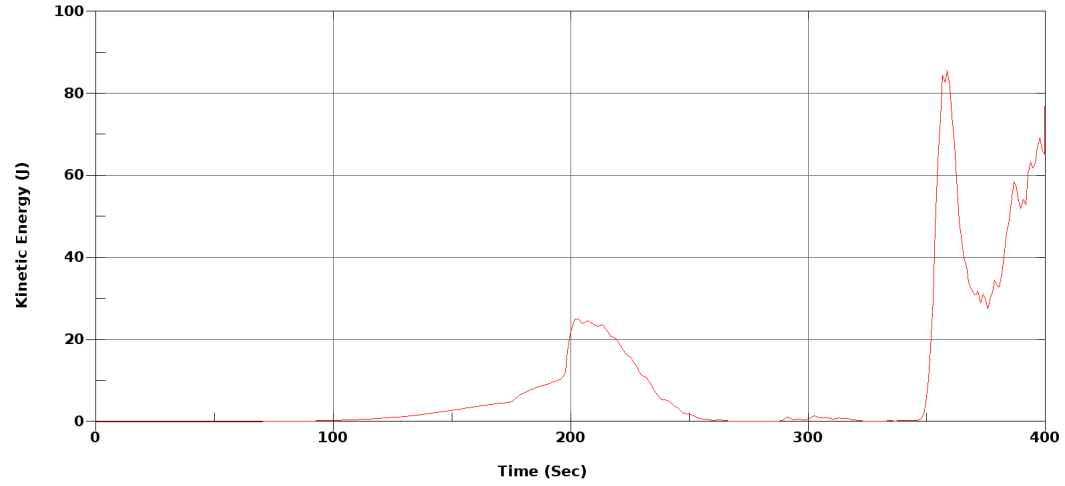

Figure 4.17: Bag kinetic energy vs. time with a 0.49 Poisson's ratio.

When the Poisson's ratio is set greater than 0.1, increasing the Poisson's ratio decreases both the magnitude of the rise in center node displacement and the simulation time at which it occurs. The Poisson's ratio affects the geometry of the inflated bag, Fig. 4.18.

The geometries seen for Poisson's ratios of 0.0 and 0.49 are similar. The geometry for a poisson's ratio of 0.1 has a finer wrinkle pattern along the edges than those at either end of the spectrum. This shows that the model is sensitive to the Poisson's ratio. A value of 0.267 was used in further models. This value was used in Wu and Ting (2007) and is in the mid-range of the possible Poisson's ratios for paper.

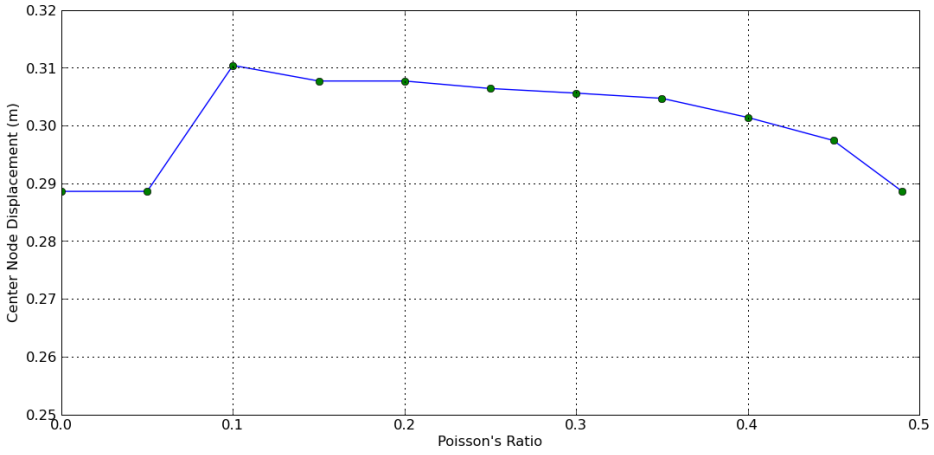

Figure 4.18: Center node displacement vs. Poisson's ratio for a square bag.

4.5 Mass Scaling Effects

Mass scaling was used to reduce unwanted dynamic effects. The effect of density on the model was tested. As the model has been mass scaled, the density used to this point was recommended in Wu and Ting (2007).. The intention was to reduce the density to that of the physical paper. The density used in the simulation was reduced from 1×10^{10} to 1×10^{7} $\frac{\text{Kg}}{\text{m}^3}$ before the model became unstable. Lower densities were not tested as further reducing the density caused significant increases in runtimes.

The test model developed, based on Wu and Ting (2007), was used. It was found that there is no visable change in the final stress patterns between simulations, and that unwanted dynamic effects did not increase significantly. The most significant effect of the changes in density was on runtime, which increased from 435 seconds at maximum density to 12744 seconds at minimum density. The increase in model accuracy, by having a more realistic density, did not warrant this increase in runtime.

4.6 Base Numerical Model

Once a stable model was developed and the sensitivity and effects of its parameters investigated, the model was adapted to more closely approximate the physical system. Geometry, Young's modulus, maximum load and shell thickness were updated for this purpose.

4.6.1 Matching the Physical and Simulated Models

Parameters expected to have the least effect on the model were updated first.

The geometry of the model was adapted first, to match the dimensions of a standard dunnage bag. Changing dimensions from 1×1 m to 1.8×0.9 m increased the number of elements in the model to maintain the desired mesh density, which in turn increased runtimes. No other effects were seen.

The change in Young's modulus from 6×10^9 Pa to 3×10^9 Pa had no adverse effects.

The maximum pressure was reduced from 1.5 MPa to 20 KPa. This changed the final stress pattern from a high pressure hoop stress dominant pattern to a high pressure hoop stress pattern in the middle of the model and a low pressure pattern at the edges.

The test model had a shell thickness of 1×10^{-3} m, and a one ply physical bag was measured to be 1.2×10^{-4} m. To match these parameters a reduction in thickness of an order of magnitude was needed. Typically such a thin shell thickness is a cause of model instability, as indicated by a warning produced in LS-DYNA for any shell thicknesses less than 5×10^{-4} m. The shell thickness was therefore reduced by 1×10^{-4} m at a time. The final thickness of 1.2×10^{-4} m, was reached. The model was evaluated after each reduction to ensure stability. No stability issues were found.

4.6.2 The Base Model

The specifications for the base model are shown in Table 4.3.

Table 4.3: Base model specifications.

Model Type	$\frac{1}{2}$ Symmetry Model
Dimensions	1.8×0.9 m
Material Model	Linear Elastic Isotropic
Young's Modulus	3×10^9 Pa
Poisson's Ratio	0.267
Material Density	1×10^{10} $\frac{\text{Kg}}{\text{m}^3}$
Shell Thickness	1×10^{-3} m
Maximum Pressure	20×10^3 Pa
Damping Constant	0.25
Analysis Time	400 sec
Load	Exponential Pressure
Time Scale Factor	0.5

Figure 4.19 shows the displacement of the center node over the duration of a simulation. No unwanted oscillation effects can be seen. Considering the exponential load application curve, the geometry is near its full inflated shape before the bulk of the pressure is applied. This correlates well with the physical model.

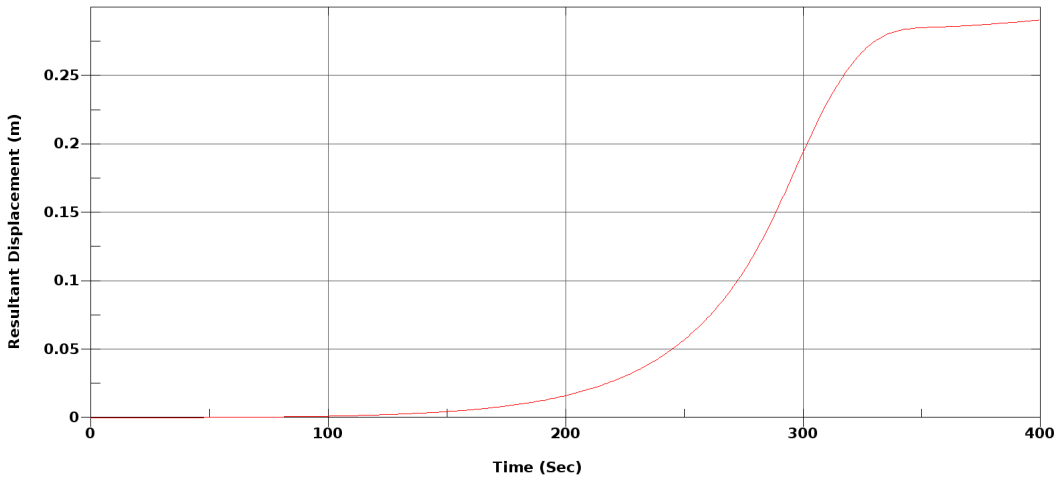

Figure 4.19: Center node displacement vs. time for the base model.

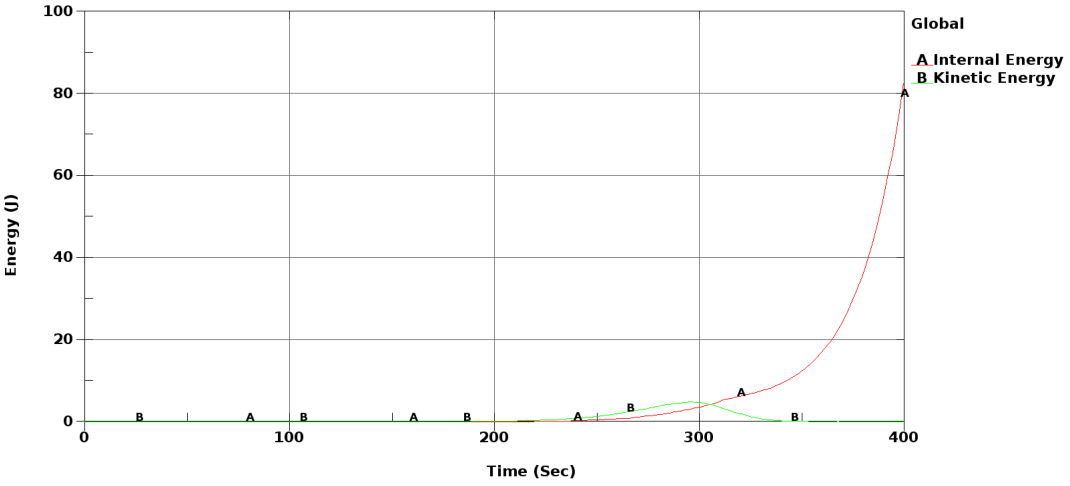

Figure 4.20: Internal and kinetic energy vs. time for the base model.

Earlier it was shown that the test models have a nonzero kinetic energy at the end of the simulation, but that effect is negligible because the magnitude of the kinetic energy is two orders of magnitude lower than that of the internal energy. Figure 4.20 shows that with the reduced maximum inflation pressure this is still true. The kinetic energy is near zero at the end of the simulation and the spike observed, near time 300 seconds, corresponds to a change in model geometry. The model is considered stable through the complete simulation.

The focus of this project is to model the inflation of a dunnage bag to investigate the stress pattern associated with an inflated bag. Two preliminary stress plots are shown in Fig. 4.21 and 4.22. These plots show the Von Mises and first principal stress in the final geometric configuration respectively. The stress pattern is that of a low pressure inflation with characteristic diagonal

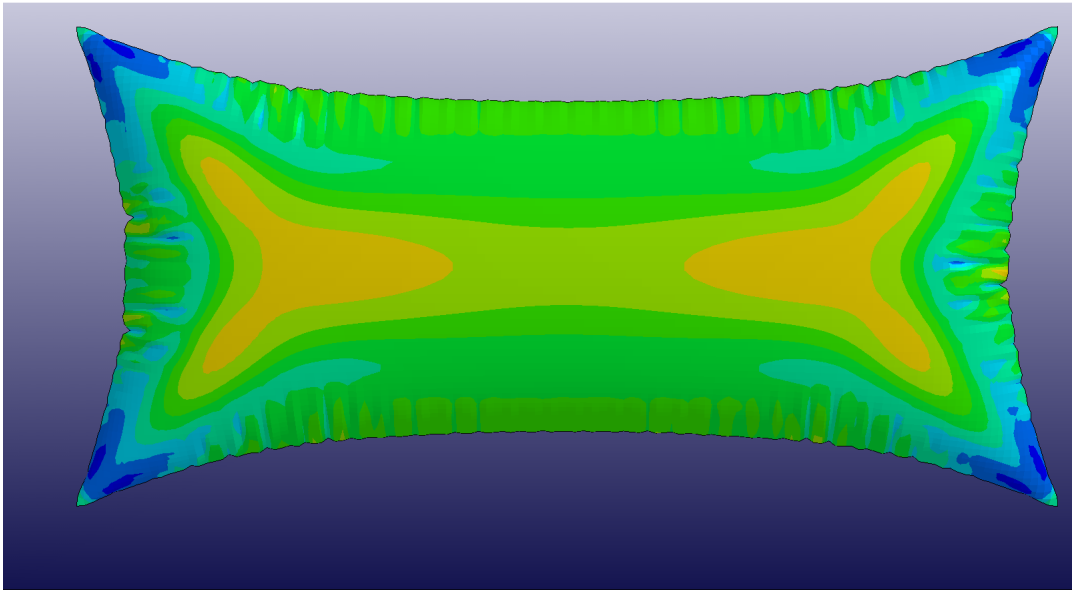

Figure 4.21: Von Mises stress for the inflated base model, where red is a high and blue is a low stress area.

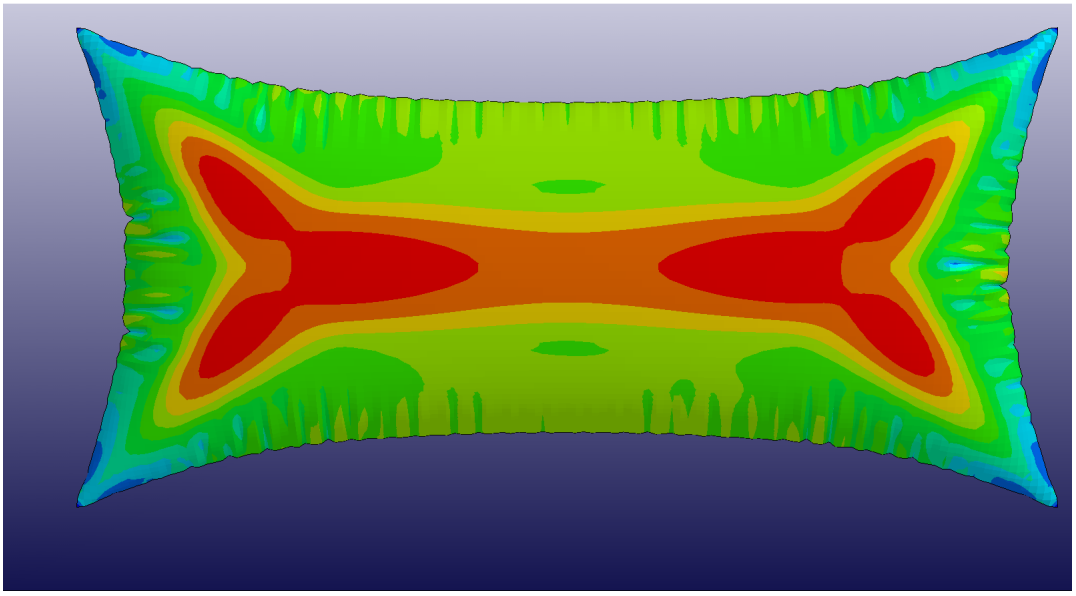

Figure 4.22: First principal stress for the inflated base model, where red is a high and blue is a low stress area.

high stress bands. The first principal stress is included here because it highlights the high tension areas in the model. Here the characteristic stress pattern described by the Von Mises stress plot is still evident but the importance of the hoop stress along the longer edge can also easily be seen.

Chapter 5

Building a Representative Numerical Model

Chapter 4 described the development of a generic inflation model. Visual comparison of the base model simulation and physical tests show close correlation between their overall shape. This chapter describes the subsequent adaptation of the base model to include finer model details, including the valve, seams and constrained inflation. The completion of this phase in model development produced a full inflation model of a representative dunnage bag.

5.1 Inflation Valve Development

Dunnage bags are inflated through a non-return valve positioned in one corner of the bag. In the simulation model the bag undergoes inflation by means of an internal pressure. The valve is included in the model because it stiffens the structure of the bag, and bags often fail in the area of the valve. Several different ways of including the valve were tested.

5.1.1 Representing the Valve as a Disc

It was first assumed that the valve could be represented by a stiffened disc within the paper mesh. A small circular mesh was included in the existing mesh. This required making a three-part mesh. The first mesh, covering the main body of the bag, is orthonormal and has a large mesh size. The second mesh, the area of the bag near the valve, changes the mesh from a coarse one along a square exterior line to a fine one along a circular interior line. The third mesh, covering the valve, is a small disc. Figure 5.1 shows the mesh near the disc.

The small circular center mesh has misshaped elements that caused problems in the simulation. Firstly, the non-square elements were overly stiff and produced local stress concentrations in an area where the analysis is required to produce accurate data. Secondly, these elements have a smaller volume

than those in the rest of the model. This is a problem as the time step size for the analysis is driven by the element with the smallest volume. A smaller element volume requires a smaller time step.

The paper bag and the plastic valve disc were assigned two separate section properties. At this point it was only important that the valve be much stiffer than the surrounding paper so the same elastic modulus was used for both but the section thickness for the disc was set at ten times that of the paper. Stiffening of the disc can be done in two ways, either by changing the material or section properties of the disc. The Young's modulus of the disc could be increased, but if the difference in moduli for the paper and disc gets too high the model becomes numerically unstable. Increasing the thickness of the disc elements makes them heavier than the surrounding shells and the difference in inertia for the adjacent parts makes the model unstable.

In the model a low stiffness for the valve disc causes the valve to wrinkle with the paper. If the stiffness of the valve is increased to the point where it resists this effect, the model becomes unusable due to the difference in stiffness between the adjacent paper and disc elements, Fig. 5.2. The model should be capable of testing the effect of changing the component materials. The material property for the disc was by then completely non-representative. It was thus concluded that a rigid disc assumption cannot be used for this simulation.

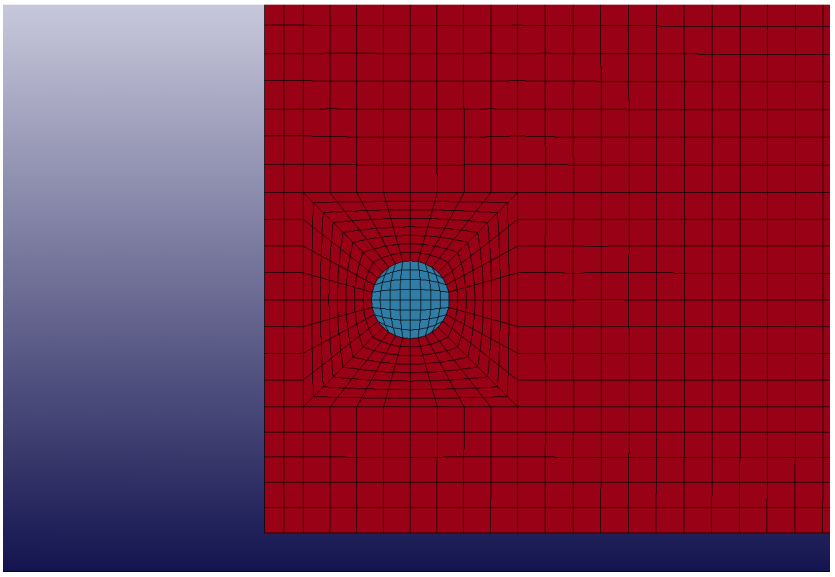

Figure 5.1: Enlarged view of the disc mesh representing the inflation valve. Valve shown in blue.

5.1.2 Valve Removed

Next the valve was excluded and analysis of the stress pattern around the hole was performed. The same mesh was used as for the disc representation with

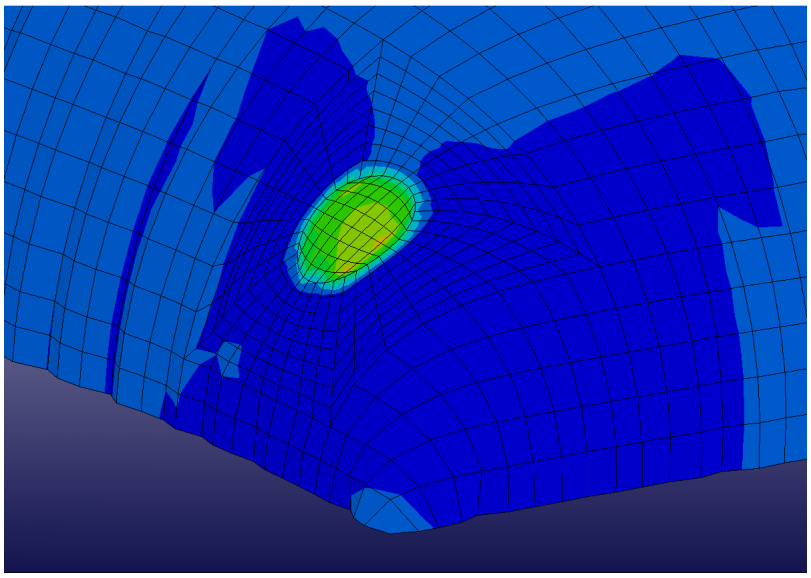

Figure 5.2: Von Mises stress near the disc valve representation, where red is a high and blue is a low stress area.

the disc elements removed, leaving a hole in the paper sheet. Figure 5.3 shows the mesh used. To compensate for the loss of pressure on the removed section, nodal equivalent forces were applied to the outer edge nodes of the hole. This solved the problems associated with the misshaped elements and incompatible stiffness.

In this case the bag inflation is stable. However, the hole now deforms along with the rest of the bag, which is not representative of the physical bag inflation, Fig. 5.4.

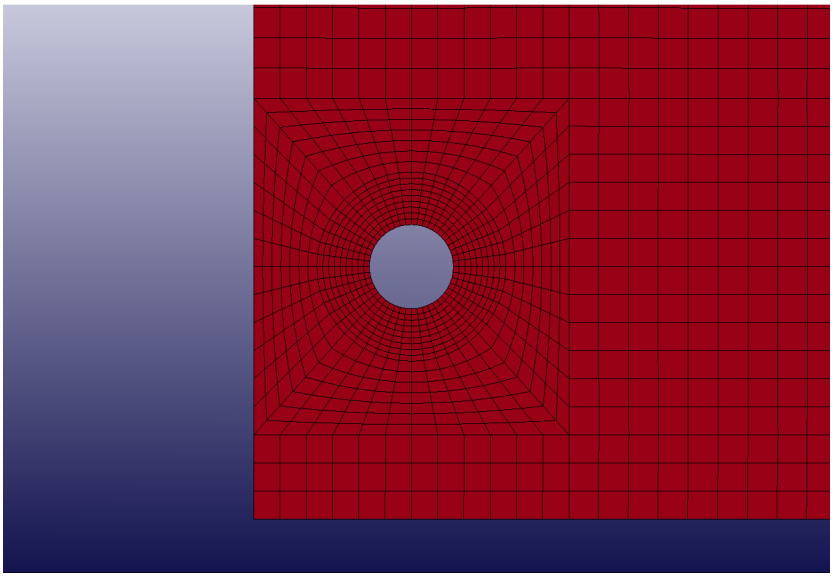

Figure 5.3: Enlarged view of the mesh representing the valve hole.

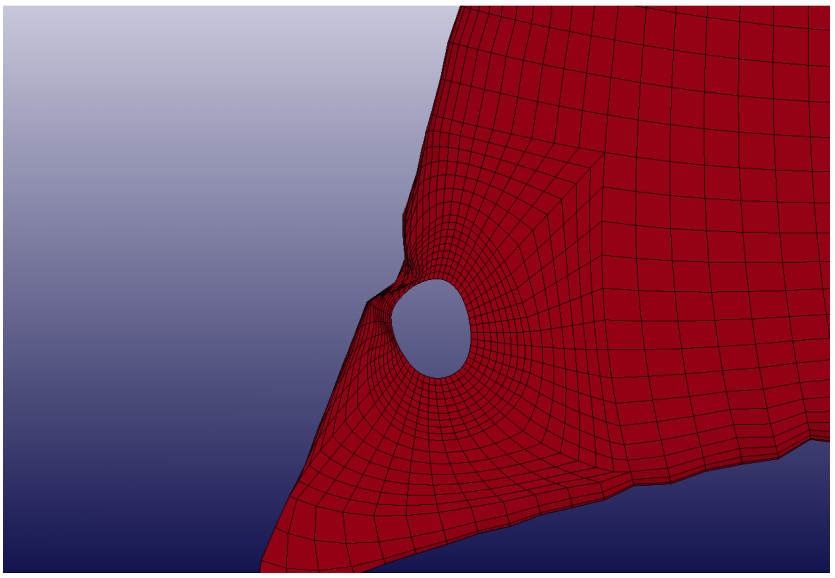

Figure 5.4: Enlarged view of the valve hole when inflated.

5.1.3 Representing the Valve as an Insert

It was decided that an independent valve should make contact with the inside of the bag. This insert should be free to slide and support the punched hole.

Single Sided Valve Insert

A short cylinder with an exterior flange was the first valve insert chosen, Fig. 5.5. Pressure is applied to the inside of the valve which is pressed against the paper bag, holding the shape of the hole. When inflation was simulated, the paper accelerated faster than the valve. Figure 5.6 shows how the valve insert then fell out of the hole and, when it makes contact with the bag, it is no longer aligned with the hole. The density of the valve was reduced to allow the insert to maintain contact with the paper, but the model became unstable. Several simulations were run, but a method of aligning the valve and hole was not found.

Double Sided Valve Insert

The single sided valve insert was improved by adding a second flange, Fig. 5.7. During simulation, the paper accelerates and makes contact with the valve, pulling the valve along with it. Towards the end of the simulation the paper acceleration slows. The pressure load applied to the inner flange of the insert presses the valve into the paper, resulting in the valve being well seated at the end of the simulation, Fig. 5.8. Figure 5.9 shows that this double sided valve insert is representative of the physical valve.

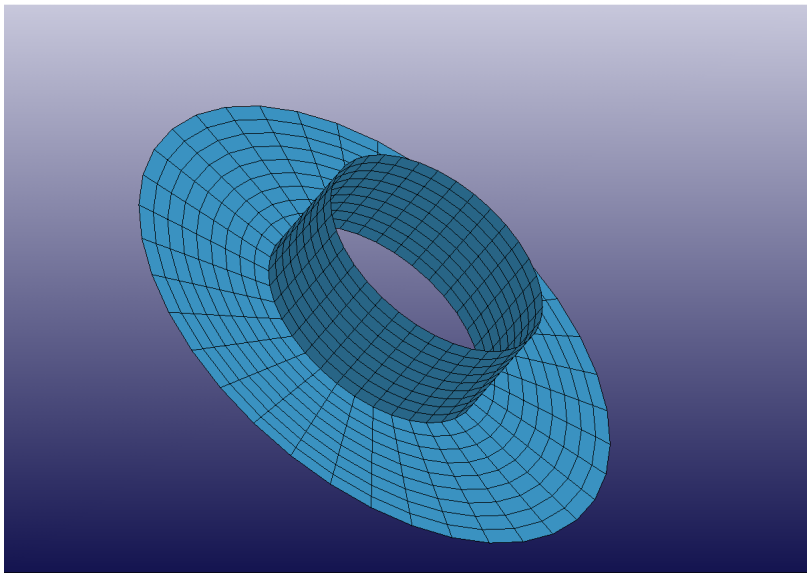

Figure 5.5: Mesh for the single sided valve insert.

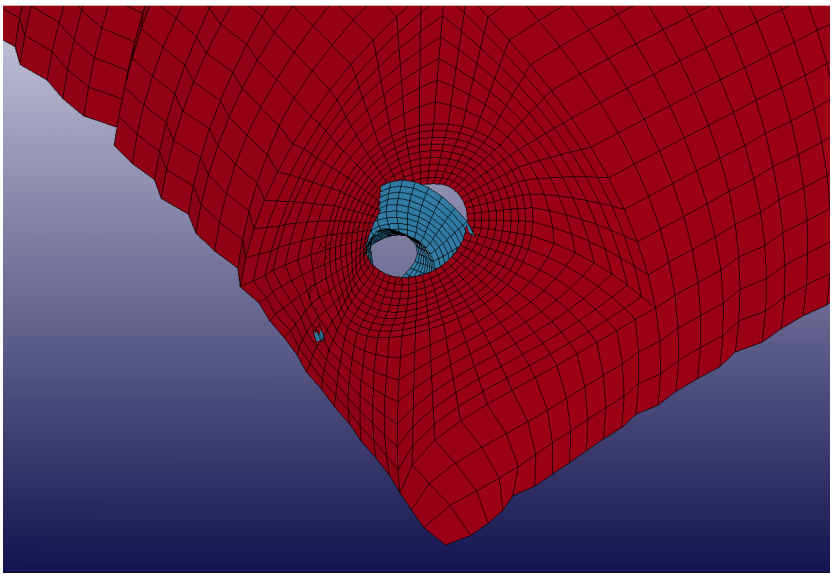

Figure 5.6: Misalignment of the single sided valve insert in the inflated bag. Valve insert shown in blue.

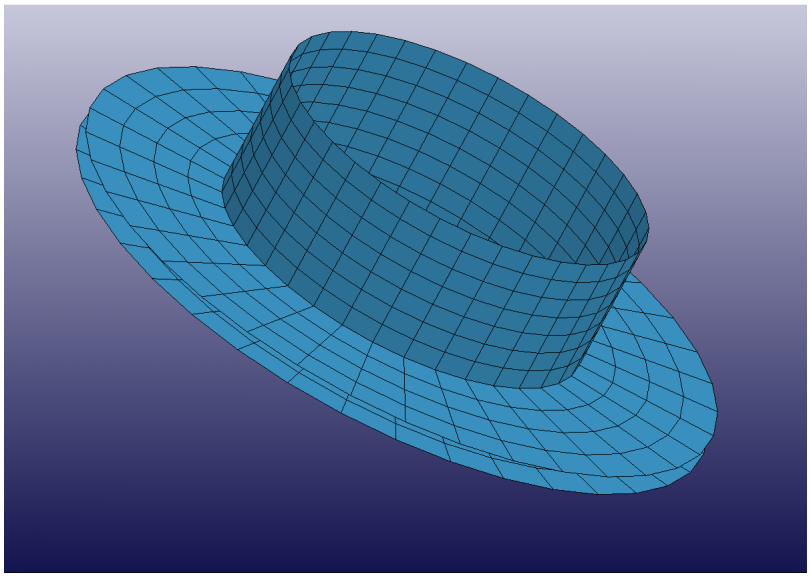

Figure 5.7: Mesh for the double sided valve insert.

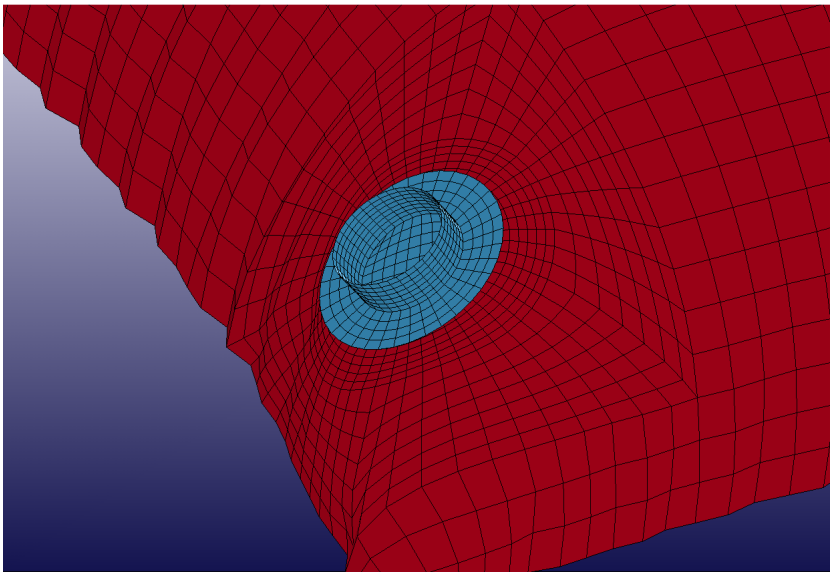

Figure 5.8: Seating of the double sided valve insert in the inflated bag. Valve insert shown in blue.

Figure 5.9: Physical double sided valve insert.

The contact model used is surface-to-surface, this allows contact between shells to be both normal to the plane and perpendicular to the edge of the element. The use of this contact model then precludes the addition of further constraints in this area.

5.2 Glued Seam Line Development

A prominent feature of the dunnage bag geometry is that it is a single paper sheet folded into a rectangular shape, held together by glued seams. These glued seams stiffen the local material properties of the bag. As the glued seams are near the areas of the bag which develop wrinkles and folds, they should be included for a meaningful simulation.

5.2.1 Representing Glued Seams Using Contact

The glued seams were included in the model by using tied node contact. Tied node contact takes two node sets and fixes their relative movement. A simulation was run where this contact method was used along an edge seam. The solver automatically detects which nodes are in contact and attaches them. Tied node contact also provides the option to specify a contact friction property for the contact. While the simulation ran successfully after the addition of a single seam, the addition of a second seam was not possible. Tied node contact is restricted to one contact per node set. Assigning the same nodes to two sets does not meet this requirement. When nodes are assigned to two sets, and both sets are used to define tied node contact, neither of the contact interfaces will be implemented. Therefore, tied node contact could not be used to model the glued seam lines.

5.2.2 Representing Glued Seams Using Section Properties

Taking into account the physical properties of the inflated bag and its failures, it was decided that only the overall properties of the glue lines need to be modeled. However, the seam has an effect on the bag and should be included in the full model. The bag seams were included using a separate geometry and material property for the seams and bag body. The existing mesh for the bag was used and the seams were included by assigning the seam elements to a different part, with a different section and material property. In the absence of material data for the glue paper combination, the seam was represented by a double thick paper section, Fig. 5.10.

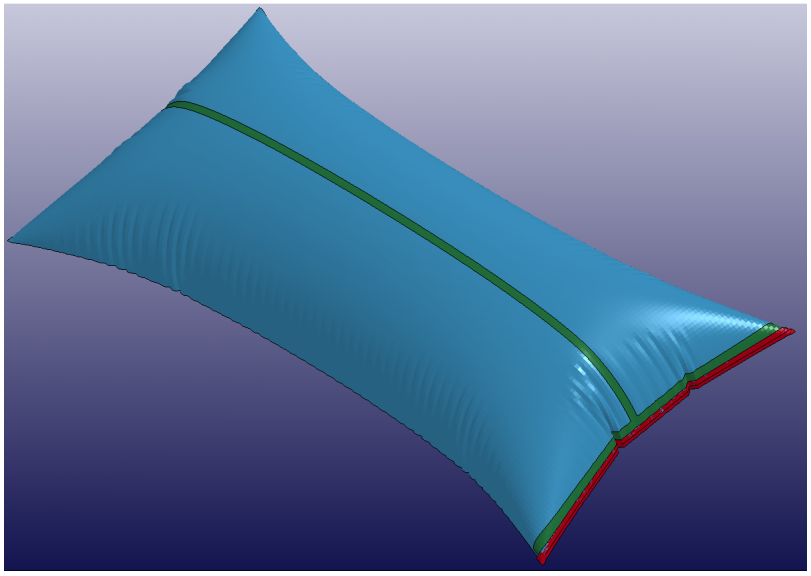

Figure 5.10: Glued seam lines using section properties. Glue lines shown in green.

5.3 Constrained Inflation

Next the contact between the inflating bag and the external plates of the test rig was included. An important parameter in the simulation of the inflation of a dunnage bag is the size of the void into which the bag is inflated. In the physical test procedure, a bag is placed on a lower plate and inflated until it makes contact with the upper plate The distance between these two plates is the desired gap size.

In the simulation, this was approximated by adding two rigid plates to the model, one above and one below the bag, each half the desired gap size away from the bag. When a simulation includes contact the solver checks for contact

after each iteration. If a node has passed through a surface specified in the contact algorithm the node is moved onto that surface by a contact force. This contact force is then monitored, and when the force required to retain a node in contact is in the direction of the surface the node is then released. The less time spent in contact, the less force data is recorded and the shorter the simulation time. Furthermore, this model has been heavily mass scaled and should the bag be positioned significantly closer to one plate than the other the inflated bag may not be symmetric, Fig. 5.11.

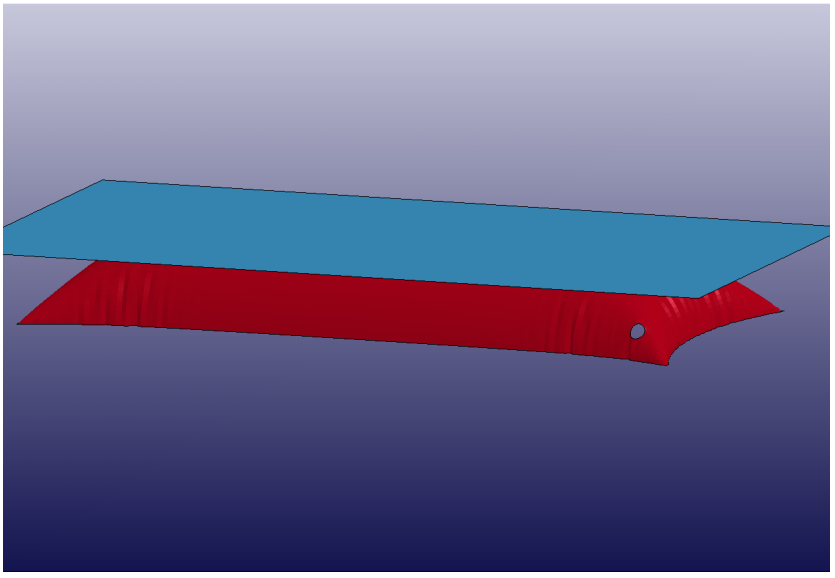

Figure 5.11: Symmetry model showing contact between the paper bag, red, and the external plate, blue.

5.4 Material Model Update

To this point in the development of the representative model, a material model without plasticity was used to reduce runtimes. The material model was adapted to more closely represent the kraft paper used for the physical bags. The material model chosen is an elastic-plastic isotropic material with kinematic hardening. Using the data acquired from the paper suppliers, as discussed in Chapter 3, two elastic moduli were found.

The first modulus is for the elastic region, 3 GPa, and the second is in the plastic region, 1.5 GPa. These values are consistent with literature [Baum *et al.* (1981*a*)]. Figure 5.12 shows the plastic deformation of the simulated bag while Fig. 5.13 shows a fully inflated dunnage bag. The wrinkle-free areas of the physical bag are the areas where plastic strain has occurred.

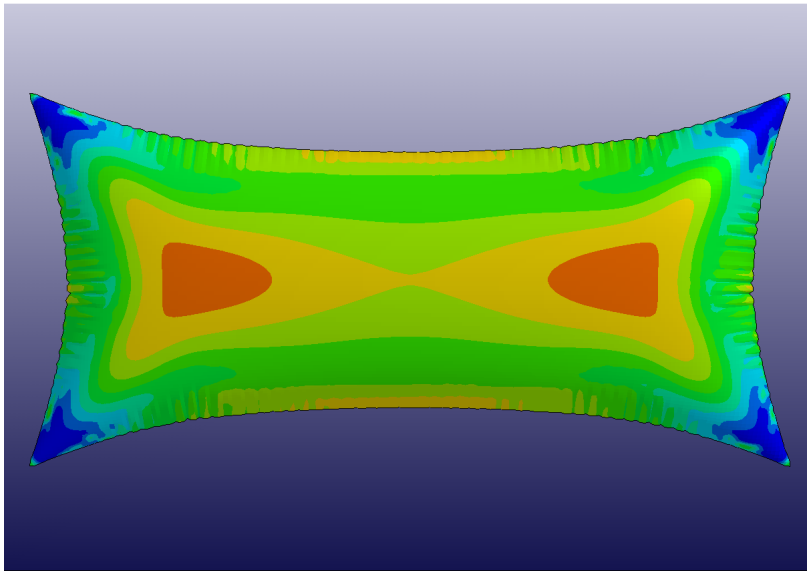

Figure 5.12: Plastic strain of a representative inflated bag, where red is a high and blue is a low strain area.

Figure 5.13: An Inflated sample bag showing plastic strain as wrinkle- and fold-free zones.

5.5 Representative Numerical Model

The base model developed in Chapter 4 has been adapted to more fully represent a paper dunnage bag through the inclusion of the correct geometry, inflation valve, seams, external constraints and material model. The complete model is stable and has specifications listed in Table 5.1. Simulated inflation of the model shows that it is representative of a paper dunnage bag, Fig. 5.14.

Table 5.1: Representative model specifications.

Model Type	Full Model
Dimensions	1.8×0.9 m
Material Model	Elastic-Plastic Isotropic, Kinematic Hardening
Young's Modulus, Elastic Region	3×10^9 Pa
Young's Modulus, Plastic Region	1.5×10^9 Pa
Poisson's Ratio	0.267
Material Density	1×10^{10} $\frac{\text{Kg}}{\text{m}^3}$
Shell Thickness, Bag	1.2×10^{-4} m
Shell Thickness, Seam	2.4×10^{-4} m
Maximum Pressure	20×10^3 Pa
Damping Constant	0.25
Analysis Time	400 sec
Load	Exponential Pressure
Time Scale Factor	0.5
Valve Type	Double Sided Insert
Constraint Type	External Contact
Seam Type	Section Property Based

5.6 Edge Fold Stress Investigation

Upon simulation of the completed representative model, an unexpected stress was found along the folded edge of the inflated bag, Fig. 5.15. It was not known whether this stress is present in the physical model or whether it is a spurious stress due to the nodal equivalencing of the top and bottom sheets of the bag at an acute angle. When the bag inflates this acute angle is opened to a straight line causing bending stress. To test the presence of this stress, the bending stress was removed from this area of the model.

5.6.1 Membranes Elements Along the Fold Edge

Removing the bending stress along the folded edge was done by replacing a row of shell elements along the edge adjacent to the fold with membrane ele-

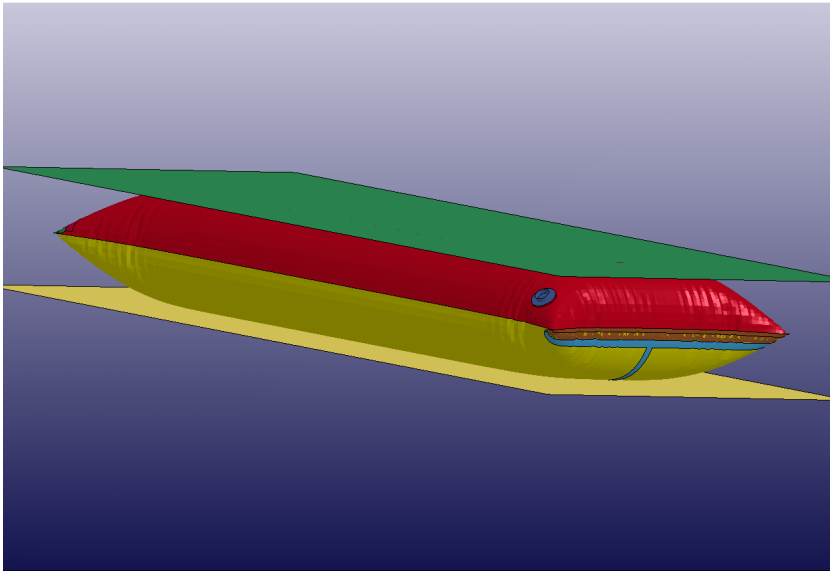

Figure 5.14: Inflation of the representative model. Bag body, red and dark yellow, seams and valve, blue, external constraints, green and light yellow.

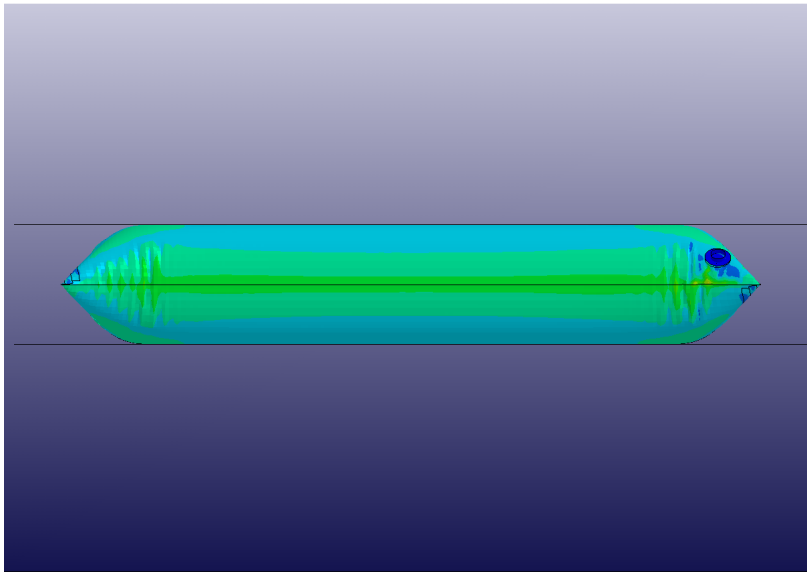

Figure 5.15: Side view of the Von Mises stress for the inflated representative model, where red is a high and blue is a low stress area.

ments, as membrane elements do not have bending stiffness. Using membrane elements in this area reduces model stability and increases the runtime for the simulation. Figure 5.16 shows the variation in stress seen in the final state of the simulation, the high stress areas are shown in red. The membrane model is unstable and the stress pattern produced is erratic, caused by spurious nodal velocities in the out-of-plane direction. These nodal velocities may be caused by the inconsistency caused by shell elements, that can hold a bending moment, being connected to membrane elements, that can not. A model produced with only membrane elements was not stable enough to be used in this test.

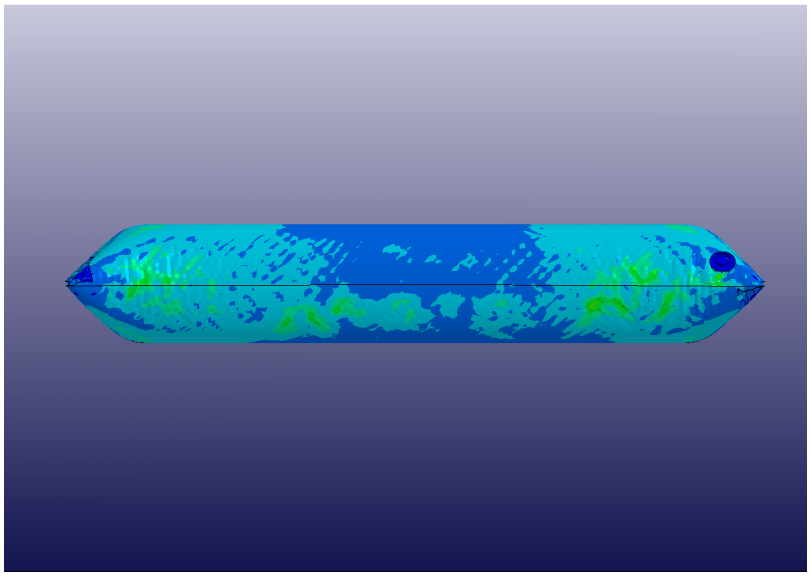

Figure 5.16: Side view of the Von Mises stress for the inflated membrane model, where red areas denote a high stress and blue areas denote a low stress.

5.6.2 Morphed Cylinder Model

A cylindrical mesh was morphed into a pillow shape to reduce the initial angle between the top and bottom sheets, but in the areas near the end of the bag there was still a very small angle between these sheets. Figure 5.17 shows the stress pattern of the morphed pillow model.

Physical testing and information gained from field use of paper dunnage bags shows that the bags do fail along these folds. The original acute angled configuration will be used in later models. Ideally a separate material property would be used to model the material near the fold, as it no longer has the same material properties as the main paper sheet. The process of folding paper is known to be modeled using a fully anisotropic material model, which is too complex for this application.

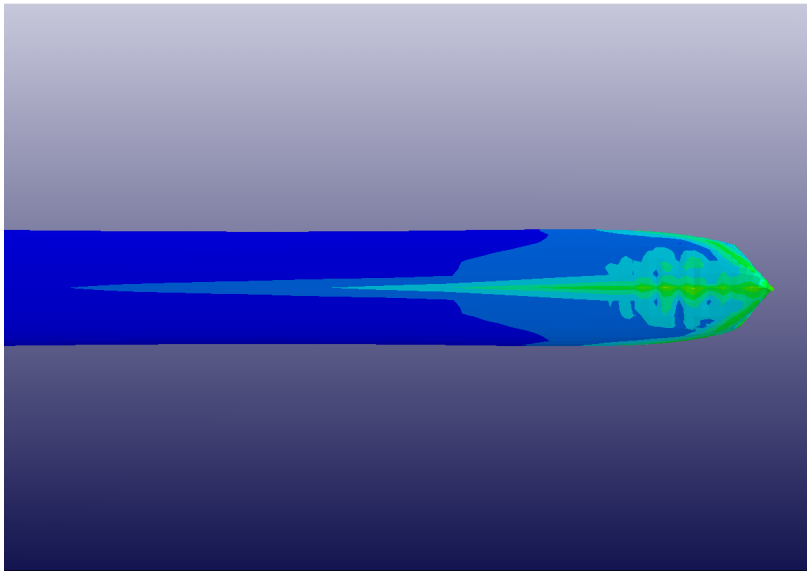

Figure 5.17: Side view of the Von Mises stress for the inflated morphed cylinder model, where red is a high and blue is a low stress.

Chapter 6

Generation of Physical Data for Model Validation

The primary validation for this project is the comparison of the simulation model to physical test data. The inflation of a dunnage bag to a given pressure and into a given void is tested. To simplify the experiments and simulation, the void used for these tests is the space between two flat parallel plates with a fixed gap.

In the absence of surface strain data the verification will be done using contact force and shape comparisons. Measuring actual surface strain values is complicated by the large deformation of the bag at low strain and the type of material chosen for the bags. Further complications are due to the thickness of the material and wrinkling of the bag. The material is too thin to bond a standard gage to without significantly stiffening the surrounding area. That and the wrinkle pattern being unknown before the test starts has a significant influence on the local stress values.

Important parameters for these tests are the dimensions of the bag, the size of the gap between the two parallel plates that the bag is inflated into, the relative pressure inside the bag and the force applied to the bag by the test rig.

Physical data generated was used to validate the effects of volume change through bag and gap size in the model. Two different plies were tested to see if the simulation requires separate layers for each ply or if a cumulative material thickness would be a valid assumption.

A range of sample bag sizes were used for these tests to investigate how well the simulated model represents different physical models. Bags were chosen for both their size and shape. Two rectangular bags and two lower-volume square bags were used. The samples were also chosen to represent bags near the production size limits for dunnage bags. The sample bag dimensions and plies chosen are shown in Table 6.1.

While the number of plies can be as high as six or eight, only one and two ply bags were used to investigate the effect of material thickness, in order to reduce the pressure required to burst the bags.

Table 6.1: Dunnage bag sample information

Deflated Dimensions (mm)	No. Plies
2200 × 900	1
2200 × 900	2
900 × 900	1
900 × 900	2
2200 × 1200	1
2200 × 1200	2
1200 × 1200	1
1200 × 1200	2

6.1 Experimental Setup

The test rig, Fig. 6.1, used for these experiments was custom built for testing dunnage bags. The test rig consists of two flat rigid steel plates. The lower plate is fixed to the laboratory floor while the upper plate is connected to a hydraulic actuator. The hydraulic actuator lifts the upper plate, allowing the gap between the plates to be fixed at various sizes. A pneumatic supply line provides for the inflation of the bags. Both hydraulic and pneumatic lines are controlled by a hand-held pendant controller.

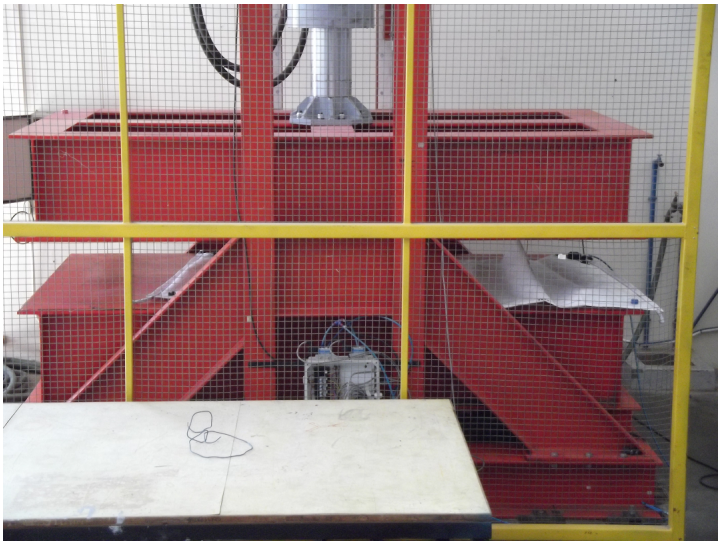

Figure 6.1: Side view of the dunnage bag test rig.

The hydraulic actuator has a three-way control valve that allows for; move up, move down and hold functions. Hydraulic supply can be switched off while the actuator is in the hold state without the gap size changing. The rig is also set up for proportional and integration control of displacement. Similarly two

two-way pneumatic control valves are used to allow for; inflate, deflate and hold functions.

The test rig is also fitted with three data measurement devices, namely a linear variable displacement transducer to measure the gap size, a pressure transducer to measure the relative pressure inside the bag and a series of bridged load cells to measure the contact force applied by the test rig on the sample bag.

6.2 Experimental Procedure

Each bag is placed between the flat parallel plates of the test rig, flat onto the bottom plate, and the inflation line is connected. The pressure measurement line is run inside the air supply line so that the existing valve can be used as the orifice to measure internal pressure. The alternative would be inserting another gland for measurement purposes which would change the inflated shape of the bag.

A gap size is set and held, then the bag is inflated until it bursts. While the bag inflates photos and video clips are taken for later comparison. Once the test is completed the bag is removed from the test rig and logged for later inspection.

Twelve test sets of either five or ten bags were completed. The 2200 × 900 mm and 900 × 900 mm bags were used as the primary test samples while the other bags produced supplemental information. Three different void sizes were tested, two constrained voids with gap sizes of 150 mm and 300 mm, and one unconstrained void. A summary of the tests is shown in Table 6.2.

Table 6.2: List of test sets with testing parameters.

Test Set Number	Bag Size (mm)	Ply	Gap Size (mm)	Number of Bags
1	2200 × 900	1	unconstrained	10
2	2200 × 900	1	300	10
3	2200 × 900	1	150	10
4	900 × 900	1	unconstrained	10
5	900 × 900	1	300	10
6	900 × 900	1	150	10
7	2200 × 1200	1	150	5
8	900 × 900	2	150	5
9	2200 × 900	2	150	5
10	1200 × 1200	1	150	5
11	1200 × 1200	2	150	5
12	2200 × 1200	2	150	5

Gap size, pressure and contact force were recorded using a data acquisition unit. Photos were taken from three different angles and a further two photos were taken of the valve area once the bag was inflated, Figs. 6.2 through 6.5.

Figure 6.2: Front view of an inflated bag in the test setup.

Figure 6.3: Side view of an inflated bag in the test setup.

Due to the flexibility and low mass of the paper bags, the internal pressure required to inflate the bag is low for the majority of the inflation time. The pressure transducer available was not sensitive enough to pick up any pressure change during the bulk of the displacement. The displacement behaviour relative to internal pressure would not provide useful data in this test. However, an investigation of the relationship between the volume pumped into the bag,

Figure 6.4: Corner view of an inflated bag in the test setup.

Figure 6.5: Enlarged view of the valve of an inflated bag in the test setup.

internal pressure and displacement could provide useful data, tough no such flow sensor was available at the time of these tests.

6.3 Results

In addition to the numerical data gathered using the test rig's built-in sensors, observations were made during each test and bags were inspected after each test.

Information was also gathered from the data acquisition unit recordings. This data was reduced using the ratio of the contact force (F) over internal pressure (P).

If

$$\frac{\frac{F_i}{P_i}}{\frac{F_{i-1}}{P_{i-1}} + \frac{F_i}{P_i} + \frac{F_{i+1}}{P_{i+1}}} > 0.01 \tag{6.3.1}$$

, for data points recorded at time i, then those points are excluded from the data set.

The remaining data points were used to extract information on maximum pressure, maximum contact force and maximum and median contact area. The contact area was generated using the internal air pressure and the measured contact force.

Finally, each failed bag was inspected. The position of the failure and whether the valve was involved or not, was noted for each bag. The failures were separated by where they occurred, not necessarily where the failure started. Six distinct failure zones were defined, Fig. 6.6. Zones one to four are edge zones and consist of both sides of the fold. Zones five and six are the mid-sheet zones, one on each side. The valve is situated between zones one and two. For each bag the zones that failed were recorded.

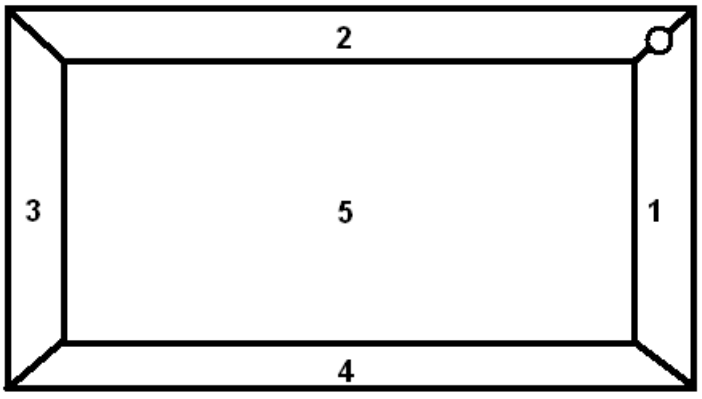

Figure 6.6: Definition of sample bag failure zones. The valve is positioned between zones one and two. Zone six is not shown.

6.4 Discussion of Results

During the inflation of the bags two things were noticed that require further investigation. Firstly, the inner flange of the inflation valve presses into the paper of the bag causing a severe stress concentration that would be challenging to model. Secondly, the bags have a tendency to be thrown towards the point of failure. The expectation is that the bag would be thrown away from the point of failure, thrust by the air escaping from the burst point. Some bags were found to form a 'fishtail' shape due to the escaping air volume, Fig. 6.7.

Figure 6.7: Post burst sample showing 'fishtailing'.

The data collected was used to plot characteristics for each test and test set. Pressure and contact force over time were plotted for each test in a set. Bar charts were generated showing burst pressure, burst force and the median contact area for each test. For the cases involving the unconstrained voids, contact force and contact area were excluded.

The graphic plots of the pressure and contact force over time were used to check the consistency of each test set's data. The data has been shifted to start at the same time. This data shows the internal pressure and contact force are consistent over the part of inflation where the most pressure is applied, the final few seconds of the inflation. A representative set is shown in Fig. 6.8 and 6.9.

The bar plots of the pressure and contact force at burst as well as the median contact area further corroborate the consistency of the data, as shown in representative figures, Fig. 6.10 through 6.12. Burst pressures differ by no more than 10% in each test set.

Once the data within each test set was checked, the average burst pressure and contact force for each test set were plotted on a graph with the median contact area for each test set, Fig. 6.13. The four tallest burst pressure bars

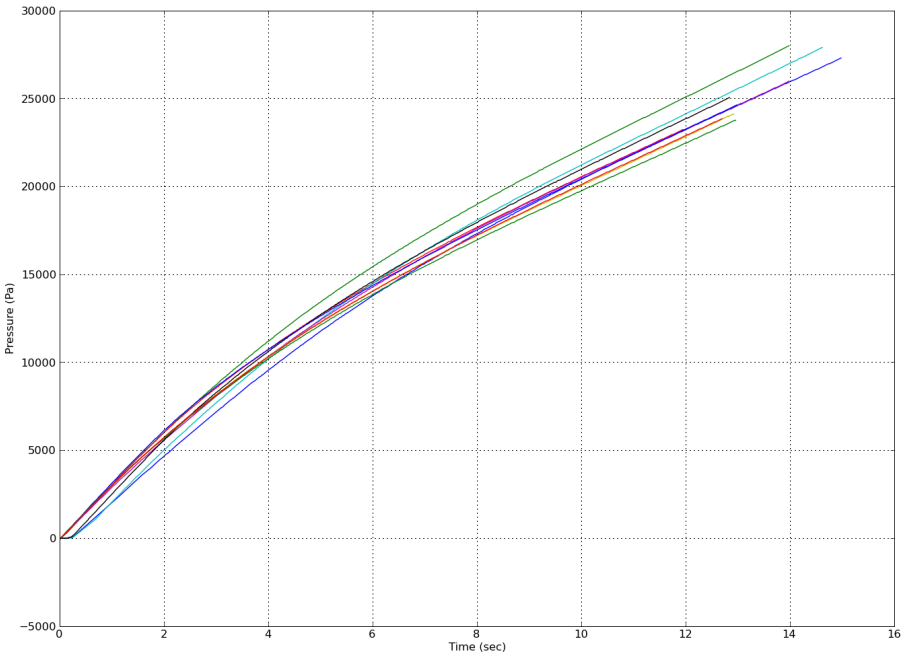

Figure 6.8: Pressure vs. time for test set four.

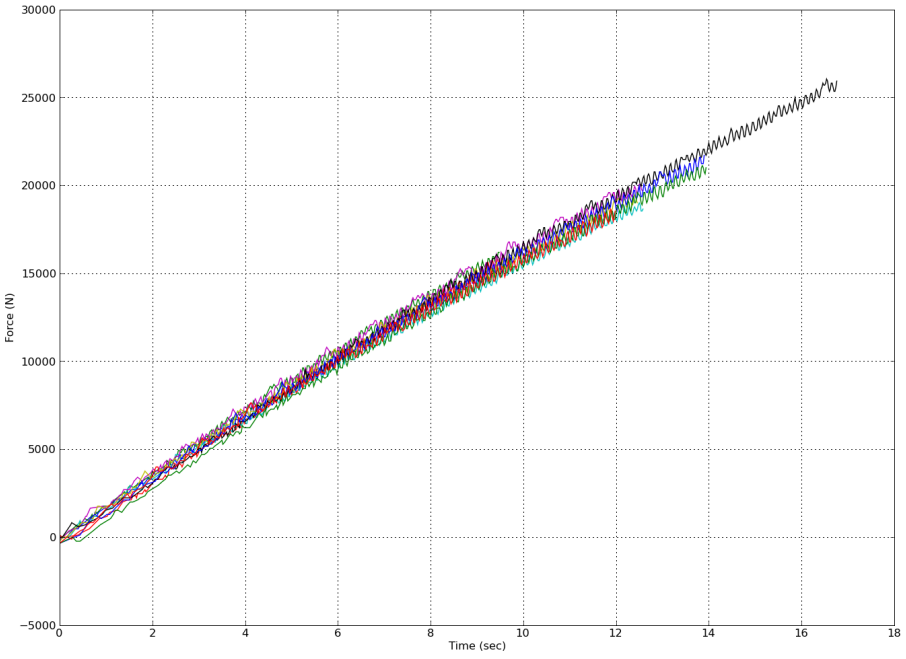

Figure 6.9: Contact force vs. time for test set six.

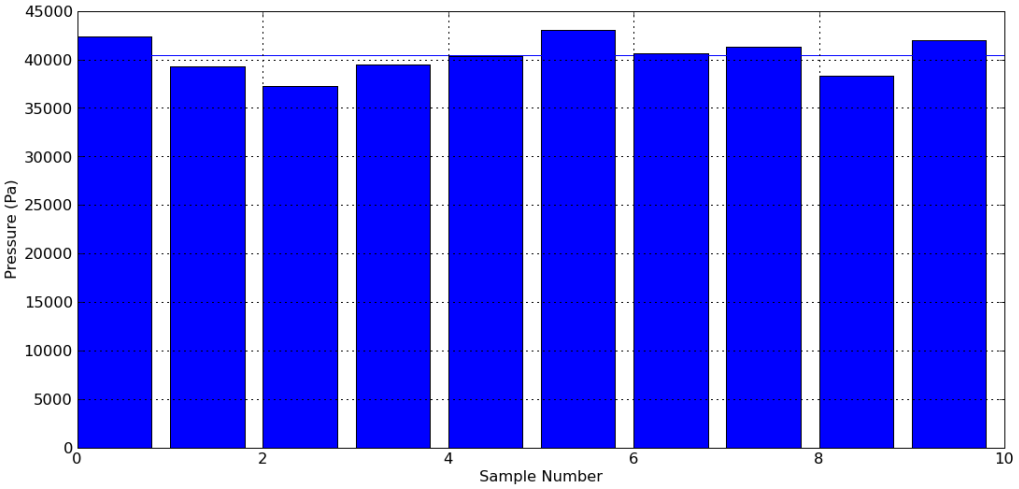

Figure 6.10: Burst pressure recorded for each sample in test set five.

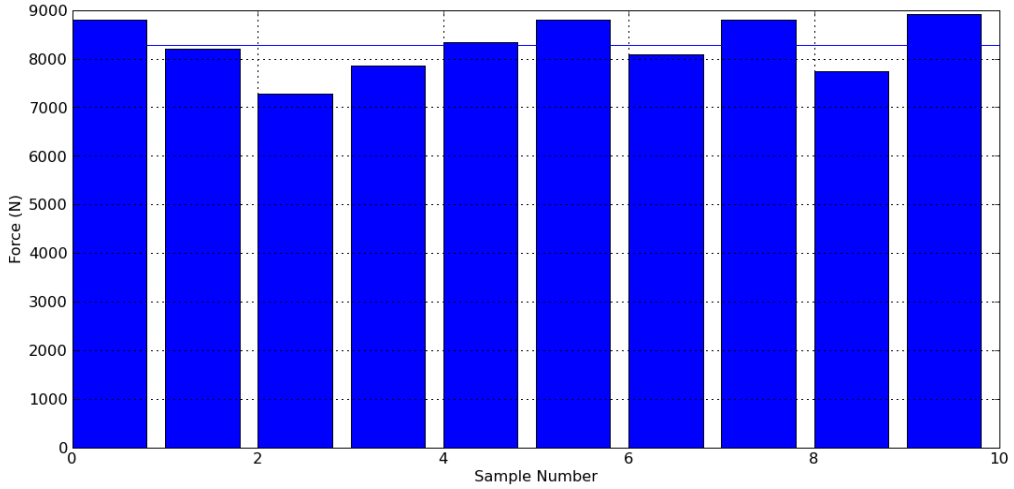

Figure 6.11: Contact force recorded for each sample in test set five.

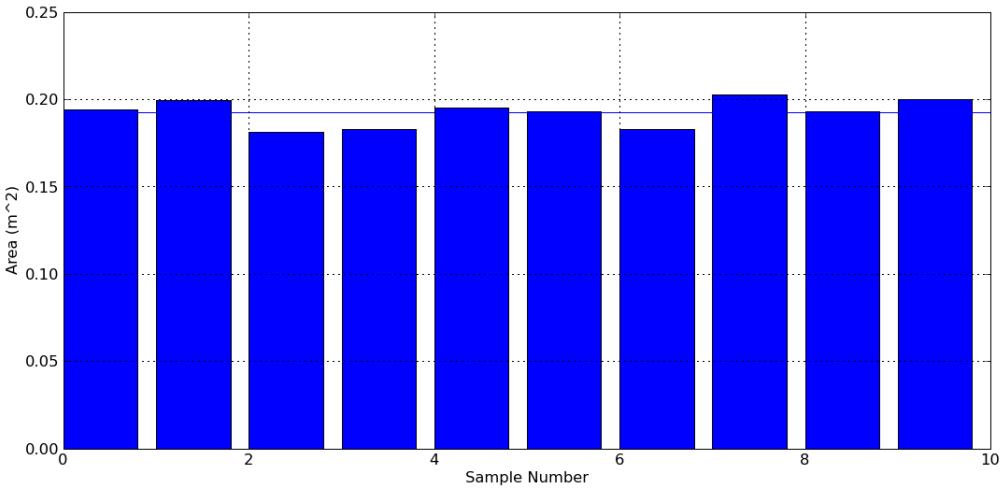

Figure 6.12: Median contact area recorded for each sample in test set five.

were 2 ply bags. Each bar also indicates the standard deviation associated with that test set. Four average lines are plotted on the graph. The top line is the average for the 2 ply bags, the next line down is the average for the 1 ply bags at a 150 mm gap, the third is the average for the 1 ply bags at 300 mm and the lowest line is the average for the unconstrained 1 ply bags.

It is seen that the ply number is related to the burst pressure of the paper bags. The more plies a bag has, the higher the burst pressure. However, doubling ply number does not double the expected burst pressure.

Burst pressure can also be increased by reducing the void size. In the case of the 2200×900 mm bags, the burst pressure when filling a 150 mm gap is twice that of a bag that is unconstrained. Unexpectedly, the volume of air contained within a bag appears to bear no relationship to the achievable burst pressures. All four bag sizes have similar average burst pressures at a 150 mm gap, even though they represent different contained volumes.

Failure data from post burst bag inspections was then analysed. The position of failure for each bag was classified by the zones affected by the failure, Figure 6.6. The combination of the failure zones were also recorded. That is, if zones one and two failed on a particular bag, it had a failure combination '12'. There were only 12 failure zone combinations, shown in Table 6.3. Figure 6.14 shows first the number of failures in each failure zone, then the number of failure zone combinations. The graph shows that the edges nearest the valve fail most often, and the combination of these two edges failing is the most common failure combination. This suggests that the valve itself is involved in the failure.

Figure 6.15 shows the burst pressures and failure zone combinations for each test set. Different failure combinations are more prevalent for different voids. Unconstrained bags are likely to fail in zones five and six, which is

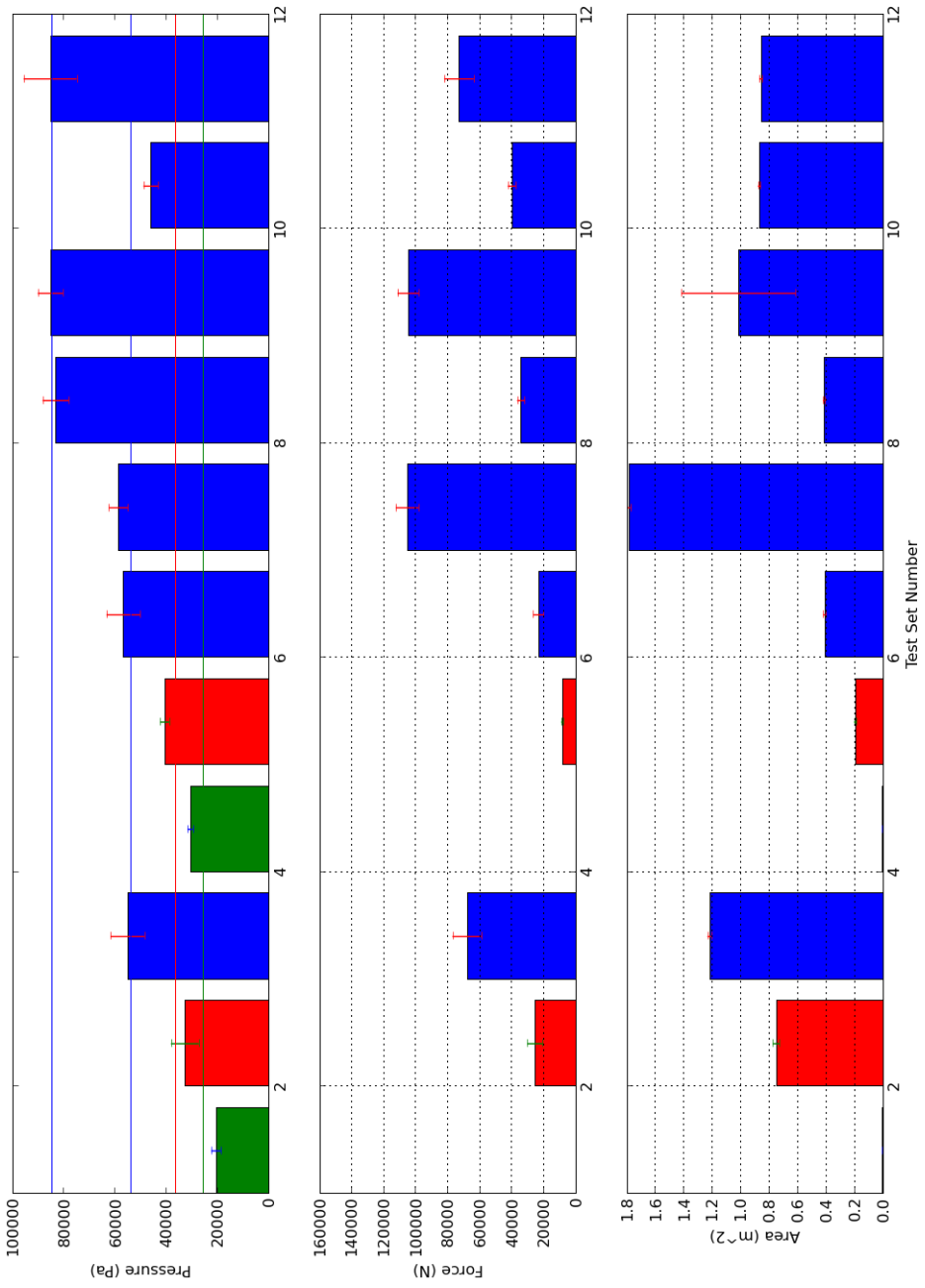

Figure 6.13: Overview of average test set burst pressure, contact force and contact area for each test set. Green, red and blue columns are for tests done in unconstrained, 300 mm and 150 mm voids respectively.

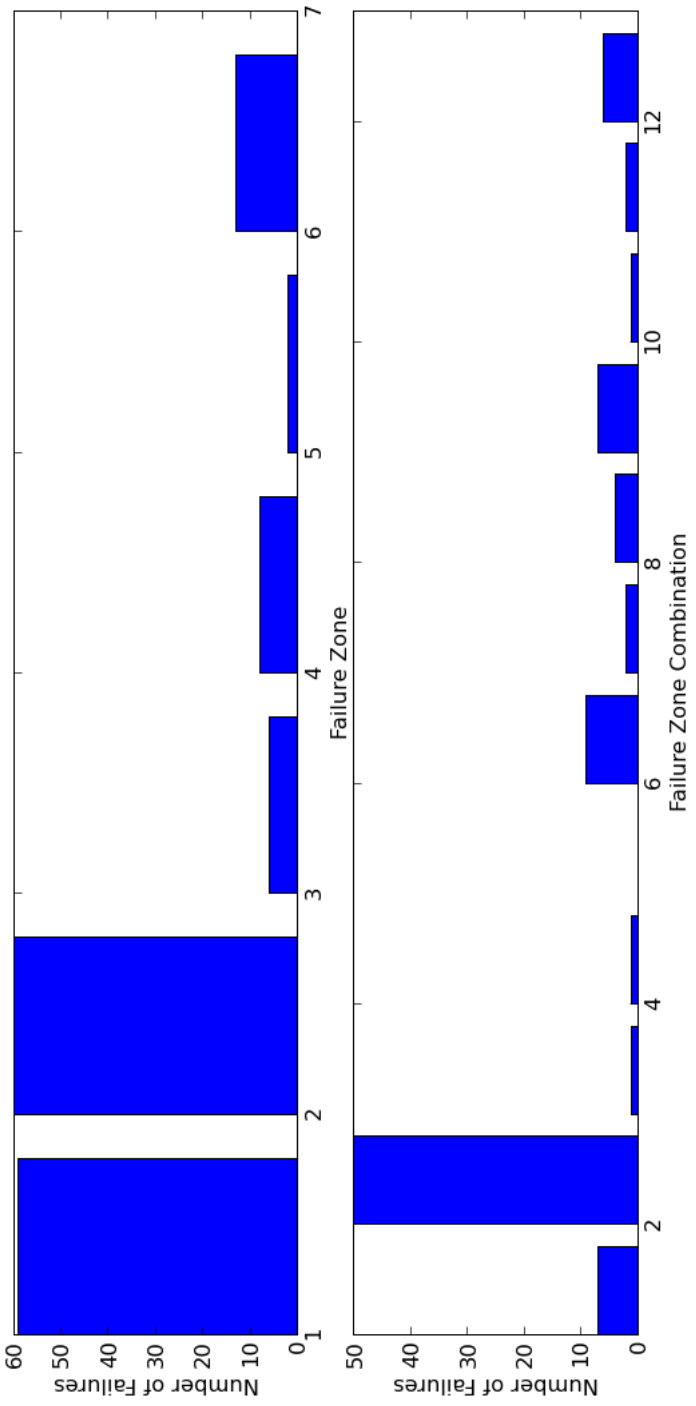

Figure 6.14: Failure data overview by zone and zone combination.

Table 6.3: Failure zone combinations with their corresponding colour

Failure Zone Combination	Failure Zones	Failure Zone Colour
1	1	Blue
2	12	Magenta
3	16	White
4	126	Orange
5	125	Pink
6	2	Red
7	3	Green
8	36	Aqua
9	4	Cyan
10	46	Grey
11	5	Yellow
12	6	Black

unseen in constrained tests. Furthermore tests performed at a 150mm gap tended to fail primarily in zones one and two.

Figure 6.16 shows the burst pressure of each test. The tests have been sorted by burst pressure, with the lowest burst pressure on the left and the highest on the right. It can be seen that the higher pressure tests fail mostly in failure combinations two, one and six.

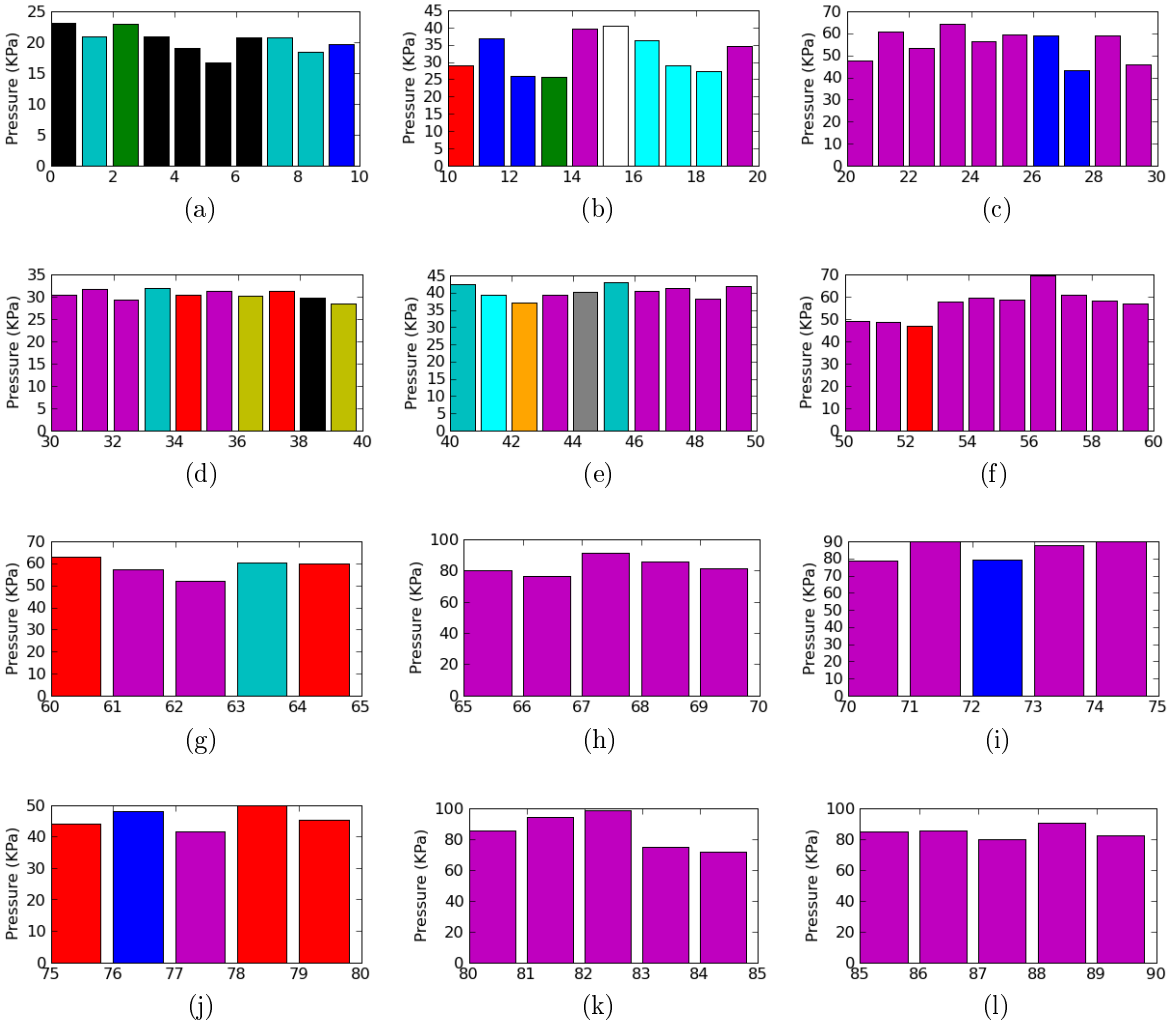

Figure 6.15: Failure data overview by set. Each subplot shows the burst pressure (KPa) recorded for each sample in a set. The bar colors correspond to the failure combination as per Table 6.3. (a) Test Set 1. (b) Test Set 2. (c) Test Set 3. (d) Test Set 4. (e) Test Set 5. (f) Test Set 6. (g) Test Set 7. (h) Test Set 8. (i) Test Set 9. (j) Test Set 10. (k) Test Set 11. (l) Test Set 12.

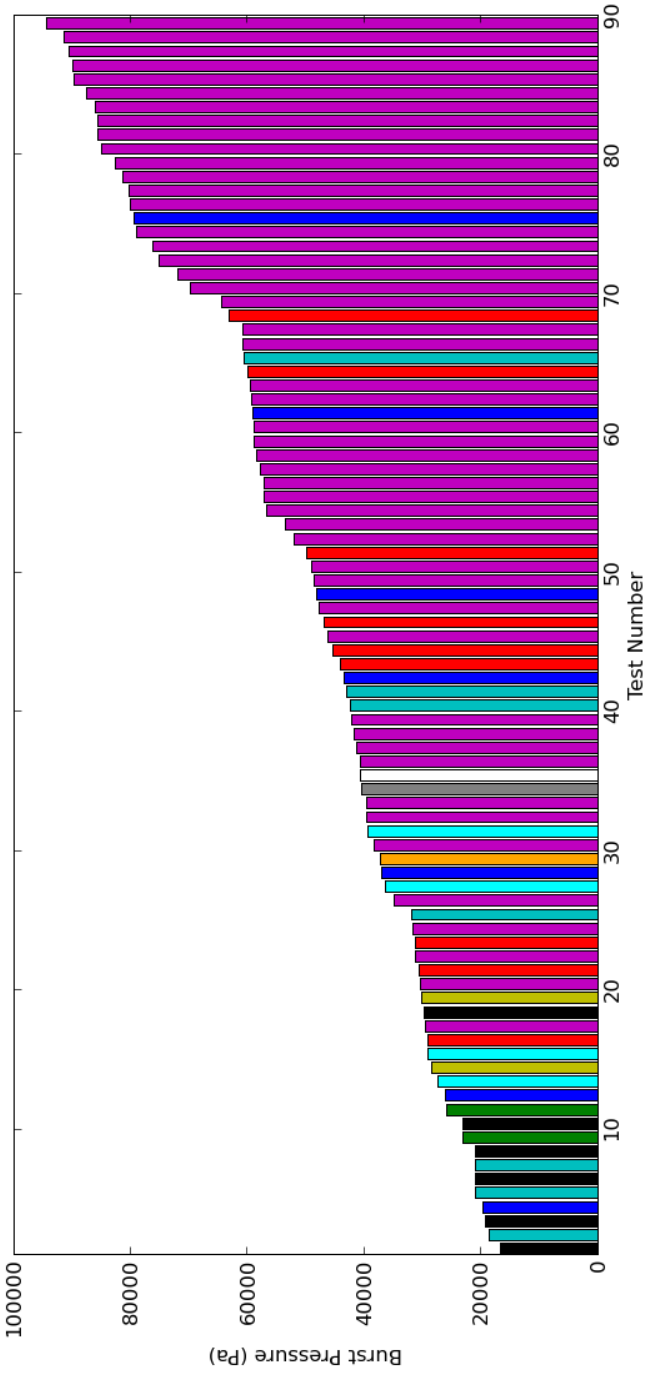

Figure 6.16: Burst pressure and failure zone combination for each test. Color coding as per Table 6.3.

Chapter 7

Validation of the Numerical Model

The simulated model of a paper dunnage bag is to provide a tool with which to investigate new designs. To this end, the model should represent the physical testing of the bags to an acceptable degree. This chapter describes how the simulated models compare with physical tests.

A numerical model was created to resemble each physical test set. The representative model discussed in Chapter 5 was used as a base for these validation models. The geometry of each sample bag was recreated and the average burst pressure for that test set was used as the maximum applied pressure in the simulation.

7.1 Basis for Model Validation

The simulated model was compared both to the physical tests conducted and to literature. First the deformed shape of the simulated bag was compared visually to photographs taken during testing. It is important that the inflated shape produced by the simulation is comparable to that of the sample bags. These simulations are run with a simple contact interface, but the model is required to have the capability to conform to more complex contacting surfaces.

Secondly, the data retrieved from the data acquisition unit recordings was compared to the data generated by the simulation. The maximum internal pressure of the simulation was defined by the user and data pertaining to the contact force was then used for comparison. If the pressure within the simulated and physical bags are the same then the contact force should be the same. This can be used to define how well the simulated model matches the physical samples.

Finally the stress patterns discussed in literature were compared to those observed in the simulated models.

7.2 Visual Comparison

A visual comparison was made between the physical and simulated models for the three different gap sizes. The basic test requirements are met in the simulated models, Fig. 7.1, 7.3 and 7.5, as the bag is inflated between two flat parallel plates, similar for that in the physical models, Fig. 7.2, 7.4 and 7.6. Comparisons were then made between the physical and simulated models, on the overall shape of the inflated bags as well as the wrinkle and fold patterns observed along the edges of the inflated bag. Wrinkles are shallow repeated features visible on the edge of the inflated bags, and are more prominent near the bag corners. Folds form where the paper of the bag overlaps itself. These are distributed along the length of the inflated bag, but are more prominent when away from the corners.

For the unconstrained bag, the general shape of simulated inflated bag approximates the physical bag well. Near the midpoint of each edge, the cross section of the bag approaches a circle with the largest displacement of the bag being at the midpoint of the deflated rectangle. Wrinkling is visible along the entire length of the bag, but is deeper near the corner. Both the physical and simulated bags have three folds along an edge.

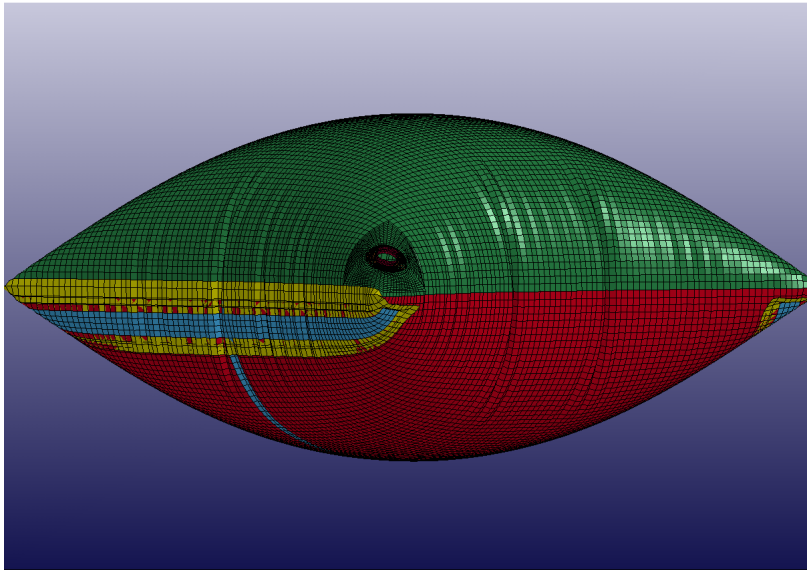

Figure 7.1: Inflated validation model, unconstrained.

Figure 7.2: Inflated sample bag, unconstrained.

The overall shape of the bags constrained at 300 mm also compare well. The wrinkle pattern of the bag is less prominent near the middle.

When the gap is reduced to 150 mm, wrinkles are only visible near the corner of the bag. There are no longer any folds, but there are some deep wrinkles that would become folds in a larger void.

7.3 Numerical Comparison

The numerical models were simulated at the average burst pressure of their

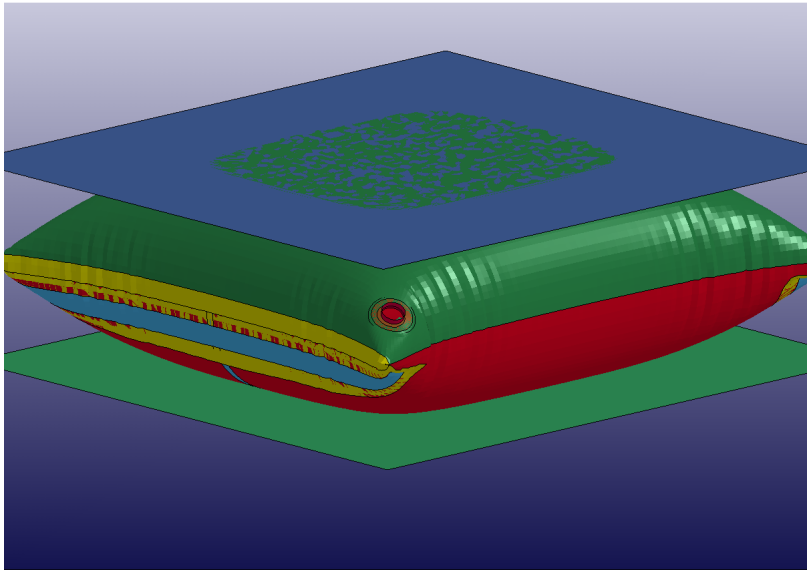

Figure 7.3: Inflated validation model, constrained at a 300 mm gap.

Figure 7.4: Inflated sample bag, constrained at a 300 mm gap.

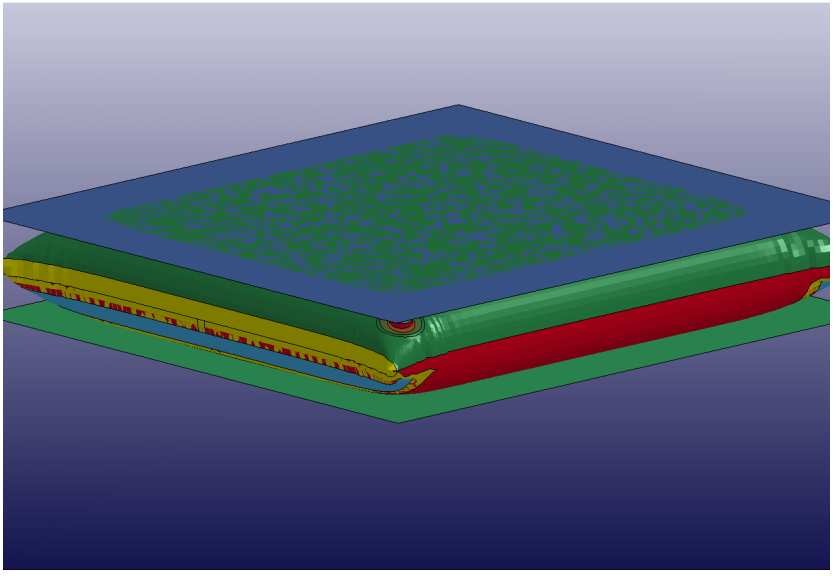

Figure 7.5: Inflated validation model, constrained at a 150 mm gap.

Figure 7.6: Inflated sample bag, constrained at a 150 mm gap.

equivalent sample set, but the material properties of the paper in the simulation do not allow the failure to be simulated. From supplier data, it is known that kraft paper fails at 5% elongation. This could be used as a method of determining failure.

The validation model data was compared with the averaged data for each physical test set. In table 7.1 the value for internal pressure, when the maximum strain in the simulated bag reaches 5%, is compared to the average burst pressure of the physical tests. The results using a strain based failure criterion show no relation between the physical and simulated models. This could be due to the combination of folding and wrinkling during the early stages of inflation plastically deforming areas of the mesh and the material model that is overly stiff. The material model used here is for an isotropic material, paper is highly orthotropic, having a machine direction (MD) elastic modulus that is twice that of the cross direction (CD) elastic modulus and ten times the through-thickness (ZD) elastic modulus. Additionally a finer mesh could be required in the wrinkle and fold areas to minimize spurious stress concentrations.

Table 7.1: Burst pressure data for simulated and physical testing.

Test Set Number	Simulation Pressure at 5% Elongation (Pa)	Physical Burst Pressure (Pa)
1	1438	20377
2	1325	32550
3	40709	54948
4	1851	30459
5	1218	40400
6	12007	56598
7	4340	58482
8	1851	82956
9	1478	85086
10	1866	45834
11	1719	85140
12	1627	84738

Table 7.2 compares the average contact force exerted by the a particular test set with the contact force recorded in the equivalent simulation. The error between the physical and simulated models is shown in the last column. The average error over all the comparisons is 6%, with the highest error being 10.8%. Using contact force as a comparative measure the simulations compare well with the physical tests. In the physical testing the average standard deviation within a test set was 8%.

Table 7.2: Contact force data for simulated and physical testing. Unconstrained bags do not have an associated contact force

Test Set Number	Simulation Contact Force at Burst (N)	Average Physical Burst Contact Force (N)	Contact Force Error (%)
1	NA	NA	NA
2	25394	25307	0.43
3	72800	67803	7.36
4	NA	NA	NA
5	8036	8282	2.97
6	25628	23112	10.8
7	108973	105125	3.66
8	37183	34048	9.2
9	112054	104468	7.21
10	42564	39796	6.95
11	78880	72742	8.48
12	156558	151516	3.26

It is known from past experience that a smaller gap size allows a greater burst pressure for a given bag. Simulations confirm that bags constrained by a small void withstand a higher pressure. Each simulation was run to the burst pressure of the physical tests, and in each case the maximum stress in the bag at the end of the simulation was between 90 and 100 MPa.

7.4 Literature Comparison

Levy (1942) described the analytical solution to the deformation of a square plate subjected to a normal pressure load, which undergoes a deflection of up to 1.9 times the thickness of the plate. This is less than the deformation seen in the inflated dunnage bags. Ramberg *et al.* (1942) conducted a series of tests on both clamped and freely supported plates subjected to a pressure load. The authors describe the position and relative magnitude of bending strains, as well as giving a stress contour plot for a rectangular plate.

Figure 7.7 shows the stress pattern of a representative inflated model. This model matches the patterns seen in both of these sources.

7.5 Failure Data Comparison

Next the stress patterns on the verification models were compared to the failure zone data collected in the physical burst tests.

In the physical tests, 63 of the 90 bags tested had failures involving the punched hole. This failure type was more prominent in the bags tested at a

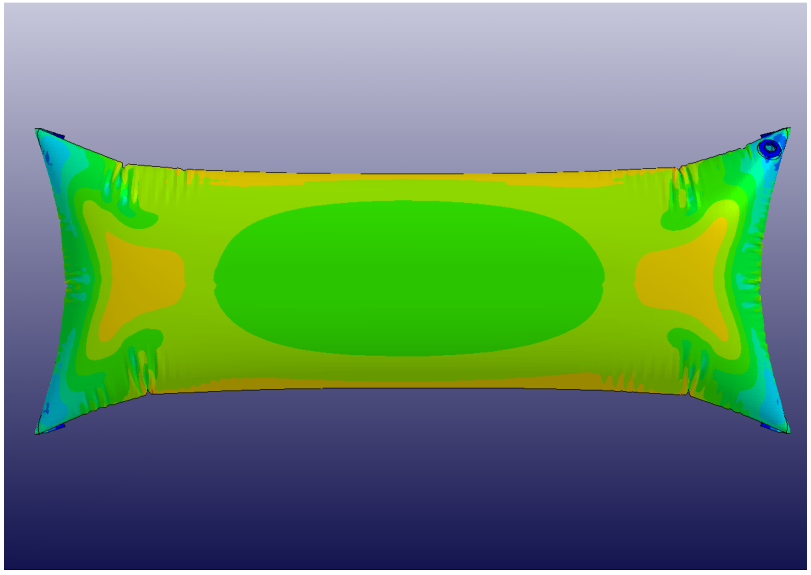

Figure 7.7: Top view of the Von Mises stress for the inflated validation model, where red is a high and blue is a low stress.

150 mm gap. Figure 7.8 shows the area around the hole for a burst bag. Three tears are seen radiating from the punched hole. Figure 7.9 shows the stress pattern in the same area of a simulated model with the same gap size. Three stress concentrations are present on the edge of the punched hole matching the tear points of the physical bag.

Figure 7.8: Failure of a sample bag at the valve corner.

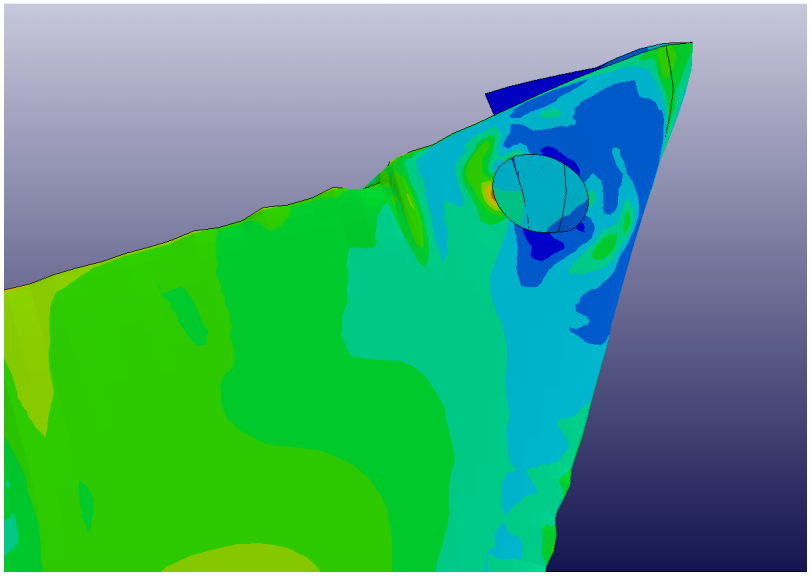

Figure 7.9: Enlarged view of the Von Mises stress for the inflated validation model near the valve, where red is a high and blue is a low stress.

Simulations of unconstrained bags, Fig. 7.10 and 7.11, show high stress concentrations near the center of the inflated bag, along the fold edges and at the valve. The center of the bag and along the fold lines show a maximum stress. This correlates well with the test data that showed several bags failing in these zones.

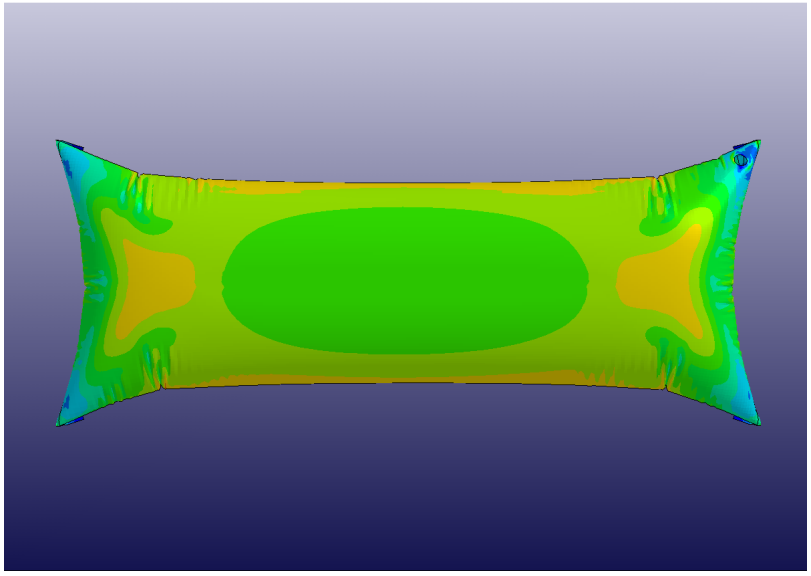

Figure 7.10: Top view of the Von Mises stress for the inflated validation model, unconstrained, where red is a high and blue is a low stress.

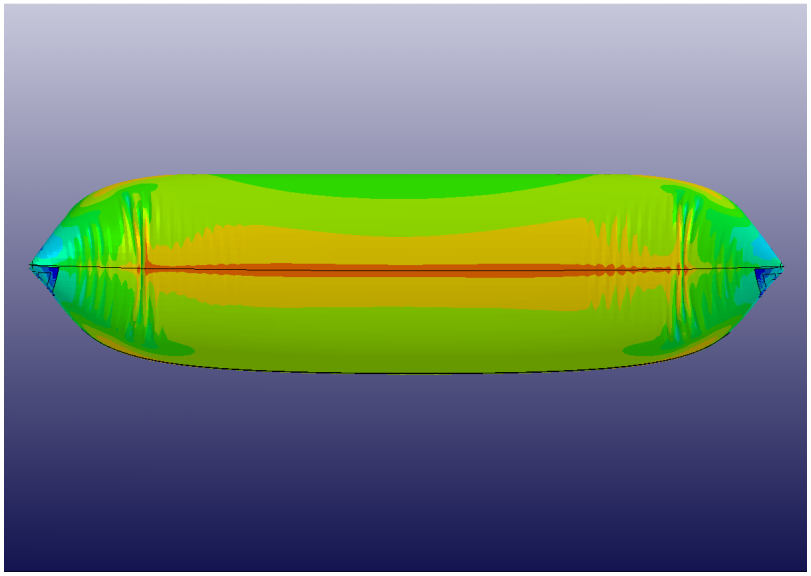

Figure 7.11: Side view of the Von Mises stress for the inflated validation model, unconstrained, where red is a high and blue is a low stress.

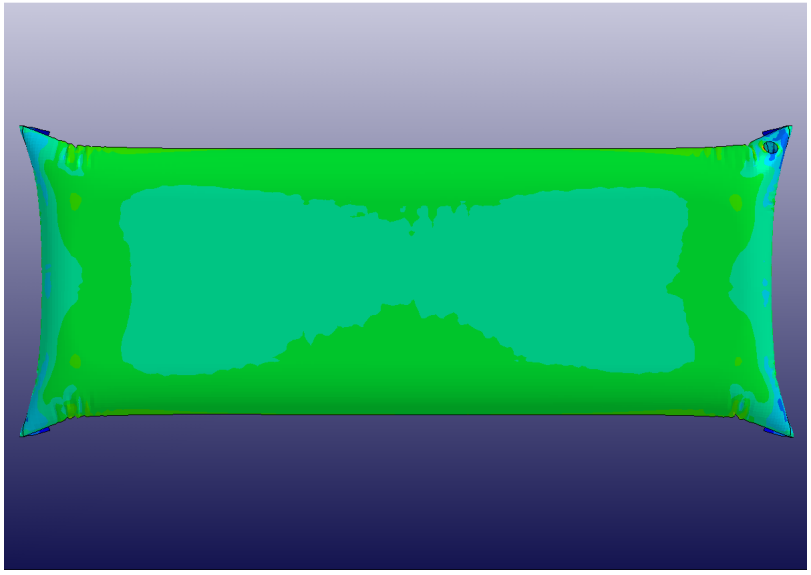

Figure 7.12: Top view of the Von Mises stress for the inflated validation model, constrained at 300 mm, where red is a high and blue is a low stress.

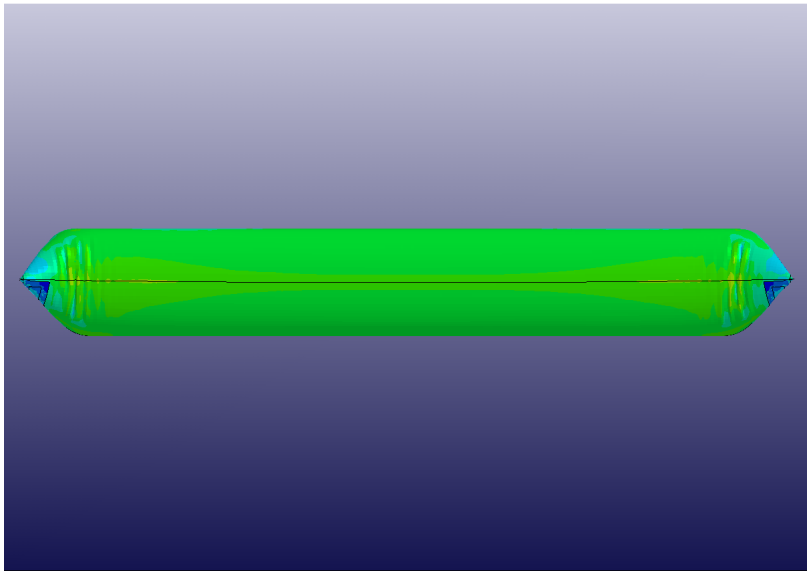

Figure 7.13: Side view of the Von Mises stress for the inflated validation model, constrained at 300 mm, where red is a high and blue is a low stress.

When simulated bags were constrained in a gap of 300 mm, the center was no longer a high stress area as it is supported by the rigid plates. The stress along the edge folds is also slightly reduced, Fig. 7.12 and 7.13. This means that the stress concentration near the valve becomes more prominent. This again correlates well to physical test data, as there were no failures corresponding to a center burst recorded at this gap size. More failures occurred along the edges, though the failure edge was not restricted to those near the valve.

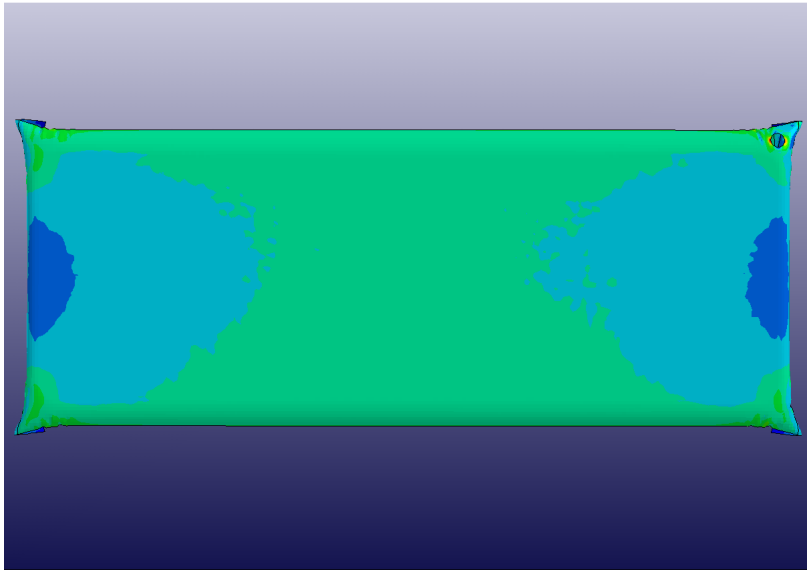

Figure 7.14: Top view of the Von Mises stress for the inflated validation model, constrained at 150 mm, where red is a high and blue is a low stress.

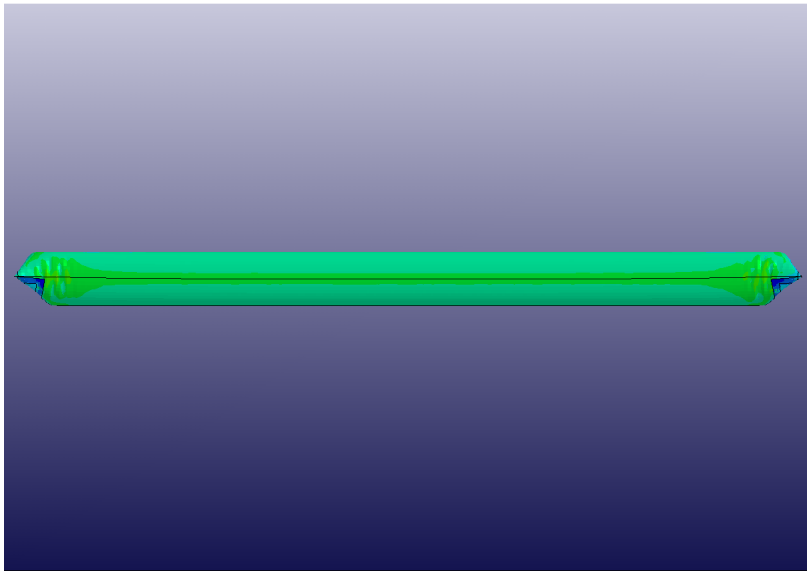

Figure 7.15: Side view of the Von Mises stress for the inflated validation model, constrained at 150 mm, where red is a high and blue is a low stress.

Simulations of a 150 mm gap size showed reduced center and edge fold stresses. The dominant stress concentrations are in the area of the valve, Fig. 7.14, 7.15 and 7.16. The high number of failures along edges one and two during physical testing validate the simulation results.

Though no direct strain measurement was possible on the paper bags, the evidence provided here verifies that the simulated model has the capacity to give strong trend information for a simulated loading, meeting its primary

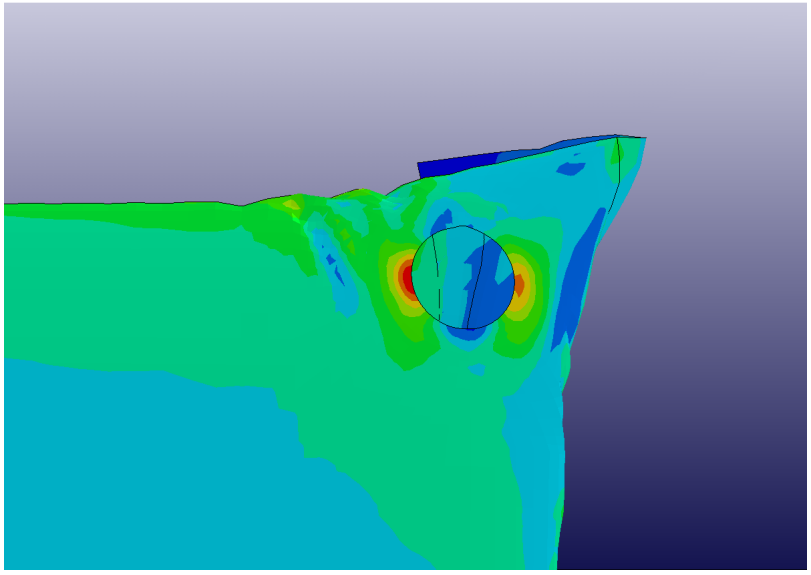

Figure 7.16: Top view of the Von Mises stress for the inflated validation model near the valve, constrained at 150 mm, where red is a high and blue is a low stress.

objective. This model can, however, not be used to predict burst pressure. The current model has elements that experience strains above their failure limit during inflation. The elements then fail while the pressure is low. Further investigation will be required to produce a model that is capable of predicting the burst pressure for a particular bag configuration.

Chapter 8

Conclusions

The goal of this project was to build a design tool capable of simulating the inflated shape of a paper dunnage bag. The objective was to build a numerical model that has a representative material model, a means of inflating the dunnage bags, reproduces the inflated shape of the dunnage bag, allows for various void shapes and sizes and shows the stress trends associated with the inflated shape. The model produced was then compared to physical tests. To meet these objectives, a model was developed for LS-DYNA.

The cover used for the dunnage bags, kraft paper, is a complex engineering material, and the inclusion of all its known properties was not possible within the scope of this project. Several material models were considered to reduce the complexity of the material while maintaining the accuracy of the model. Basic tensile test data was supplied and used to assist in the selection of a material model. The choice was made to use a bilinear material model and include plastic effects. A bilinear model represents the properties of kraft paper well and LS-DYNA has a material model capable of including the desired effects. A bilinear elastic-plastic isotropic material with kinematic hardening was chosen for this model.

A pressure load was used as the mechanism that inflates the virtual bags. This mechanism suits the purpose of this model but has limited application for further development. Future models should use a mechanism that is driven by volume rather than pressure as this would improve stability during initial inflation and with the inclusion of gas laws, the model can be used to simulate dynamic tests performed on the sample bags.

The current model has been developed, including surface-to-surface contact that can be used to define various void sizes and shapes.

Physical tests were run and the results of these tests were compared with the results of the simulated models. Good consistency was found between the final shape of the physical and simulated models. Comparisons can be made between the areas where wrinkling takes place and where large folds form. The same trends in the position of wrinkling and folding were seen when the void size was changed. The tendency that as void size is reduced the wrinkle area shifts towards the bag corners is mirrored in the simulated models. When

the numerical data, gained from the physical tests, was compared to the data extracted from the simulations it was found that the simulations predicted the restraining force of the dunnage bags to within 7% which is less than the average standard deviation of the physical tests for the same measure.

The stress pattern seen in the fully inflated simulation model was compared with available literature. It was found that even though the deflections in this model are far more than those discussed in literature a similar stress distribution is seen in the simulations. This model can however not be used to investigate stress distribution during the early phases of inflation as a surface pressure based mechanism does not provide the same support as a volume based simulation.

The position of stress concentrations were investigated and compared with the positions of failure in the test samples. It was found that the simulation predicted the position of failure in the valve area well, with failure in the sample matching positions indicated by the simulations.

Further investigations compared the trends associated with changing the simulation variables. The effect of constraining sample test bags at various gap sizes was found to be an increased burst pressure for smaller gap sizes and a tendency for bag failures involving the valve to dominate. These results were reproduced in the simulated model, where the magnitude of the stress in the constrained contact area of the bag was immediately reduced when contact was made with the constraining surface. As the gap size was reduced, the center and edge stresses also reduce while those near the valve increased. The effect of ply number was then investigated. It was found that increasing the section thickness was a good representation of the multi-ply bags. The results of these tests and simulations differing no more than those of the single-ply bags. Thus there is no need to model two distinct plies.

This model is not capable of predicting burst pressures or being updated to include dynamic testing at this point. It is however capable of simulating the inflation of an initially flat paper dunnage bag. The final shape of the simulated dunnage bags match the physical samples tested for various bag sizes, having either one or two plies, inflated into various void sizes. The model has been validated in such a way that it can be developed to gain further insight into the stress distributions of new paper dunnage bags.

Chapter 9

Further Investigation of Inflatable Paper Dunnage Bags

With this basic model built, several model adaptations are possible to more closely represent the physical bag and extend the use of the model to prediction. This section covers some of the ideas that should be tested.

9.1 Valve Changes

Changes can be made to the size, shape and position of the valve. Changing the position of the valve is easily done. From the testing and simulations done to date, it is known that the position of the valve has a large influence on burst conditions of the bag. It is far easier to test the effects of changing the position of the valve with this type of simulation than manufacturing and testing adapted bags. Once the methods involved with the construction of a suitable bag mesh are known, the valve can be positioned anywhere on the bag. It is important to note that there are stress concentrations near the hole and the mesh in the vicinity of the hole should be sufficiently dense to capture these effects.

It is also known that the size of the valve affects the burst pressures reached by the inflated bag. A smaller hole allows for higher burst pressures. Different hole diameters can be tested to find a balance between large diameters for increased inflation speeds and small diameters for higher burst pressures.

The model may also be used as a design tool in testing different valve shapes. There are cases when a round inflation valve of a given diameter may greatly reduce the burst pressure of the bag. If another shape was used, the same hole area might be maintained without much loss in burst pressure. This is not a feasible line of investigation using standard testing tools as the cost of designing and manufacturing prototype valves is high.

9.2 Geometry Changes

Alternative bag geometries may be tested using the model, before manufacturing prototypes. A simple model adaptation is to change the analysis of the bag for shapes such as a trapezoid. A trapezoid shape may lower the burst pressure of the bag, but if the bag failures are then more consistent and predictable this could be an advantage to the end user.

A second geometry change that could be investigated is to design the deflated bag for a given void. This method could be used to more evenly distribute the stress present in the inflated bag. This may increase burst pressures.

9.3 Manufacturing Defects

An important aspect of this numerical model is the ease with which a sensitivity analysis can be performed. A sensitivity analysis would show how an incremental change in one parameter, such as the geometry or pressure, would affect the burst pressure of the bag. Such an investigation would direct manufacturers as to which parameters should be more closely monitored during quality control.

9.4 Internal Fluid

A shortfall of this model is that it does not take into account the volume of air inside the bag. The air volume and relative stiffness have an effect on the wrinkle pattern. If a volume of air is present in the model, dynamic testing of the model can be done. As the volume of the physical bag is reduced, the air inside compresses and the internal pressure is increased. The current model does not capture this characteristic because a fixed pressure is used to represent the volume of air. This adaptation would allow the model to more accurately represent the physical bag.

9.5 Multiple Bags

With a functional inflated bag model, static tests of various bag combinations can be performed. For example, it is known that a given bag has a higher burst pressure when filling a smaller void. Should there be a need to fill a large void, it would be advantageous to test whether using more than one bag would reduce failure rates, and what optimum pressure those bags should be inflated to.

If two bags are inflated, one within the other, at two different pressures, a two stage spring might be produced. This might allow users to customize the spring characteristic of the restraining force.

9.6 Working Conditions

The next logical step in dunnage bag research would be to investigate how dunnage bags are used. The question of how dunnage bags are currently used and the purpose of dunnage bags would dictate the nature of further research. If the restraining force is critical one would design the bag in one way but if the maximum deceleration is critical the bags should be designed in another.

9.7 Material Properties

To improve the accuracy of the current models, a better material model for kraft paper is required. Currently data on the full material characteristic is difficult to access. A bilinear tensile test machine would help to get more accurate data on the material.

Appendices

Appendix A

Material Models for Paper

Material models are numerical relationships between material parameters. The use of a numerical model to describe these relationships reduces the amount of data required by the finite element model to generate the parameters needed at a particular point in an analysis. Assumptions are made so that the model can be as simple as possible.

Paper properties are presented here as constitutive models. There are two kinds of constitutive models of paper. The first type of model is a micro-property model, where paper is seen as a network of fibers. These network models have been created to predict paper strengths based on the properties of its constituent materials. The second model type is a continuum model. These models are generated using the macro-properties of paper. Several assumptions are made for both these model types. This section will focus on the continuum models for paper as they are better suited to finite element modeling and the testing of material properties is simpler [Ramasubramanian and Wang (1999)].

Ramasubramanian and Wang (1999) gives a short description of several different types of continuum models that can be used to describe paper. These are used as a brief theory section of model development. This is followed by a discussion of the most popular constitutive models available.

A.1 Nonlinear Elastic Plate Model

Johnson and Urbanik (1984) applied classical continuum theory to a paper plate. Making the assumption that on a macro scale paper is homogeneous, they formulated basic equations for three dimensional nonlinear elasticity. They related plate behavior to strain energy density,

$$\sigma_{ij} = \frac{\partial W}{\partial \varepsilon_{ij}} \tag{A.1.1}$$

where W is a function of e, the in-plane strains at mid-plane. Johnson and Urbanik proposed a nonlinear effective strain,

$$e = \frac{\varepsilon_x^2}{\nu_{yx}} + \frac{\varepsilon_y^2}{\nu_{xy}} + 2\varepsilon_x\varepsilon_y + \frac{C}{4}\gamma_{xy}^2 \tag{A.1.2}$$

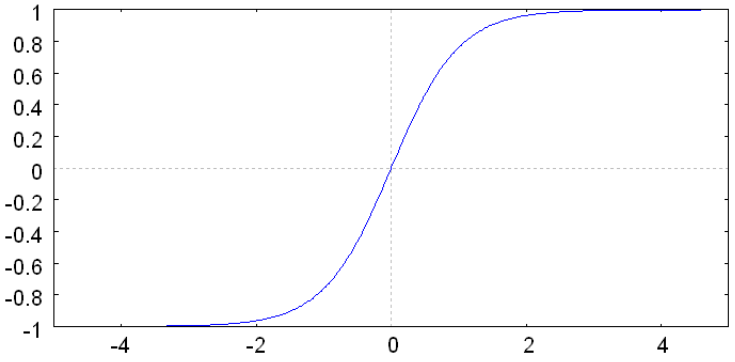

Figure A.1: Characteristic stress-strain curves of paper using the method described by Johnson and Urbanik (1984).

Here ν is the Poisson's ratio, ε is the in-plane axial strain, γ is the in-plane shear strain and C is a function of the axial and shear stress, E and G.

$$C = \frac{4G_{xy}(1 - \nu_{xy}\nu_{yx})}{\nu_{xy}E_x} \tag{A.1.3}$$

The stress-strain data acquired in tensile testing is fitted to equation A.1.4, solving for constants c_1 and c_2.

$$\sigma(\varepsilon) = c_1 \tanh\left(\frac{c_2\varepsilon}{c_1}\right) \tag{A.1.4}$$

Equation A.1.1 can then be integrated in the form $W(\varepsilon)$. This results in equation A.1.5 which is plotted in Fig. A.1 with all constants set to one.

$$\sigma_1(\varepsilon_1) = c_1\sqrt{\frac{c_2}{c_1}}\tanh\left(\frac{c_2}{c_1}\sqrt{\frac{\nu_1}{\nu_2}}\varepsilon\right) \tag{A.1.5}$$

This model captures the indistinct yield point observed in paper testing. Furthermore, the stress strain gradient approaches zero as strain increases. This implies that the model has the capacity to approach pure plasticity at high strains. However, the model is expected to fail if the material reaches plasticity, as the mathematics driving the model are based on conservation of strain energy which is violated under plastic deformation. This can be noted by the rise in temperature experienced by a material undergoing plastic deformation.

A.2 Hyperelastic Model

The hyperelastic model proposed by Suhling *et al.* (1989) is an adaptation of the model by Johnson and Urbanik (1984). The model is still based on the assumption that paper is elastic only. For this model, the stress-strain relationship is given by the second Piola-Kirchoff stress tensor, which for small

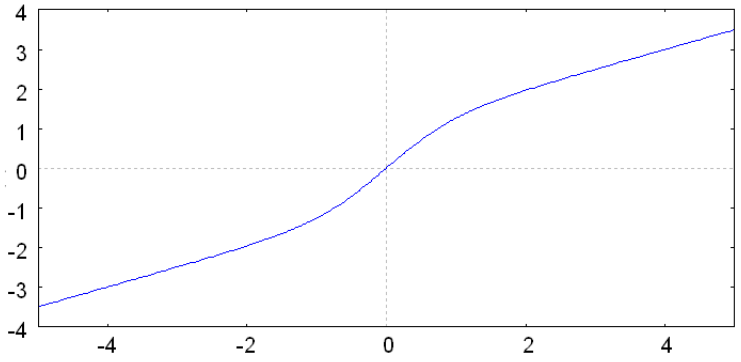

Figure A.2: Characteristic stress-strain curves of paper using the method described by Suhling *et al.* (1989).

displacement gradients could be replaced by equation A.1.1 [Ramasubramanian and Wang (1999)]. For this model, the Poisson's ratios are determined empirically in addition to the strain density. The strain energy density function is changed from that in equation A.1.4 to

$$\sigma(\varepsilon) = c_1 \tanh(c_2\varepsilon) + c_3\varepsilon \tag{A.2.1}$$

and the stress-strain relationship is updated to that of Fig. A.2. Suhling *et al.* (1989) generates two strain energy equations, one in the MD and one in the CD. Each of these are fitted to data generated by uniaxial testing in that direction. At high strains this model deviates from measured data [Ramasubramanian and Wang (1999)]. In reality, paper exhibits significant plasticity. The deviation of this model is attributed to energy dissipation which, like the Johnson and Urbanik (1984) model, is based on an assumption that strain energy is conserved.

A.3 Laminate Model

The composite laminate model proposed by Salmen *et al.* (1984) is based on laminate plate theory. Each layer in this laminate approach is seen as unidirectional cellulose fibers embedded in a hemicellulose matrix. The layers are in in-plane stress and are perfectly bonded to each other. The constitutive relationship is then derived using Kirchoff plate theory. In order to make use of this model, information about the mechanical properties of the constituent fibers and their bonds must be known. This model fits data well for isotropic paper but over-predicts the properties of orthotropic and anisotropic paper. Properties for the constituents of paper are also difficult to obtain. Once a working material model is found, work might be done on data matching a composite model.

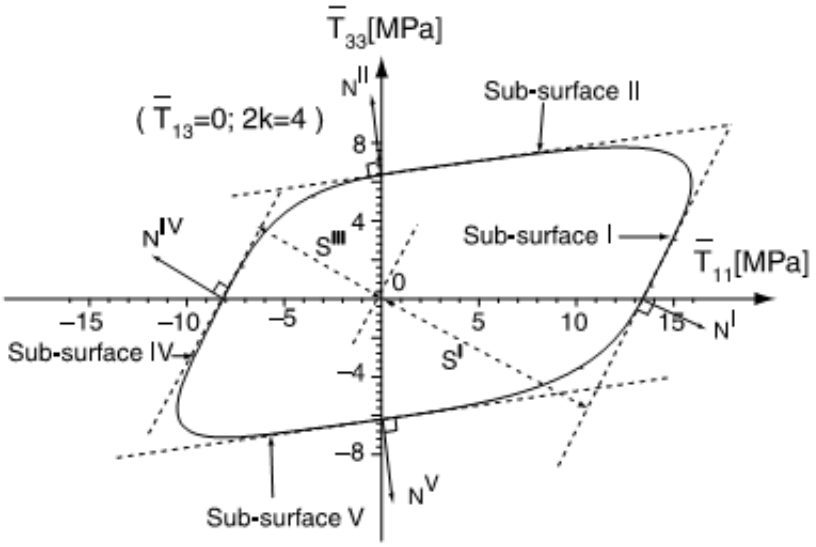

Figure A.3: Yield surface predicted by equation A.4.1, using the method described by Xia *et al.* (2002).

A.4 Anisotropic Elastic-Plastic Model

Xia *et al.* (2002) propose a finite deformation, anisotropic, elastic-plastic behavior model. The model assumes that the initial behavior exhibited is a purely orthotropic elastic behavior. The model assumes the in-plane behavior to be elastic-plastic and the out-of-plane behavior to be elastic. The application of this model is limited to in-plane loading unless the decohesion models are used [Xia *et al.* (2002)]. In metal plasticity plastic flow is governed by shear, requiring that yield stress be based on deviatoric stress. Unlike in metal plasticity, there is no evidence that plasticity in paper is driven by deviatoric stress. This necessitates the total stress be used to determine the yield conditions. The yield condition proposed for this model is

$$f(\bar{\boldsymbol{T}}, S^K) = \sum_{K=1}^{N} \left[\frac{\chi_K \bar{\boldsymbol{T}} \cdot \boldsymbol{N}^K}{S^K} \right]^{2k} - 1 \tag{A.4.1}$$

which is shown graphically in Fig. A.3. The parameter $\bar{T}$ is the 2^{nd} Piola-Kirchhoff stress measure, S^K is the equivalent strength of the K^{th} sub-surface, defined by the distance from the origin to each sub-surface, N^K is the surface normal and χ_K is a switching controller,

$$\chi_K = \begin{cases} 1, & \text{if } \bar{\boldsymbol{T}} \cdot \boldsymbol{N}^i > \boldsymbol{0}; \\ \boldsymbol{0}, & \text{otherwise.} \end{cases} \tag{A.4.2}$$

The factor $2k$ is taken to be a shaping factor of greater than four. The six normals are

$$\boldsymbol{N}^K = \sum_{ij=1}^{K} N_{ij}^K \boldsymbol{e}_i \otimes \boldsymbol{e}_j \tag{A.4.3}$$

$$N_{ij}^K = N_{ji}^K \tag{A.4.4}$$

where e_i are the basis vectors for the material coordinates. The plastic flow is then taken to be

$$\widehat{\boldsymbol{K}} = \frac{\partial f}{\partial \bar{\boldsymbol{T}}} \tag{A.4.5}$$

and by inserting equation A.4.1 into A.4.5

$$\widehat{\boldsymbol{K}} = \sum_{K=1}^{N} 2k\Lambda_K^{2k-1} \frac{\chi_K \boldsymbol{N}^K}{S^K} \tag{A.4.6}$$

$$\Lambda_K = \frac{\bar{\boldsymbol{T}} \cdot \boldsymbol{N}^K}{S^K} \tag{A.4.7}$$

This model has the potential to compensate for strain hardening by adding an evolutionary component to the strength parameter. Furthermore, this model allows for the simulation of complex loading conditions such as those experienced in a folding process.

A.5 Elasto-Plasticity Model

Castro and Ostoja-Starzewski (2003) developed an in-plane tensile response model for paper. The model disregards viscosity, assuming that strain rates are low. As seen in the previous models, paper has no well-defined yield point. The hyperelastic model described by Suhling *et al.* (1989) does not describe plastic unloading in paper. Therefore Castro and Ostoja-Starzewski (2003) based their model in thermomechanics, using internal variables. The failure envelope for paper is commonly described as elliptical

$$F_{11}\sigma_{11}^2 + 2F_{12}\sigma_{11}\sigma 22 + F_{22}\sigma_{22}^2 + F_{66}\sigma_{12}^2 = 1 \tag{A.5.1}$$

where,

$$F_{11} = \frac{1}{XX'} \tag{A.5.2}$$

$$F_{22} = \frac{1}{YY'} \tag{A.5.3}$$

$$F_{66} = \frac{1}{S^2} \tag{A.5.4}$$

X,X',Y and Y' are the tensile and compressive yield strengths in the MD and CD respectively. F_{12} is zero when there is no shear load.

A.5.1 Linear Elastic Orthotropic Model

Pre-yield, a linear-elastic orthotropic model is used to describe the behavior of paper. Equations A.5.5 through A.5.7 show the formula used in a plane model.

$$\sigma_{11} = \frac{E_1}{1-\nu_{12}\nu_{21}}\varepsilon_{11} + \frac{E_2\nu_{12}}{1-\nu_{12}\nu_{21}}\varepsilon_{22} \tag{A.5.5}$$

$$\sigma_{22} = \frac{E_1\nu_{21}}{1-\nu_{12}\nu_{21}}\varepsilon_{11} + \frac{E_2}{1-\nu_{12}\nu_{21}}\varepsilon_{22} \tag{A.5.6}$$

$$\tau_{12} = G\gamma_{12} = 2G\varepsilon_{12} \tag{A.5.7}$$

E_1 and E_2 are the Young's moduli in the MD and CD respectively, $\nu_{12} = \frac{-\varepsilon_{22}}{\varepsilon_{11}}$ and $\nu_{21} = \frac{-\varepsilon_{11}}{\varepsilon_{22}}$ are the Poisson's ratios for strain in the CD when stressed in the MD and the Poisson's ratio for strain in the MD when stressed in the CD respectively and G is the shear modulus in the MD-CD plane. For an orthotropic material

$$\frac{E_1}{E_2} = \frac{\nu_{12}}{\nu_{21}} \tag{A.5.8}$$

or

$$E_1\nu_{21} = E_2\nu_{12} \tag{A.5.9}$$

must be met. The shear modulus is then approximated as,

$$G = \frac{E_1E_2}{E_2 + E_1 + E_1\nu_{21} + E_2\nu_{12}} \tag{A.5.10}$$

A.5.2 Nonlinear Hyperelastic Orthotropic Model

Castro and Ostoja-Starzewski (2003) extend the hyperelastic model of Suhling *et al.* (1989). The proposed constitutive orthotropic model is

$$\begin{bmatrix}\sigma_{11}\\ \sigma_{22}\\ \tau_{12}\end{bmatrix} = 2\frac{dw(e)}{de}\begin{bmatrix}\frac{1}{\nu_{21}} & 1 & 0\\ 1 & \frac{1}{\nu_{21}} & 0\\ 0 & 0 & \frac{G(1-\nu_{12}\nu_{12})}{\nu_{21}E_1}\end{bmatrix}\begin{bmatrix}\varepsilon_{11}\\ \varepsilon_{22}\\ \gamma_{12}\end{bmatrix} \tag{A.5.11}$$

Given that there is no clear yield point in the stress-strain response for paper, it can be assumed that the stress-strain curve can be fitted to

$$\frac{dw(\varepsilon_{11})}{d\varepsilon_{11}} = A\tanh(b\varepsilon_{11}) \tag{A.5.12}$$

Where A and b are constants to be determined. The resulting empirical equation can then be integrated to find the stress energy function $w(\varepsilon_{11})$, which is shown in equation A.5.13 as a function of the effective strain e.

$$w(e) = \frac{A}{b}\log\left[\cosh\left(b\sqrt{\frac{\nu_{21}e}{1-\nu_{12}\nu_{21}}}\right)\right] \tag{A.5.13}$$

Substituting equation A.5.13 into equation A.5.11 and using results of a biaxial tensile tests, with the $\varepsilon_{22} = 0$, the value of b can be found as well as the zero-strain tangent moduli Q_{11},Q_{22} and Q_{12}.

$$Q_{11} = \frac{d\sigma_{11}^{(1,0)}(0)}{d\varepsilon_{11}} = \frac{Ab}{1-\nu_{12}\nu_{21}} \tag{A.5.14}$$

$$Q_{12} = \frac{d\sigma_{11}^{(0,1)}(0)}{d\varepsilon_{22}} = \frac{Ab\nu_{21}}{1-\nu_{12}\nu_{21}} \tag{A.5.15}$$

$$Q_{22} = \frac{d\sigma_{22}^{(0,1)}(0)}{d\varepsilon_{22}} = \frac{Ab\nu_{21}}{\nu_{12}(1-\nu_{12}\nu_{21})} \tag{A.5.16}$$

From this $E_1 = Ab$ and because $E_2\nu_{12} = E_1\nu_{21}$,

$$\begin{bmatrix}\sigma_{11}\\ \sigma_{22}\\ \tau_{12}\end{bmatrix} = \frac{1}{b}\begin{bmatrix}Q_{11} & Q_{12} & 0\\ Q_{12} & Q_{22} & 0\\ 0 & 0 & G\end{bmatrix}\begin{bmatrix}\tanh(b\varepsilon_{11})\\ \tanh\left(b\varepsilon_{22}\sqrt{\frac{\nu_{21}}{\nu_{12}}}\right)\\ \frac{\tanh(b\varepsilon_{11})}{\varepsilon 11}\gamma_{12}\end{bmatrix} \tag{A.5.17}$$

This model is a good fit for conditions where stress in the MD dominates stress in the CD, but in general this model over-predicts stiffness at stresses approaching failure.

A.6 Orthotropic Elastic-Plastic Model

The model proposed by Mäkelä and Östlund (2003) is a simplification of the model proposed by Xia *et al.* (2002). Xia *et al.* (2002) propose a complex anisotropic model that includes many of the mechanical properties of paper, however there are many instances where a simplified model would both suffice and be preferred. The proposal is that an orthotropic elastic-plastic constitutive model based on J_2-flow theory is a reasonable material model for paper. The model assumes small deformation. This method uses a non-quadratic yield surface

$$\sigma_e = \left(k(3J_2)^3 + (1-k)\left(\frac{27J_3}{2}\right)^2\right)^{\frac{1}{6}} \tag{A.6.1}$$

where σ_e is an effective stress based on the second invariant of the deviatoric stress tensor, J_2 and J_3 are the second and third invariants of the deviatoric stress tensor and k is a factor that determines the influence of the third invariant.

The non-quadratic effective stress measure leads to an orthotropic non-quadratic elastic-plastic strain hardening constitutive relation

$$d\varepsilon_{ij} = S_{ijkl}d\sigma_{kl} + \frac{729n(\sigma_e^{'})^{n-11}}{4E_0^n}L_{ijmn}Q_{mn}L_{klpq}d\sigma_{kl} \begin{cases} \text{if } f = 0 \text{ and } d\sigma_e^{'}, \end{cases} \tag{A.6.2}$$

$$d\varepsilon_{ij} = S_{ijkl}d\sigma_{kl} \begin{cases} \text{if } f < 0 \text{ or,} \\ \text{if } f = 0 \text{ and } d\sigma_e^{'} \leq 0 \end{cases} \tag{A.6.3}$$

where

$$Q_{ij} = kJ_2^{'2}s_{ij}^2 + \frac{9}{2}()J_3^{'}s_{ik}^{'}s_{jk}^{'} \tag{A.6.4}$$

$$f = \sigma_e(J_2, J_1) - H \tag{A.6.5}$$

For the orthotropic tri-axial model, 17 parameters are required, 9 elastic parameters (E_1, E_2, E_3, ν_{12}, ν_{13}, ν_{23}, G_{12}, G_{13} and G_{23}) and 8 describing the strain hardening (E_0, n, A, B, C, D, E and F).

The tri-axial model can be simplified to a plane stress model, as shown in Mäkelä and Östlund (2003). The model over-predicts stiffness as failure is approached.

A.7 Orthotropic Bilinear Model

Saliklis *et al.* (2003) propose a bilinear model to define the interaction of paper material parameters. The biggest advantage of this method is its simplicity. A second advantage is that yield strengths are related in orthogonal directions, which is an important aspect of strength characteristic of paper. This method fits a bilinear curve to experimental stress-strain data. This approach also uses a strain energy density function,

$$H = \frac{\nu_2 E_1}{2(1 - \nu_1\nu_2)}e \tag{A.7.1}$$

where

$$e = \frac{\varepsilon_{11}^2}{\nu_2} + \frac{\varepsilon_{22}^2}{\nu_1} + 2\varepsilon_{11}\varepsilon 22 + c\gamma_{12}^2 \tag{A.7.2}$$

$$c = \frac{4G(1 - \nu_1\nu_2)}{\nu_1 E_2} \tag{A.7.3}$$

The stress values now become functions of this strain energy density function,

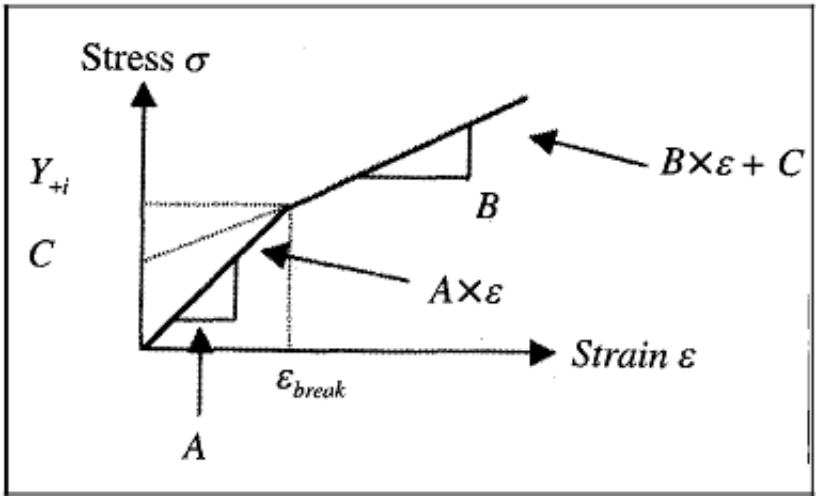

Figure A.4: Bilinear constitutive law. This image is taken from Saliklis *et al.* (2003).

$$\sigma_{11} = \frac{\partial H}{\partial \varepsilon_{11}} \tag{A.7.4}$$

$$\sigma_{22} = \frac{\partial H}{\partial \varepsilon_{22}} \tag{A.7.5}$$

$$\sigma_{12} = \frac{1}{4}\frac{\partial H}{\partial \gamma_{12}} \tag{A.7.6}$$

It is assumed that $H(e)$ is valid for both linear and nonlinear experimental data. The term $H'(e)$ is quantified by substituting H into one of equations A.7.4, A.7.5 or A.7.6 and fitting it to the data curves. Using Hill's yield criteria in place of Von Mises criteria accounts for differing yield strengths in the orthotropic directions. This also takes into account the different yield strength in tension and compression. As a result of using Hill's criteria, the stress-strain response becomes bilinear on the three axes. The constitutive model will now require two elastic moduli per direction, one initial elastic modulus and one post-yield elastic modulus. If the second modulus is set to zero, this will result in pure elastic-plastic behavior. Figure A.4 shows the bilinear constitutive law.

The accuracy of this method diminishes when the out-of-plane loading dominates. This model is the simplest to input into a finite element analysis.

A.8 Summary

Firstly it is important to note that there exists as yet no complete constitutive model for paper. There are several promising proposals but all models deviate significantly from measured data in the plastic region, though some models do

accurately predict the trends present in the material behavior. Most models make use of curve fitting, where the measured data is fitted to some or other hyperbolic tangential relationship between stress and strain. Several methods are used to develop the yield surface for paper, ranging from an augmented Von Mises criteria to the Tsai-Wu criteria, but common consensus is that Hill's criteria described by Tryding (1994) has the best fit. All models over-predict the strength of paper at higher strains. The best approach is to generate material data from both uniaxial and biaxial tension tests and, keeping in mind the application, choose the model that most closely matches the available data.

List of References

AAR (2001). Rules governing the loading, blocking and bracing of freight in closed trailers and containers for TOFC/COFC service. Tech. Rep., Association of American Railroads.

AAR (2007). Rules and procedures for testing of new loading and bracing methods or materials. Tech. Rep., Association of American Railroads.

Baum, G. (1981). Procedures for measuring the in-plane orthotropic elastic constants of paper using ultrasonic techniques. Tech. Rep., The Institute of Paper Chemistry, Appleton, Wisconsin.

Baum, G. (1984). The elastic properties of paper: A review. Tech. Rep., The Institute of Paper Chemistry, Appleton, Wisconsin.

Baum, G., Brennan, D. and Habeger, C. (1981*a*). Orthotropic elastic constants of paper. *Tappi Journal*, vol. 64(8), pp. 97–101.

Baum, G. and Habeger, C. (1980). On-line measurement of paper mechanical properties. Tech. Rep., The Institute of Paper Chemistry, Appleton, Wisconsin.

Baum, G., Habeger, C. and Fleischman, E. (1981*b*). Measurement of the orthotropic elastic constants of paper. Tech. Rep., The Institute of Paper Chemistry, Appleton, Wisconsin.

Blandino, J., Johnston, J. and Dharamsi, U. (2002). Corner wrinkling of a square membrane due to symmetric mechanical loads. *Journal Of Spacecraft And Rockets*, vol. 39(5), pp. 717–724.

Bletzinger, K., Jarasjarungkiat, A. and Wüchner, R. (2007). Wrinkling as multiscale phenomenon in numerical analysis of membranes. In: *ECCOMAS Thematic Conferance on Multi-scale Computational Methods for Solids and Fluids, Cachan, France.*

Castro, J. and Ostoja-Starzewski, M. (2003). Elasto-plasticity of paper. *International Journal of Plasticity*, vol. 19, pp. 2083–2098.

Cerda, E. and Mahadevan, L. (2003). Geometry and physics of wrinkling. *Physics Review Letters*, vol. 90(7), pp. 074302–1 – 074302–4.

Hallquist, J. (2006). LS-DYNA theory manual. Tech. Rep., Livermore Software Technology Corporation.

Haslach, H. (2000). The moisture and rate-dependant mechanical properties of paper: A review. *Mechanics of Time-Dependant Materials*, vol. 4, pp. 169–210.

Haslach, H. (2008). Time-dependant mechanisms in fracture of paper. *Mechanics of Time-Dependant Materials*, vol. 13, pp. 11–35.

Jarasjarungkiat, A. (sa). Elastoplasticity adopted wrinkling model. Tech. Rep., Lehrstuhl für Statik, Technische Universität München Arcisstr. 21, München, Deutschland D-80333.

Jimenez-Caballero, M., Conde, I., Garcia, B. and Liarte, E. (2009). Design of different types of corrugated board packages using finite element tools. In: *SIMULIA Customer Conference*.

Johnson, M. and Urbanik, T. (1984). A nonlinear theory for elastic plates with application to characterizing paper properties. *Journal of Applied Mechanics*, vol. 51, pp. 146–152.

Jones, A. (1967). *An Experimental Investigation of The In-Plane Elastic Moduli of Paper*. Ph.D. thesis, Lawrence University, Appleton, Wisconsin.

Levy, S. (1942). Square plate with clamped edges under normal pressure producing large deflections. Tech. Rep., National Advisory Commitee For Aeronautics.

Mäkelä, P. and Östlund, S. (2003). Orthotropic elastic-plastic material model for paper materials. *International Journal of Solids and Structures*, vol. 40, pp. 5599–5620.

Mann, R., Baum, G. and Habeger, C. (1979). Determination of all nine orthotropic elastic constants for machine-made paper. Tech. Rep., The Institute of Paper Chemistry, Appleton, Wisconsin.

MSC (2000). Msc.marc volume A, theory and user information, version 2000. Tech. Rep., MSC.

Ramasubramanian, M. and Wang, Y. (1999). Constitutive models for paper and other ribbon-like nonwovens - a literature review. *Mechanics of Cellulosic Materials*, vol. 85, pp. 31–42.

Ramberg, W., McPherson, A. and Levy, S. (1942). Normal-pressure tests of rectangular plates. Tech. Rep., National Advisory Commitee for Aeronautics.

Saliklis, E., Urbanik, T. and Tokyay, B. (2003). Bilinear modeling of cellulosic orthotropic nonlinear materials. *Journal of Pulp and Paper Science*, vol. 29 (12), pp. 407–411.

Salmen, L., Carlsson, L., de Ruvo, A., Fellers, C. and Htun, M. (1984). A treatise on the elastic and hygroexpansional properties of paper by a composite laminate approach. *Fiber Science and Technology*, vol. 20, pp. 283–296.

Suhling, J., Johnson, M., Rowlands, R. and Gunderson, D. (1989). Nonlinear elastic relations for cellulosic materials. *Mechanics of Cellulosic Materials*, vol. AMD- Vol.99/MD-Vol.13, pp. 1–15.

Tryding, J. (1994). A modification of the Tsai-Wu failure crition for the biaxial strength of paper. *Tappi Journal*, vol. 77(8), pp. 132–134.

Wu, T. and Ting, E. (2007). Large deflection analysis of 3D membrane structures by a 4-node quadrilateral intrinsic element. *Thin-Walled Structures*, vol. 46, pp. 261–275.

Xia, Q., Boyce, M. and Parks, D. (2002). A constitutive model for anisotropic elastic-plactic deformation of paper and paperboard. *International Journal of Solids and Structures*, vol. 39, pp. 4053–4071.

ZAF (1983). Agricultural pests Act 36 of 1983.
Available at: `www.nda.agric.za/docs/NPPOZA/Agricultural.pdf`